TOWARDS ROBUST DECONVOLUTION IN MEDICAL IMAGING: INFORMATICS, DIAGNOSIS AND TREATMENT

A Dissertation

Presented to the Faculty of the Graduate School

of Cornell University

in Partial Fulfillment of the Requirements for the Degree of

Doctor of Philosophy

by

Ruogu Fang

August 2014

TOWARDS ROBUST DECONVOLUTION IN MEDICAL IMAGING:
INFORMATICS, DIAGNOSIS AND TREATMENT

Ruogu Fang, Ph.D.
Cornell University 2014

Robust deconvolution, the task of estimating hemodynamic parameters from measured spatio-temporal data, is a key problem in computed tomography perfusion. Traditionally, this has been accomplished by solving the inverse problem of the temporal tracer enhancement curves at each voxel independently. Incorporating spatial contextual information, i.e. information other than the temporal enhancement of the contrast agent, has received significant attention in recent works. Intra-subject contextual information is often exploited to remove the noise and artifacts in the low-dose hemodynamic maps. In this thesis, we take a closer look at the role of inter-subject contextual information in robust deconvolution. Specifically, we explore its importance in three aspects. First: *Informatics* acquisition. We show, through synthetic evaluation as well as in-vivo clinical data, that inter-subject similarity provides complimentary information to improve the accuracy of cerebral blood flow map estimation and increase the differentiation between normal and deficit tissue. Second: Disease *diagnosis*. We show that apart from the global learned dictionary for hemodynamic maps, the tissue-specific dictionaries can be effectively leveraged for disease diagnosis tasks as well, especially for low-contrast tissue types where the deficits usually occur. Lastly: *Treatment* plan. We propose a generalized framework with inter-subject context through dictionary learning and sparse representation possible for any hemodynamic parameter estimation, such as

blood-brain-barrier permeability. We also extend to include inter-subject context through tensor total variation. The diverse hemodynamic maps provide necessary information for treatment plan decision making. We present results of our approaches on a variety of datasets and clinical tasks, such as uniform regions estimation, contrast preservation, data acquired at low-sampling rate and low radiation dose levels.

THESIS COMMITTEE

Prof. Tsuhan Chen

Department of Electrical and Computer Engineering

Cornell University

Prof. Ramin Zabih

Department of Computer Science

Cornell University

Prof. Noah Snavely

Department of Computer Science

Cornell University

Prof. Pina Christine Sanelli

Department of Radiology

Department of Public Health

Weill Cornell Medical College

To my parents: Zihua Fan and Zhaoxiong Fang

You are my forever support.

ACKNOWLEDGEMENTS

I thank my advisor, Prof. Tsuhan Chen, for his continuous support and advice through out these precious five years. Being your first Ph.D. student after you moved to Cornell is the best choice I have ever made. Thank you for your guidance that directed me towards medical image analysis research, the freedom you provided for me to pursue diverse topics in computer vision and machine learning, the motivating and encouraging attitude you inspired when facing challenges and unknowns, and the optimism and care you showed that accompanied me through every step of my PhD. I have always wondered how much I have learned from you in every aspect of research.

I thank my thesis committee: Prof. Pina Sanelli (you are my role model in career and research. I have always admired your devotion and passion for career. None of the works in this thesis would have happened without you), Prof. Noah Snavely (the time spent at your lectures and collaborating with you is one of my best memories at Cornell. Your acceptance, wisdom and flexibility opened up my creativity and enthusiasm towards research at the beginning of my PhD and guided me all the way through), Prof. Ramin Zabih (thank you for your guidance towards medical imaging research. I alway respect your broad knowledge and deep thinking and it was a delight collaborating with you).

I thank Shaoting Zhang, my mentor, collaborator and friend ever since meeting at MICCAI 2011 in Canada. Your candid advice and insightful analysis have enlightened me and strengthened me all the way through. Your optimism has built up my confidence and led me through challenging times, and your unreserved advice has guided me towards maturity in research. It is a blessing to have you as my mentor and friend.

I thank my collaborators, Andrew Gallagher, Alexander Loui, Kolbeinn

Karlsson, Kevin Tang, Ashish Raj, Leo Grady and Joyce Yu-hsin Chen. It was a pleasure and a great learning experience working with each of you.

I thank all the Advanced Multimedia Processing lab members: Amir Sadovnik, Kuan-Chuan Peng, Amandy Nwana, Henry Shu, Congcong Li, Yi-meng Zhang, Zhaoyin Jia, Adarsh Kowdle, Druve Batra and Yao-Jen Chang. I also thank the visitors, the undergraduate and MEng students I had the pleasure of collaborating and mentoring over the years. The inspiring discussions and the informative tutorials at the weekly group meetings engaged us into not only collaboration, but also lasting friendship. I am grateful to the open-minded atmosphere at Cornell which gave me the depth and broadness of research exploration.

I thank all my wonderful friends at Cornell. You have made my life at Cornell full of love, care and truly beautiful memories.

I thank my parents, my sister and all my family members for being there supporting me through out the years. A special thank to my mother, whose love and encouragements have made my last years of graduate life special and memorable.

TABLE OF CONTENTS

LIST OF TABLES

LIST OF FIGURES

CHAPTER 1

INTRODUCTION

Deconvolution in medical imaging is an inverse process to estimate the hemodynamic parameters, such as the blood flow, blood volume and mean transit time, from the measurements in the medical images, as illustrated in Figure 1.1. A traditional machinery employed for estimating these hemodynamic parameters is to compute the impulse response function of each voxel independently using matrix factorization or curve fitting. For instance, singular value decomposition (SVD) is widely used in current commercial softwares to inverse the convolution process.

When SVD-based algorithms are proposed in 1990s, they assume the X-ray radiation and intravenous injection are high enough to generate accurate measurements. However, the elevated radiation exposure in computed tomography perfusion (CTP), one of the most widely used imaging modality for hemodynamic parameter estimation, has raised significant public concerns regarding its potential biological effects and potential increase of cancer risk. Consensus has been reached that the "as low as reasonably achievable" (ALARA) principle should be executed more consistently. The low-dose protocols using existing deconvolution methods are unfortunately leading to higher image noise, as illustrated in Figure 1.2, which is compensated by using spatial smoothing, reduced matrix reconstruction and/or thick-slices, at the cost of lowering spatial resolution. Furthermore SVD-based methods tend to introduce unwanted oscillations and results in estimation bias.

Recently works have observed that the cues of hemodynamic parameters are not present only within the target voxels. The dynamic information surround-

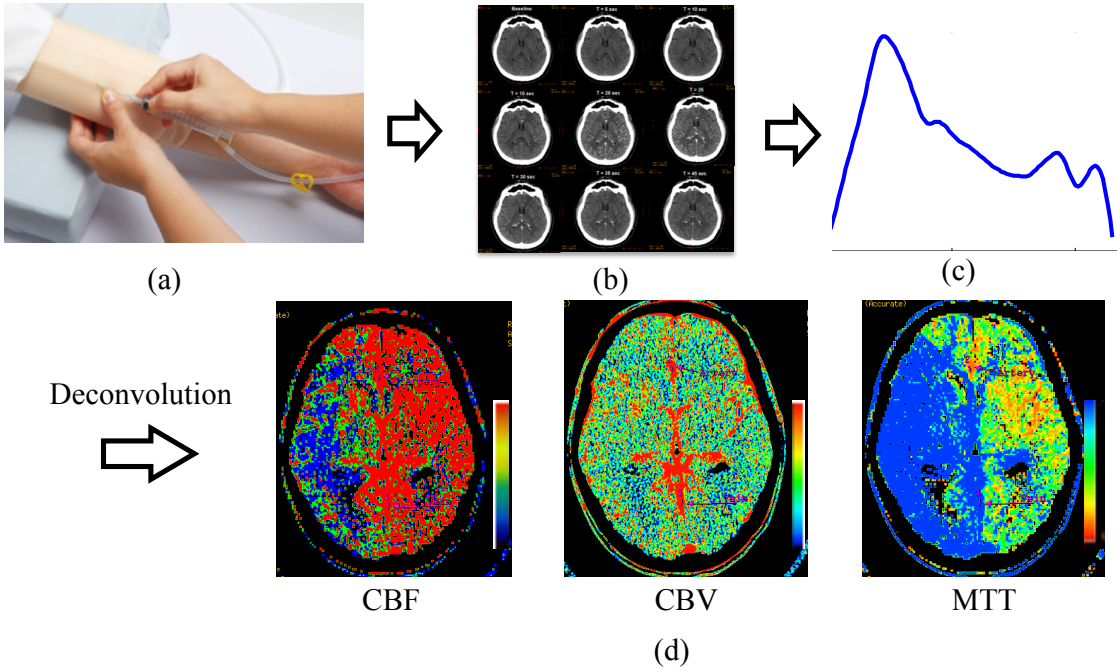

Figure 1.1: Deconvolution in computed tomography perfusion as an inverse process. (a) Intravenous injection of contrast agent to trace the blood flow. (b) Cine scanning of the brain slice at continuous time points. (c) Extracted tissue enhanement curve (TEC) from a voxel location. (d) Estimated cerebral blood flow (CBF), cerebral blood volume (CBV) and mean transit time (MTT) by deconvolution from the TECs.

ing the target voxel also holds strong cues about the functionality of the target voxel. For example, the neighboring voxels in the same anatomical region of the target voxel should have same or similar hemodynamic parameter values as the target voxel. Many works have attempted to incorporate this spatial contextual information, as opposed to using the temporal dynamic model of the voxel of interest alone, into the hemodynamic parameter deconvolution pipeline for increased robustness as well as accuracy.

While significant progress has been made in incorporating the spatial contextual information and understanding its impact on enhanced deconvolution

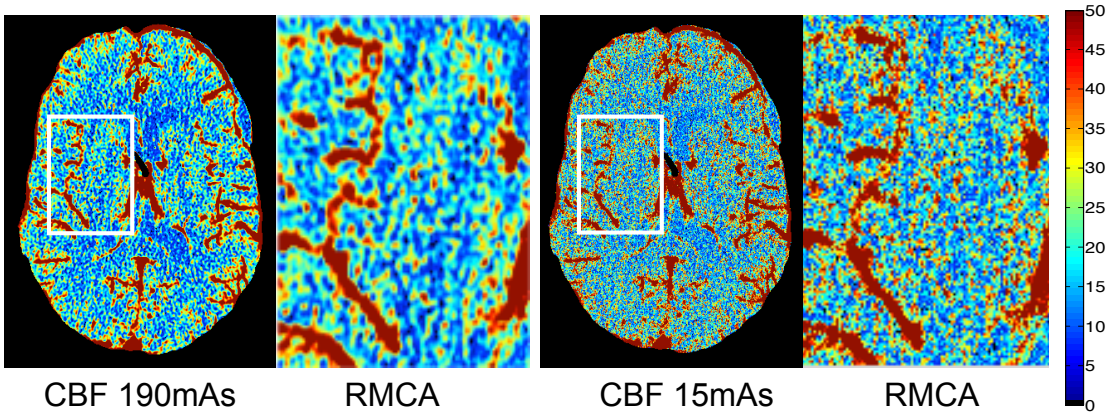

Figure 1.2: High- and low-dose cerebral blood flow maps at 190 mA and 15 mA tube current levels.

of hemodynamic parameters, we believe there are several aspects of spatial contextual information that have been largely ignored. These are the aspects explored in this thesis. For instance, the spatial context has mostly been exploited within the same subject to incorporate spatial smoothness or boundaries. We study the scenarios under which spatial context across subjects is really necessary, and most beneficial to close the gap between high- and low-dose images through dictionary learning and sparse representation. Spatial context has mostly been explored for the whole image globally. We explore the role of tissue-specific spatial context by segmenting the different tissue types and learn corresponding dictionaries. And finally, most works employ the spatial contextual information in cerebral blood flow which is the most significant indicator of infraction and ischemic penumbra. We investigate how this robust deconvolution framework can be generalized to other hemodynamic parameters, such as blood-brain-barrier permeability. We also use tensor total variation regularizer to robustly estimate the impulse response function, thus all hemodynamic parameters can be computed simultaneously.

The rest of this thesis is organized as follows. Chapter 2 describes our work on studying robust medical *informatics* acquisition. Chapter 3 presents our work on exploring how disease *diagnosis* can benefit from robust deconvolution. Chapter 4 and Chapter 5 present our approach to generalize robust hemodynamic parameter estimation to blood-brain-barrier permeability and other dynamics for *treamtent* plan decision. We provide an introduction and relevant background for each of these three aspects in their relevant chapters. The thesis is concluded in Chapter 6 with a discussion of potential future work.

1.1 First Published Appearances of Described Contributions

Most contributions or their initial versions described in this thesis have first appeared ias various publications:

1. Chapter 2: Fang, Chen, Sanelli [23, 27, 24]
2. Chapter 3: Fang, Chen, Sanelli [26]
3. Chapter 4: Fang, Chen, Sanelli [30]
4. Chapter 5: Fang, Sanelli, Chen [31]

The following contributions have appeared in various publications: Fang, Chen, Zabih, Chen [28]; Fang, Zabih, Raj, Chen [33]; Fang, Raj, Chen, Sanelli [25]; Fang, Tang, Snavely, Chen [32]; Fang, Gallagher, Chen, Loui [29]. However, they are beyond the scope of this dissertation, and therefore are not discussed here.

CHAPTER 2

MEDICAL INFORMATICS: SPARSE PERFUSION DECONVOLUTION

Summary

Computed tomography perfusion (CTP) is an important functional imaging modality in the evaluation of cerebrovascular diseases, particularly in acute stroke and vasospasm. However, the post-processed parametric maps of blood flow tend to be noisy, especially in low-dose CTP, due to the noisy contrast enhancement profile and the oscillatory nature of the results generated by the current computational methods. In this chapter, we propose a robust sparse perfusion deconvolution method (SPD) to estimate cerebral blood flow in CTP performed at low radiation dose. We first build a dictionary from high-dose perfusion maps using online dictionary learning and then perform deconvolution-based hemodynamic parameters estimation on the low-dose CTP data. Our method is validated on clinical data of patients with normal and pathological CBF maps. The results show that we achieve superior performance than existing methods, and potentially improve the differentiation between normal and ischemic tissue in the brain.

2.1 Introduction

Stroke is the third-leading cause of death in the United States after heart disease and cancer. Early and rapid diagnosis of stroke can save critical time for thrombolytic therapy. Cerebral perfusion imaging via computed tomography

perfusion (CTP) has become more commonly used in clinical practice for the evaluation of patients with cerebrovascular disease such as acute stroke and vasospasm after subarachnoid hemorrhage (SAH) [76, 56, 44]. Various mathematical models have been used to process the acquired temporal data to ascertain quantitative information, such as cerebral blood flow (CBF), cerebral blood volume (CBV) and mean transit time (MTT), with higher radiation dosage compared to a standard CT of the head [80, 81, 44, 42, 105, 43]. However, recent reports on the over-exposure of radiation in CTP imaging have brought the dosage problem to the limelight because many patients suffered biologic effects from radiation exposure, including hair loss, skin burns and even cancer risk [102]. A key challenge in CTP is to obtain a high-quality CBF image using low radiation dose.

The most commonly used deconvolution method to quantify the perfusion parameters in CTP is truncated singular value decomposition (TSVD) and its variants, such as circular TSVD (cTSVD) [9, 10, 81, 80, 108, 105]. When TSVD deconvolution algorithm was first introduced in 1996, it calculates the perfusion parameters for each tissue voxel independently. It assumes the X-ray radiation and intravenous injection were high enough to generate accurate tissue enhancement curve (TEC) and arterial input function (AIF) for deconvolution. However, TSVD-based methods tend to introduce unwanted oscillations [7, 77] and results in overestimation of perfusion parameters, particularly CBF. Numerous works have been proposed to denoise the reconstructed CT images and therefore successfully improved the quality of CBF maps, including bilateral filtering [75], non-local mean [66], nonlinear diffusion filter [87], and wavelet-based methods [61]. However, these works improve the quality of the reconstructed CT data only and do not take the convolution flow model of CTP

into consideration. The oscillatory nature of the TSVD-based method has initiated research that incorporates different regularization methods to stabilize the deconvolution, and have shown varying degrees of success in stabilizing the residue functions by enforcing both temporal [7, 79, 2, 106] and spatial regularization [43, 24] on the residue function. However, prior studies have focused exclusively on imposing regularizations on the noisy low-dose CTP, without considering the corpus of high-dose CTP data.

Since perfusion images tend to be noisy at low-dose, our aim is to develop a method to perform deconvolution-based first-pass hemodynamic parameter estimation that is more robust to noisy input at low radiation dosage by learning from high-dose data, and to produce perfusion parameter maps with better signal-to-noise characteristics. To that end, we have developed a formulation that utilizes a sparse representation functional to enforce both temporal convolution and spatial regularization using example-based restoration learned from high-dose CTP parametric maps. Because TSVD-based approaches estimate the residue function (and hence the perfusion parameters) for each voxel independently of its neighbors, our sparse perfusion deconvolution approach with dictionaries learned from high-dose perfusion maps mitigates the noise issue associated with the traditional approaches. Although sparse representation image models have been used in several context [1, 70], to date we are not aware of any such work in the context of perfusion parameter estimation to bridge the gap between high- and low-dose CTP data.

In this chapter, we propose a robust sparsity-based deconvolution method to estimate CBF in CTP at low radiation dose We first learned a dictionary of CBF maps from a corpus of high-dose CTP data using online dictionary learning

and then perform deconvolution-based hemodynamic parameter estimation of the low-dose CTP. This method produces perfusion parameter maps with better signal-to-noise characteristics.

The main contributions of our work are threefold: (1) We propose to train a dictionary of perfusion parameter maps from the high-dose CT data in an online fashion to improve the quantification of low-dose CTP. (2) We combine the temporal convolution model with the dictionary mapping term and the sparsity term to enforce spatio-temporal regularization. (3) In vivo brain aneurysmal SAH patient data, we demonstrate that our estimated CBF values lead to better separation between ischemic tissue — which by its angiogenic nature tends to have less blood flow — and normal tissue.

2.2 Related work

Since we use sparsity prior and example-based restoration to enhance low-dose perfusion CT images, we review relevant work in both sparsity prior and example-based restoration work.

2.2.1 Sparsity prior and dictionary learning

Sparsity methods have been vastly investigated in recent years. [8] and [17] have shown that a sparse signal can be recovered from a small number of its linear measurements with high probability. Various greedy algorithms have been proposed to solve the problems with sparsity priors, including basis pursuit (BP) [12], matching pursuit [71], orthogonal maching pursuit (OMP) [11] and

stagewise OMP (stOMP) [16]. Another approach is to use l_1 norm relaxation and convex optimization [8, 54, 35], which is employed in our work.

Sparse representation and dictionary learning has been widely used in computer vision and multimedia communities, such as, but not limited to, natural image and video denosing [20, 85], image restoration [69], image super-resolution [109], robust face recognition [107], automatic image annotation [115]. In medical image analysis, sparsity prior has been applied to MR reconstruction [65, 45], shape modeling [114], deformable segmentation [117], etc. However, to the best of our knowledge, it is the first time sparse prior and learned dictionaries are used in a spatio-temporal model to address the challenging task of low-dose CTP enhancement. The sparsity prior leads to more robust solution in face of overcomplete bases in signal recovery, and removes noise existent in the captured signal. Specifically, [107] have shown that sparse representation is critical for high-performance classification of high-dimensional data, and occlusion and corruption can be handled uniformly and robustly with this framework.

To learn a compact representation from the original dataset due to computational cost when the training datasets have thousands or millions of samples, extensive studies in dictionary learning have been done. A brief introduction of the relevant algorithms are presented here. Dictionary learning typically consists of two steps: sparse coding and codebook update. Sparse coding can implemented using greedy algorithms such as matching pursuit (MP) [71] and orthogonal matching pursuit (OMP) [11] by finding the sparsest coefficients. And codebook update employs optimal direction (MOD) [21], K-SVD [1] or the recently proposed online dictionary learning [68]. Online dictionary learning

is used in this work because it can handle large training dataset with higher efficiency and achieves more robust dictionary compared to MOD and K-SVD.

2.2.2 Example-based Restoration

Redundancy representation and sparsity have been the driving forces for signal denoising for the research in the past decades or so, leading to what is considered today as some of the best available image denoising methods [84, 90, 22, 73]. While this work is built on the very same concept of sparsity and redundancy concepts for restoration, it is adopting a different point of view, drawing resources from yet another recent line of work on example-based restoration. Traditionally, the image prior to address the general inverse problem in image processing using Bayesian approach has been based on some simplifying assumptions, such as spatial smoothness, low/max-entropy, or sparsity in transform domain. On the other hand, example-based approach resorts to the images themselves for the optimal prior, for instance, using a spatial-smoothness based Markov random field prior and training the derivative filters for image restoration [118, 86]. Example-based restoration has been applied to image and video denoising [20, 70, 85], image super-resolution [38], shape representation and segmentation [114, 117]. We introduce the concept of example-based restoration into low-dose perfusion CT enhancement by learning the prior from the high-dose perfusion maps.

2.3 Methodology

In this section, we present the new sparse perfusion deconvolution (SPD) framework for CTP quantification. The framework is comprised of two steps: online dictionary learning and sparse perfusion deconvolution.

2.3.1 Perfusion parameter model

Based on the theoretical model provided in [81], in CTP, the amount of contrast in the region is characterized by

$$C_v(t) = CBF \int_0^t C_a(\tau) R(t-\tau) d\tau, \tag{2.1}$$

where $C_v(t)$ is the tissue enhancement curve (TEC) of tracer at the venous output in the volume of interest (VOI), CBF is the cerebral blood flow, $C_a(t)$ is an arterial input function (AIF) and $R(t)$ is the tissue impulse residue function (IRF), which measures the mass of contrast media remaining in the given vascular network over time. Under this model, at time $t = t_0$, a unit of contrast agent is injected as a bolus, and $R(t = t_0) = 1$ indicates that the entire mass of contrast agent is within the vascular network. After a finite duration (t_N) when all contrast has left the vascular network, $R(t = t_N) = 0$.

To discretize the computation, we assume that $C_a(t)$ and $C(t)$ are measured with N equally spaced time points t_1, t_2, ..., t_N with time increment Δt. The convolution is discretized

$$\mathbf{C} = CBF \cdot \Delta t \cdot C_a \cdot \mathbf{R}, \tag{2.2}$$

where

$$\mathbf{C} = \begin{pmatrix} C(t_1) \\ C(t_2) \\ \vdots \\ C(t_N) \end{pmatrix} \qquad \mathbf{R} = \begin{pmatrix} R(t_1) \\ R(t_2) \\ \vdots \\ R(t_N) \end{pmatrix}$$

and

$$\mathbf{C_a} = \begin{pmatrix} C_a(t_1) & 0 & \dots & 0 \\ C_a(t_2) & C_a(t_1) & \cdots & 0 \\ \vdots & \vdots & \ddots & \vdots \\ C_a(t_N) & C_a(t_{N-1}) & \cdots & C_a(t_1) \end{pmatrix}$$

When $R(t)$ is estimated from Eq. (2.2), CBF can be computed from

$$CBF = R(t = 0) \tag{2.3}$$

since from the definition of the residue function $R(t)$, $R(t = 0) = 1$.

2.3.2 Circulant truncated singular value decomposition

Singular value decomposition is a widely adopted approach to estimate the perfusion parameter maps [81, 9, 10], where matrix C_a is factorized into two orthogonal matrices $\mathbf{U}$ and $\mathbf{V^T}$ and a diagonal matrix $\mathbf{S}$, with n singular values, s_i, $i = 1, 2, , n$ in descending order along the diagonal

$$\mathbf{C_a} = \mathbf{USV^T} \tag{2.4}$$

Eq. (2.2) can be rewritten as

$$CBF \cdot \Delta t \cdot \mathbf{R} = \mathbf{VS^TU^T} \cdot \mathbf{C} \tag{2.5}$$

Because smaller singular values related to the higher frequency singular values and the reciprocal of these small singular values lead to large weighting coefficients of oscillatory singular vectors, TSVD regularized the solution by truncating small singular values to zero using a threshold λ and therefore remove the corresponding oscillatory terms from the solution. In this chapter, we set parameter λ=0.3 (30% of the maximum element in $\mathbf{S}$) based on the experimental analysis in [34]. Delay and dispersions between the AIF and tissue VOI can lead to inaccurate estimation of perfusion parameters, especially when contrast agents arrive earlier in the tissue than in the chosen AIF. Therefore in this chapter block-circulant version of Ca matrix is used instead of linear deconvolution to avoid the causality problem.

2.3.3 Proposed sparse perfusion deconvolution with online dictionary learning (ODL-SPD)

Sparse representations over trained dictionaries for perfusion parameter maps restoration rest on the assumption that the image priors in the perfusion maps can be learned from images, rather than choosing a prior based on some simplifying assumptions, such as spatial smoothness, non-local similarity, or sparsity in the transform domain. Since the low-dose CTP has high noise level in TEC, it is important to learn the dictionaries from the high-dose (thus low noise level) CTP. Therefore, we implement the sparse and redundant representation in the spirit of Sparseland [20]. In our model, we estimate perfusion parameters by considering both temporal correlations and example-based restoration using dictionaries learned from high-dose data.

Basic framework: Suppose $C(x, y, z, t) \in \mathbb{R}^{N \times T}$ is TEC in VOI $[x, y, z]^T$ from a spatial-temporal patch of size $\sqrt{N} \times \sqrt{N} \times 1$ pixels and T time points. $R(x, y, z, t) \in \mathbb{R}^{N \times T}$ represent the remaining tracer concentration of the voxel $[x, y, z]$ at a given time point t, where x, y and z are the respective row, column and slice coordinates of the spatial-temporal data. The least-square form of Eq. (2.2) is

$$J_{ls} = \|\mathbf{C} - \mathbf{C_a}\mathbf{R}\|_2^2 \tag{2.6}$$

By definition, CBF map can be computed using $f = R(t = 0)$, where $f \in \mathbb{R}^N$ indicates a vector of patch in the CBF map by stacking the pixels vertically.

Due to the noise in the low-dose CTP data, the solution of Eq. (2.6) may be severely distorted. To utilize the high-dose repository existent as a prior, we first learn a compact dictionary $D \in \mathbb{R}^{N \times K}$ from the existing high-dose CBF maps, where K is the number of patches in D and N is the number of pixels in each patch. f is the vector of a newly-input patch which needs to be constrained or refined. Our basic framework assumes any input patch can be approximately represented as a weighted linear combination of the patches in the learned dictionary D. We denote $\alpha = [\alpha_1, \alpha_2, \ldots, \alpha_K]^T \in \mathbb{R}^K$ as the coefficients or weights. Thus the values of α for the linear combination is found by minimizing the following loss function:

$$J_{basic} = \mu_1 \|\mathbf{C} - \mathbf{C_a}\mathbf{R}\|_2^2 + \|f - \mathbf{D}\alpha\|_2^2 \tag{2.7}$$

where μ_1 indicates the importance of the temporal correlation term in the loss function. f and α are computed by solving Eq. (2.7).

Sparse linear combination: The limitations of Eq. (2.7) are twofold. First the dictionary D may be overcomplete ($K > N$) when the number of atoms is larger than the length of f. Thus the system may not have a unique solution. More

constraints of the coefficient α are needed. Second, the input patch, including the noises, may be perfectly represented if any linear combination can be used. A more approximate assumption is that the input patch can be approximately represented by a *sparse* linear combination of the dictionary atoms. Thus in the spirit of Sparseland model, the problem is reformulated as:

$$J = \mu_1 \|\mathbf{C} - \mathbf{C_a}\mathbf{R}\|_2^2 + \|f - \mathbf{D}\alpha\|_2^2 \tag{2.8}$$
$$s.t. \|\alpha\|_0 \leq k$$

where $\|\cdot\|_0$ is the l_0 norm counting the nonzero entries of a vector, k is the predefined sparsity number. Such formulation ensures that the number of nonzero elements in α is smaller than k. The value of k depends on specific applications.

Convex relaxation: The constraints in Eq. (2.8) are not directly tractable because of nonconvexity of l_0 norm. Greedy algorithms can be applied to this NP-hard l_0 norm minimization problem, as in [23], but there is no guarantee to capture the global minima. In the general case, no known procedure can correctly find the sparsest solution more efficiently than exhausting all subsets of the entries for f. Thanks to the recent proof of the sparse representation theorem [17], l_1 norm relaxation can be employed to make the problem convex while still preserving the sparsity property. Thus Eq. (2.8) is reformulated as

$$J = \mu_1 \|\mathbf{C} - \mathbf{C_a}\mathbf{R}\|_2^2 + \|f - \mathbf{D}\alpha\|_2^2 + \mu_2 \|\alpha\|_1 \tag{2.9}$$

where μ_1 and μ_2 controls the weight of the temporal term and how sparse α is. Since the deviation from Eq. (2.8) to (2.9) relaxes the absolute sparseness constraints of the objective function (l_0 norm to l_1 norm), and converts a NP hard problem to a continuous and convex optimization problem, which can be solved efficiently, it paves the way for a feasible spatio-temporal deconvolution procedure as described later.

Connections to other methods: It is interesting to look in Eq. (2.9) by adjusting μ_1 and μ_2 into some extreme values.

- If μ_1 is extremely large, the temporal correlation term dominates. Thus SPD is similar to methods that do not model spatial regularization.
- If μ_1 is extremely small, the temporal correlation is no longer a constraint. With proper initialization, SPD becomes the imaging denoising method using learned dictionaries.
- If μ_2 is very large, may have only one non-zero element. Thus SPD becomes the nearest neighbor method.
- If μ_2 is very small, the sparsity constraint no longer exists. A dense linear combination of atoms is used, which is able to perfectly approximate the low-dose perfusion parameter map.

Parameter settings: Eq. (2.9) has two user tunable parameters μ_1 and μ_2, which are usually crucial to the performance and convergence. It is desirable to have parameters easy to tune and insensitive to different data in one application from a practical view. Fortunately the parameters in our algorithm have a physical meaning and it is straightforward to adjust them. μ_1 controls the weight of the temporal correlation term. A good initialization of CBF map would conform to the temporal correlation model. Thus a small μ_1 is good enough with a warm start. μ_2 controls the sparsity of α. The length of vector α is equal to the number of atoms in the dictionaries. It is usually larger than 200. To generate a sparse coefficient α, a relatively large μ_2 is necessary. Both the parameters are straightforward to tune given their meanings.

Vessel and non-vessel threshold: To further improve the signal-to-noise ra-

tio for different types of tissue, which have different physiological structures and spatial resolution requirements, we apply different regularization parameters to different tissue types. In this work, we use different parameter settings for vessel and non-vessel voxels. Vessels are identified by setting a threshold on the CBF map, e.g. if vessel threshold is 40 mL/100 g/min, then every voxel with at least 40mL/100 g/min CBF value in the brain is marked as vessel. For vessels, we apply low regularization parameters μ_1^l and μ_2^l because vessels have high-contrast boundaries with respect to neighboring regions. For non-vessel voxels, we apply high regularization parameters μ_1^h and μ_2^h because they are expected to be more spatially coherent.

Dictionary learning: To learn the dictionary **D**, we use the recently developed online learning algorithm [68] which solves Eq. (2.9) by processing one sample (or a mini-batch) at a time and updating the dictionary using block coordinate descent with warm restart. We first learn a dictionary by using randomly sampled patches from the CBF perfusion maps estimated from the high-dose CTP data. Given a set of image patches $Z = \{z_j\}_{j=1}^N$, each of $\sqrt{N} \times \sqrt{N} \times 1$, we seek the dictionary **D** that minimizes

$$\arg\min_{\mathbf{D},\mathbf{A}} \sum_{j=1}^{N} \|z_j - \mathbf{D}\alpha_j\|_2^2 + \mu_2\|\alpha_j\|_1, j = 1, \cdots, N \tag{2.10}$$

where A is a matrix formed by $[\alpha_1, \alpha_2, \ldots, \alpha_N]$. To solve Eq. (2.10), we start from an initial dictionary (i.e. the overcomplete DCT dictionary), and CBF parameter map estimated using cTSVD algorithm at high-dose CTP.

Sparse perfusion deconvolution (SPD): When the dictionary **D** is known, the CBF perfusion parametric map from the low-dose CTP data can be estimated using our sparse perfusion deconvolution method by minimizing Eq. (2.9) in an iterative fashion. Our SPD method is divided into two sub-problems: (1)

minimization with respect to α with f fixed, (2) update of f with α fixed as a simplified linear inverse problem.

The first step is sparse coding, which is formulated as

$$\arg\min_{\alpha} \|f - \mathbf{D}\alpha\|_2^2 + \mu_2\|\alpha\|_1 \tag{2.11}$$

Eq. (2.11) can be solved by LARS-Lasso [18].

The second step is to minimize

$$\arg\min_{f} \mu_1\|\mathbf{C} - \mathbf{C_a}\mathbf{R}\|_2^2 + \|f - \mathbf{D}\alpha\|_2^2 \tag{2.12}$$

Because $f = R(t = 0)$, Eq. (2.12) can be rewritten as

$$\arg\min_{f} \mu_1\|\mathbf{C} - \mathbf{C_a}\mathbf{R} \cdot diag(f)\|_2^2 + \|f - \mathbf{D}\alpha\|_2^2 \tag{2.13}$$

where R is the residue functions normalized by f so that $R(t = 0) = 1$. Eq. (2.13) is a quadratic term that has a closed-form solution.

If $vec(\mathbf{B})$ denotes the vector formed by the entries of a matrix $\mathbf{B}$ in column major order, and define $\mathbf{P} = \mathbf{C_a}\mathbf{R}$, then

$$vec(C - C_aR \cdot diag(f)) = vec(\mathbf{C} - \mathbf{P} \cdot diag(f)) = vec(\mathbf{C}) - \mathbf{M}f \tag{2.14}$$

where $\mathbf{M}$ is a $TN \times N$ matrix in form of

$$\mathbf{M} = \begin{pmatrix} P_{.,1} & 0 & \cdots & 0 \\ 0 & P_{.,2} & \cdots & 0 \\ \vdots & \vdots & \ddots & \vdots \\ 0 & 0 & \cdots & P_{.,N} \end{pmatrix}$$

where $\mathbf{P_{.,i}}$ dictates the i^{th} column of matrix $\mathbf{P}$ in its column vector form. Eq. (2.13) can be transformed into the conventional least square problem

$$\arg\min_{f} \|(\mathbf{I_n}; \mu_1\mathbf{M})f - (\mathbf{D}\alpha; \mu_1 vec(\mathbf{C})\|_2^2 \tag{2.15}$$

Let $\mathbf{A} = (\mathbf{I_n}; \mu_1 \mathbf{M})$ and $\mathbf{B} = (\mathbf{D}\alpha; \mu_1 vec(\mathbf{C}))$, we get

$$f = \mathbf{A}^{+}\mathbf{B} \tag{2.16}$$

where $\mathbf{A}^{+}$ is the pseudo-inverse of matrix $\mathbf{A}$, $(.;.)$ denotes a vector or matrix by stacking the arguments vertically.

Two procedures are iteratively employed to obtain $f$and α. Note that theoretically this iterative algorithm might lead to local minima. However, in our extensive experiments (Section 2.4), we did not observe this situation yet. We also observe our results are quite stable with respect to the training dataset.

To address the global CBF deconvolution problem, we use a sliding window of size $\sqrt{N} \times \sqrt{N}$ on the specific slice and overlaps the windows by a step size of one. The final global CBF parametric map is generated by averaging the areas that the windows overlap.

2.4 Experiments

In this section, we describe the results from comparing our online-dictionary-learning sparse perfusion deconvolution (ODL-SPD) with cTSVD and SPD deconvolution using K-SVD learning algorithm (KSVD-SPD) [23]. Out of 20 subjects, 10 are used as training data (7 with CTP deficits in the brain and 3 normal), and the rest 10 are used for testing purpose (5 with CTP deficits and 5 normal). A board-certified neuro-radiologist with 12 years experience reviewed CTP data in a blind fashion to determine the type and location of CTP deficits.

2.4.1 Experiment setup

Data acquisition: CTP was performed during the typical time-period for patients with cerebrovascular disease enrolled in an IRB-approved clinical trial from August 2007 to June 2010, between days 6-8 in asymptomatic patients and on the same day clinical deterioration occurred in symptomatic patients. CTP was performed with a standard scanning protocol at our institution using GE Light speed or Pro-16 scanners (General Electric Medical Systems, Milwaukee, WI) with cine 4i scanning mode and 45 second acquisition at 1 rotation per second using 80 kVp and 190 mA. A scanning volume of 2.0 cm was used consisting of 4 slices at 5.0 mm thickness with its inferior extent selected at the level of the basal ganglia, above the orbits, to minimize radiation exposure to the lenses. Approximately 45 mL of nonionic iodinated contrast was administered intravenously at 5 mL/s using a power injector with a 5 second delay.

Low-dose simulation: Repetitive scanning of the same patient at different radiation doses is unethical. Thereby, Gaussian noise is added to the reconstructed CT images in high-dose CTP to simulate low-dose CTP data at I mA following the practice in [6].

The noise model is built on the inverse relationship between the tube current I (mA) and the noise standard deviation σ in CT images

$$\sigma = \frac{K}{\sqrt{I}} \tag{2.17}$$

The value K is computed by analyzing the Gaussian noise in the CTP images of 22 patients under I_0=190 mA tube current and the average K value is 103.09 $\text{mA}^{1/2}$. Assume I is the simulated tube current level in mA, and σ_0 is the noise standard deviation in CTP images scanned under I_0 mA. We can rewrite

Eq. (2.17) as

$$\frac{\sigma}{\sigma_0} = \frac{\sqrt{I_0}}{\sqrt{I}} \tag{2.18}$$

Because noise distribution is statistically independent, the relationship between σ, σ_0 and the standard deviation of the added Gaussian noise σ_a is

$$\sigma^2 = \sigma_0^2 + \sigma_a^2 \tag{2.19}$$

From Eq. (2.18) and (2.19), we can compute the simulated tube current I given added noise standard deviation σ_a

$$I = \frac{I_0 \cdot \sigma_0^2}{\sigma_0^2 + \sigma_a^2} = \frac{K^2}{\frac{K^2}{I_0} + \sigma_a^2} = \frac{K^2 \cdot I_0}{K^2 + \sigma_a^2 \cdot I_0} \tag{2.20}$$

When $\sigma_a = 25.5$, the simulated low-dose $I = 15$ mA.

Implementation details: We implemented cTSVD, KSVD-SPD and ODL-SPD algorithms in MATLAB and applied them to the clinical CTP data acquired at 190mA (high-dose) and simulated low-dose dataset. All experiments are conducted on a 2.8GHz Intel Core i7 with dual cores MacBook Pro with 4GB memory in MATLAB environment. We download the online dictionary learning for sparse representation code from the authors' website[1].

For all experiments of SPD, the dictionary used are of size 64×256 designed to handle perfusion image patches of 8×8 pixels with 256 atoms in the dictionary. In all experiments, the denoising process uses a sparse coding of each patch of size 8×8 pixels from noisy image.

Evaluation metrics: In this work, we use two metrics to evaluate the performance of the deconvolution algorithms. CBF maps computed from CTP data

[1] http://spams-devel.gforge.inria.fr/

obtained at high tube current of 190 mA were regarded as the reference standard.

Root-mean-square error (RMSE) is a measure of similarity between the CBF at high-dose and low-dose, defined by

$$RMSE = \sqrt{\frac{1}{n}\sum_{i=1}^{n}(f_i - \hat{f}_i)^2} \tag{2.21}$$

where f_i and $\hat{f}_i$, $i = 1, 2, \ldots, n$ are the estimated CBF value at low dose and reference standard CBF value at high dose.

Peak signal-to-noise ratio (PSNR) is widely used in signal and image processing to measure the denoising performance. PSNR is defined as the ratio between the maximum intensity value in the ground truth image I_{max} and the power of corrupting noise σ (RMSE between the ground truth and enhanced image) that affects representation fidelity. PSNR is usually expressed in the logarithmic decibel scale as

$$PSNR = 20\log_{10}\left(\frac{I_{max}}{\sigma}\right) \tag{2.22}$$

2.4.2 Visual comparisons

Comparison of learned dictionaries: Figure 2.1 shows the learned dictionary using K-SVD and ODL. Both dictionaries were trained on a dataset of 10,000 8×8 patches of high-dose CBF perfusion maps and initialized with the redundant DCT dictionary. We could observe from the two dictionaries that the online learned dictionary capture the variety of patterns in the high-dose CTP data, while the dictionary learned using K-SVD has more redundancy in the atoms located in the upper and left corners of the dictionary. K-SVD algorithm solves

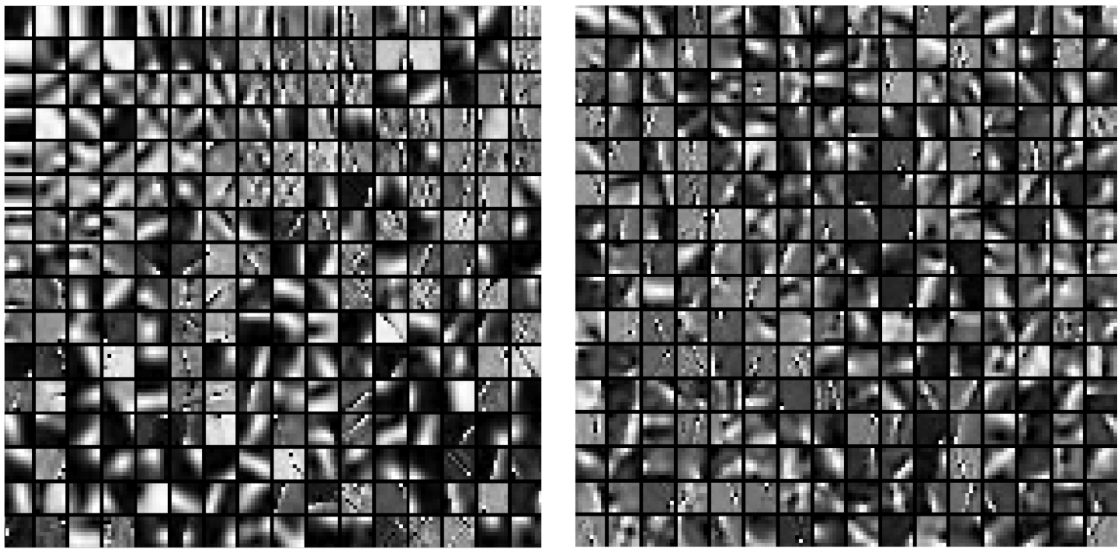

Figure 2.1: Learned dictionaries. Left: K-SVD trained dictionary. Right: Online learned dictionary.

the l_0 norm problem using a greedy codebook update step, which may lead to unstable dictionary due to perturbation in the training data. Online dictionary learning solves a relaxed l_1 norm problem which is convex and therefore results in more robust dictionary. This leads to the differences in the two learned dictionaries. Additionally, online dictionary learning updates the dictionary with one training sample (or a small batch) each time, which scales up gracefully to large datasets with millions of training samples.

Comparison of CBF perfusion maps: We then compare three deconvolution algorithms by visually observing the estimated CBF perfusion maps of two patients, a patient with left middle cerebral artery (LMCA) perfusion deficit on due to vasospasm in an aneurysmal SAH and a patient with normal CBF map. (Please note that in medical practice, the left and right side of the patient are designated opposite on the image). Low tube current of 15 mA was simulated by adding Gaussian noise with standard deviation of 25.5 [6].

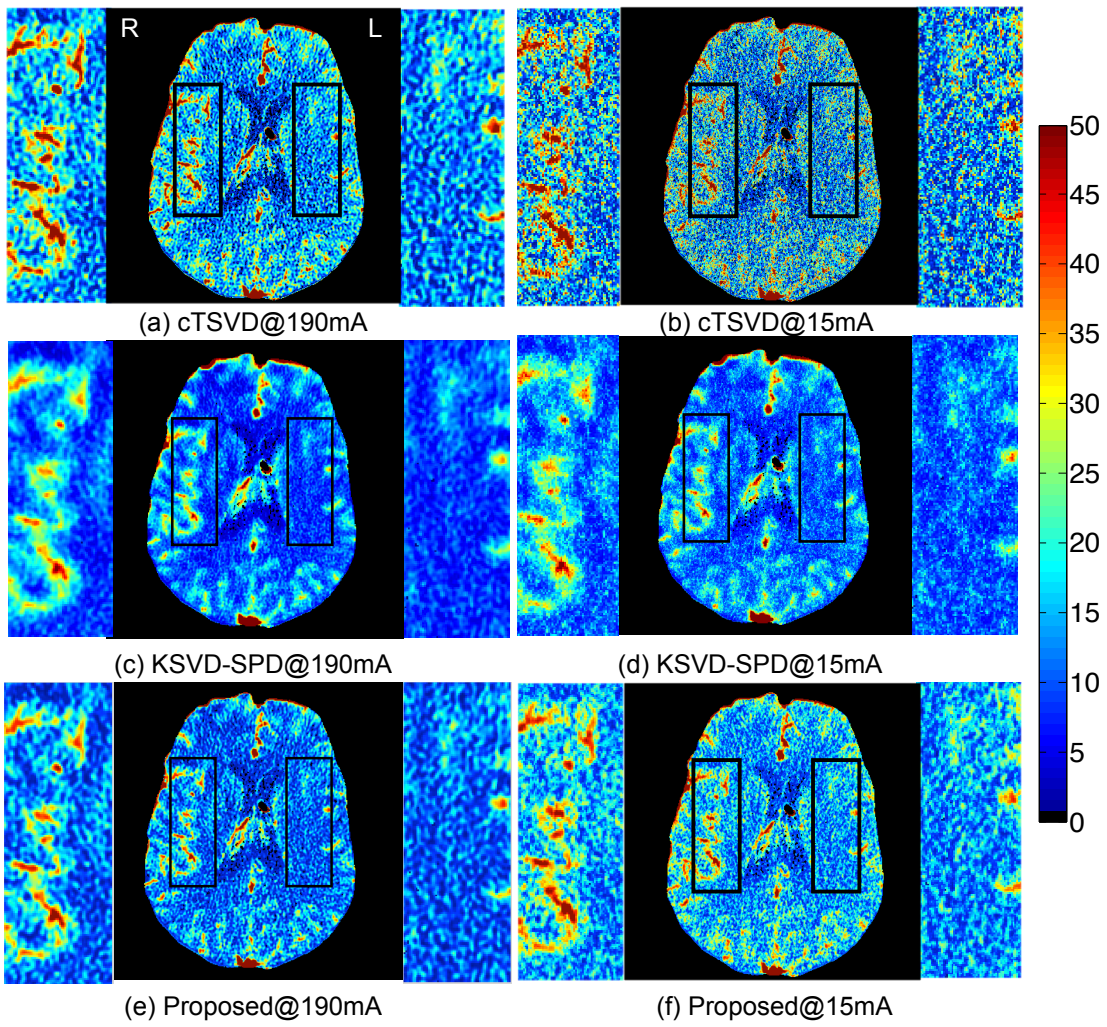

Figure 2.2: CBF maps and zoomed-in regions of a 35-year-old female with left middle cerebral artery (LMCA) perfusion deficit caused by vasospasm in aneurysmal SAH. LMCA and RMCA are enlarged for comparison. The results given by cTSVD, K-SVD SPD and our online SPD are shown in the 1^{st}, 2^{nd} and 3^{rd} row, respectively, each with CBF map of high-dose (190mA) CTP data on the left and that of low-dose (15mA) on the right.

As shown in Figs. 2.2 and 2.3, variations in the locally smooth regions are reduced significantly by our proposed method, while the boundaries between different tissue types and blood vessels are more visible. The arteries and veins are more evidently defined, while the noise in the white matter is greatly sup-

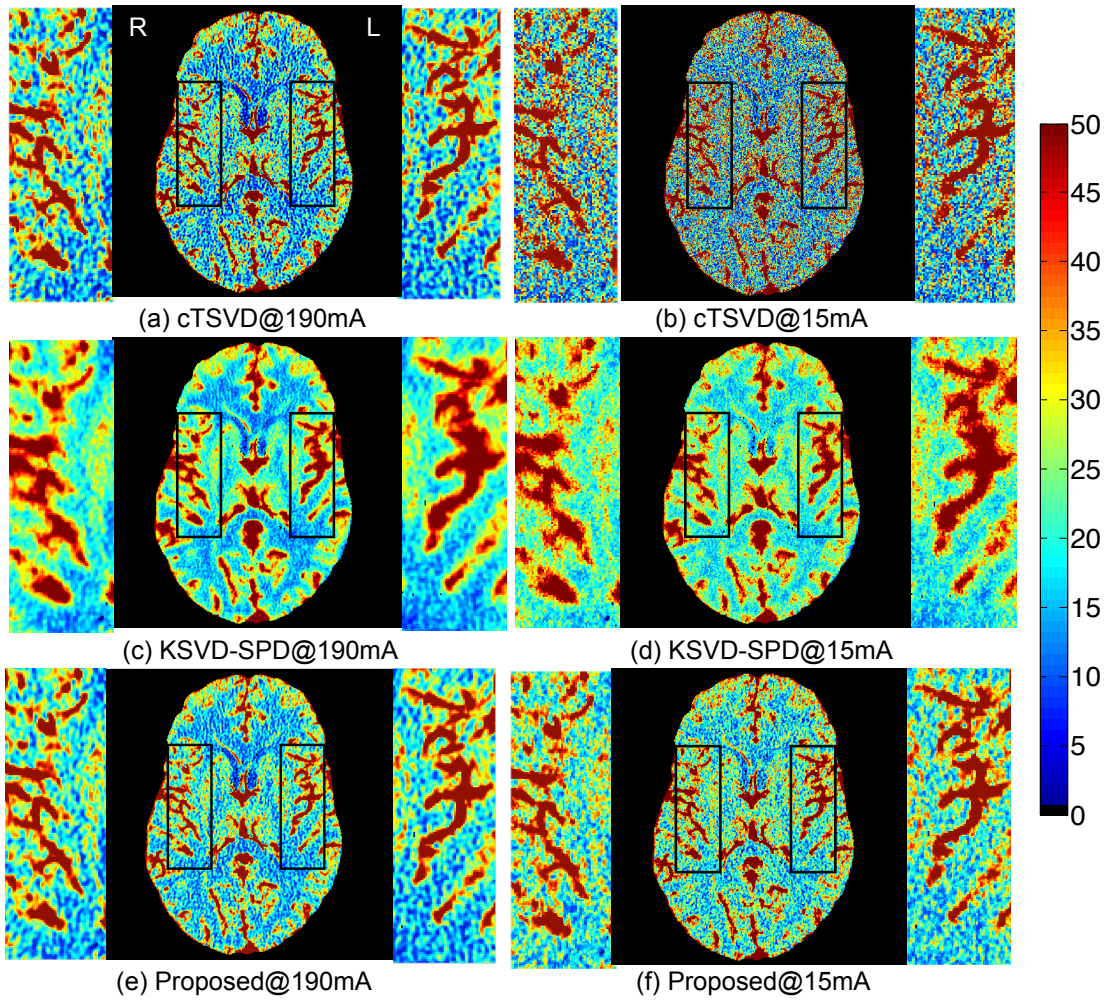

Figure 2.3: CBF maps and zoomed-in regions of a 42-year-old male with normal cerebral blood flow. LMCA and RMCA are enlarged for comparison. The results given by cTSVD, K-SVD SPD and our online SPD are shown in the 1^{st}, 2^{nd} and 3^{rd} row, respectively, each with CBF map of high-dose (190mA) CTP data on the left and that of low-dose (15mA) on the right.

pressed. While both SPD algorithms suppress noise in the CBF maps, KSVD-SPD smoothes the CBF map too much and the vessels in the CBF maps tend to discontinue and the boundaries of the vessels are less clear-cut. The non-vessel tissue also tends to be under-estimated in the aneurysmal SAH patient and to be over-estimated in the normal patient by KSVD-SPD, while our proposed ODL-

Table 2.1: Quantitative comparison of RMSE and PSNR (dB) in CBF maps at low-dose are reports using cTSVD, KSVD-SPD and our proposed method. The average value for the patients with CTP deficits, with normal CTP maps and all data are reported. The best performance of each column is highlighted.

Metric	Method	Fig. 2.2	Fig. 2.3	Deficit	Normal	All data
RMSE	cTSVD	9.47	12.05	12.72±6.45	11.46±3.28	12.09±4.87
	KSVD-SPD	7.99	9.32	10.05±4.33	8.65±1.98	9.35±3.26
	Proposed	**7.23**	**8.74**	**9.24±4.62**	**8.28±2.53**	**7.32±3.54**
PSNR	cTSVD	33.89	34.46	32.95±1.79	31.77±2.30	32.36±2.04
	KSVD-SPD	34.67	36.70	34.71±1.42	34.03±2.31	34.37±1.85
	Proposed	**36.23**	**37.25**	**35.73±1.48**	**34.75±2.36**	**35.24±1.93**

SPD overcomes these drawbacks with an improved learning and reconstruction algorithm, and different regularization parameter setting for vessel and non-vessel voxels.

2.4.3 Quantitative comparisons

To quantitatively compare different methods, we report RMSE and PSNR between the computed perfusion maps and the reference maps of the entire brain region in Table 2.1 for Fig. 2.2, Fig. 2.3 and all test data. Generally cTSVD leads to noisy perfusion maps at low-dose. KSVD-SPD achieves better performance than cTSVD in recovering the high-dose parametric maps, but it over-smooths the texture details in non-vessel structure, especially in patients with

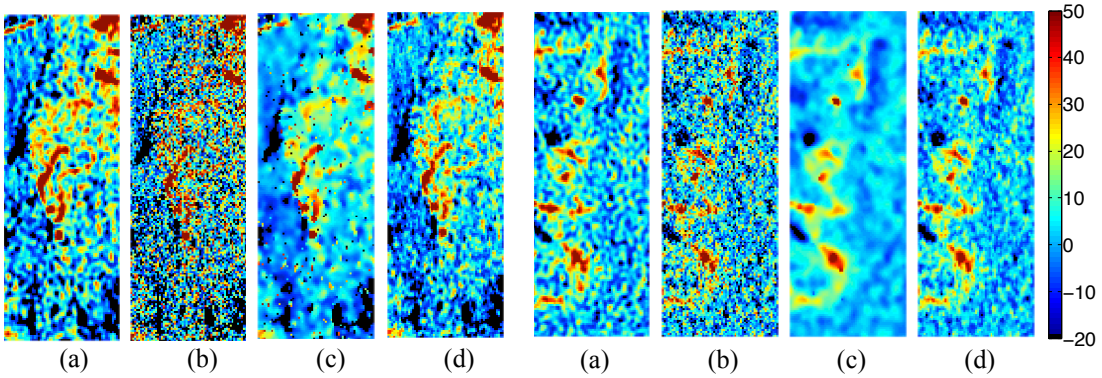

Figure 2.4: Zoomed-in regions of the intensity difference maps between LMCA and RMCA estimated by (a) cTSVD (b) KSVD-SPD and (c) ODL-SPD. Arteries are delineated in red.

CTP deficits. In our proposed method, the robust dictionary and different regularization parameters for vessel and non-vessel structure leads to better performance. It performs the best in terms of both RMSE and PSNR for patients with CTP deficits and normal CTP maps.

2.4.4 Diagnostic analysis

Comparison of asymmetry: As shown in Fig. 2.2, the intensity difference of CBF values between LMCA and right middle cerebral artery (RMCA) is more evident in the low-dose CBF map estimated using our method. To visualize the asymmetry in the left and right middle cerebral artery of this patient, we compute the intensity difference maps between LMCA and RMCA for three deconvolution algorithms, namely cTSVD, KSVD-SPD and ODL-SPD, as shown in Fig. 2.4. We can observe that the intensity different map using cTSVD is too noisy to identify the asymmetry of LMCA and RMCA vessel structures, while KSVD-SPD blurs the details of the vessel structure. Our proposed ODL-

SPD generates the different map with better contrast and spatial resolution for diagnosis of asymmetry in LMCA and RMCA.

Evaluation of ischemic voxels clustering: By aggregating all voxels (within VOI) from the normal hemisphere of the patient data into a single "normal" cluster and the pathologic hemisphere of the ischemia patient data set into an "abnormal" cluster, we have two clusters of n_1 normal voxels and n_2 ischemic voxels. In our case, $n_1 = 877$ and $n_2 = 877$. To quantify the separability between normal and ischemic CBF values, we define the distance between these two clusters as:

$$d = \frac{m_1 - m_2}{\sqrt{\frac{\sigma_1^2}{n_1} + \frac{\sigma_2^2}{n_2}}} \tag{2.23}$$

where m_1, m_2 are the means, and σ_1 and σ_2 are the standard deviations of CBF in the normal and ischemic clusters, respectively. We hypothesized that our ODL-SPD algorithm to produce larger distance d as defined in Eq. (2.23), that is, will more definitely differentiate between normal and ischemic tissues. Fig. 2.5 shows scatter plots of normal versus abnormal cluster. The x coordinate value of each point if the "number of pixels"–increasing pixel number moves from the top-left to the bottom-right of the region of interest as delineated by a radiologist. It is apparent that the two clusters are more separable in data processed via sparse perfusion deconvolution than cTSVD, as shown in Table 2.2. Both SPD algorithms perform better than cTSVD at high-dose and low-dose. Although KSVD-SPD achieves better separability between normal and ischemic tissues, it tends to under-estimate the CBF value of normal tissue, as in Fig. 2.5. At low-dose, ODL-SPD best recovers the CBF values of both normal and ischemic voxels among the three algorithm, and outperforms cTSVD at high-dose by increasing the distance between normal and ischemic voxels.

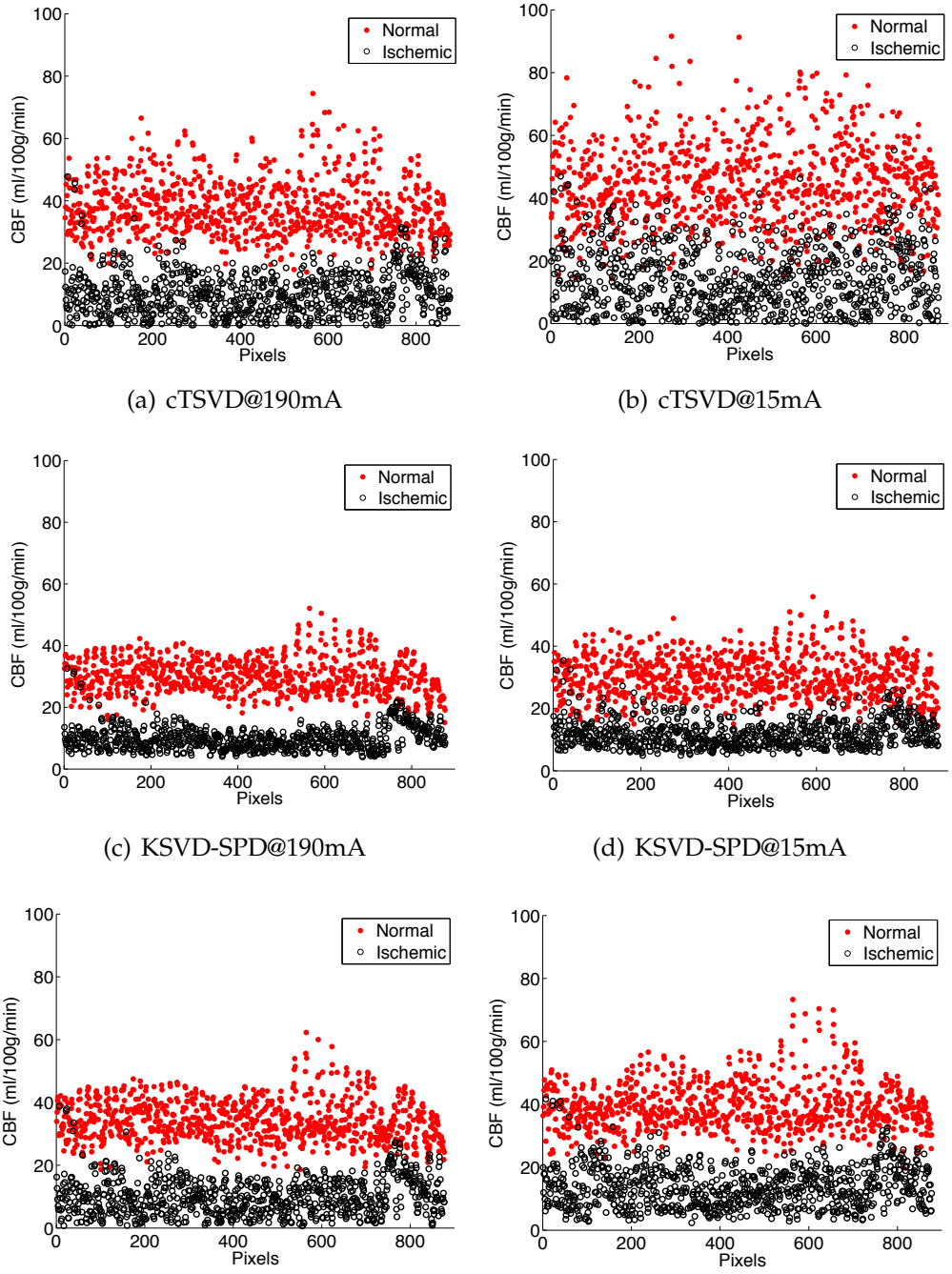

(a) cTSVD@190mA (b) cTSVD@15mA

(c) KSVD-SPD@190mA (d) KSVD-SPD@15mA

(e) Proposed@190mA (f) Proposed@15mA

Figure 2.5: Two clusters of normal vs. ischemic voxels from the aneurysmal SAH patient in Fig. 2.2. The results given by cTSVD, KSVD-SPD and our proposed ODL-SPD are shown in the 1^{st}, 2^{nd} and 3^{rd} row, respectively, each with CBF map of high-dose (190mA) CTP data on the left and that of low-dose (15mA) on the right.

Table 2.2: Normalized distance between ischemic and normal tissues

Distance	190 mA	15 mA
cTSVD	72.24	46.55
KSVD-SPD	86.56	68.37
Proposed	81.98	76.63

Comparison of diagnostic accuracy: Let us define sensitivity as the proportion of samples with abnormal CBF values, which test positive, and specificity as the proportion of samples with normal CBF values that test negative, at a specific threshold. Fig. 2.6 is the receiver operator characteristic (ROC) curve drawn based on 877 abnormal samples and 877 normal samples in which we examine a spectrum of thresholds. The plot shows the tradeoff between true positive rate (sensitivity) and false positive rate (1-specificity). The closer the curve is to the upper left corner, the more accurate the test. Fig. 2.6 shows that ODL-SPD appears to be considerably more accurate than cTSVD and KSVD-SPD, leading to more efficient diagnosis.

2.4.5 Parameter influence

Recall that the balance between the temporal convolution model and the dictionary matching is controlled by the parameter μ_1, while the sparsity of the dictionary selection vector α is controlled by parameter μ_2. Table 2.3 shows the average PSNR at different values of μ_1 and μ_2. Our algorithm consistently achieves similar performance. When $\mu_1^h = 0.02$, $\mu_1^l = 0.01$ and $\mu_2^h = 0.8$, $\mu_2^l = 0.4$,

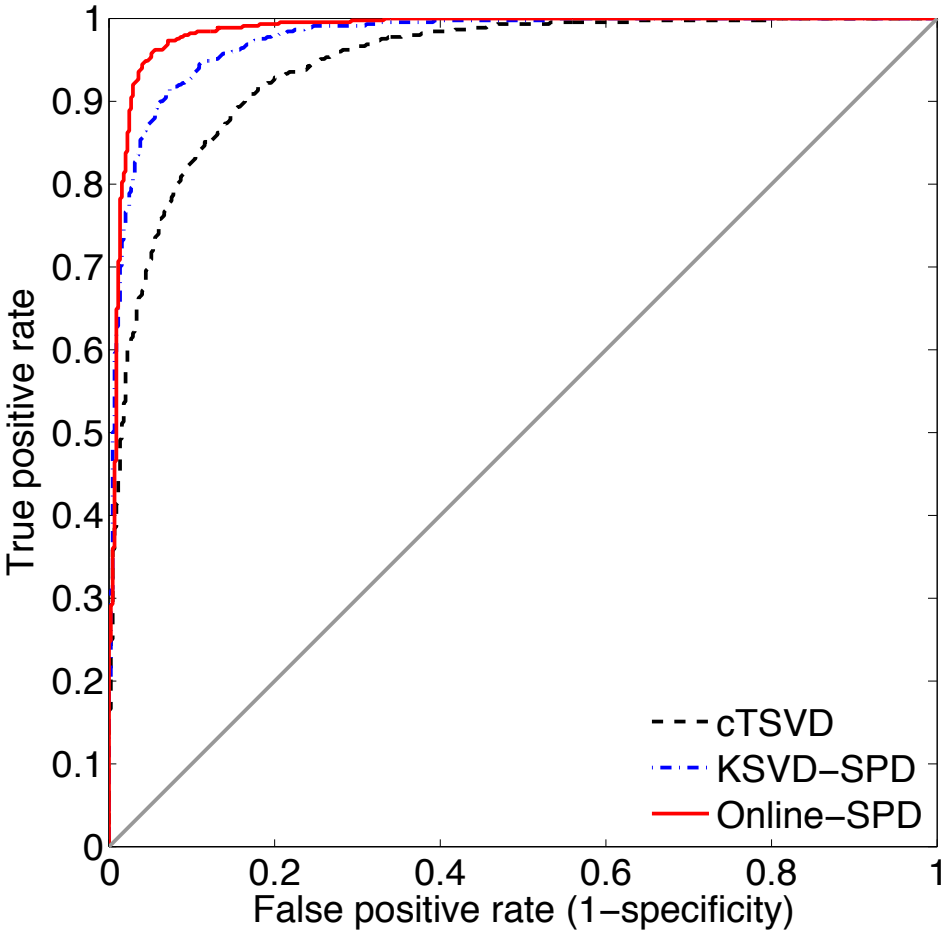

Figure 2.6: ROC curves generated by cTSVD, KSVD-SPD and ODL-SPD deconvolution algorithms. Area under curve (AUC) of cTSVD is 0.9483, the AUC of KSVD-SPD is 0.9749 and the AUC of online-SPD is 0.9852.

the algorithm provides the best CBF estimation at low-dose in terms of PSNR. Table 2.4 and 2.5 shows the parameter influence of vessel threshold and dictionary size.

The threshold for two tissue types is set as CBF value of 40 mL/100 g/min, which can best differentiate the vessels from other tissue. The dictionary size is 256 when the best performance is achieved. We therefore use this set of parameters throughout all experiments in Section 2.4.2 – 2.4.4.

Table 2.3: The influence of parameters μ_1 and μ_2

μ_1^h	0.005	0.01	**0.02**	0.08	0.1	0.02	0.02
μ_1^l	0.01	0.01	**0.01**	0.01	0.01	0.005	0.02
PSNR	44.30	44.37	**44.57**	43.68	43.53	44.22	43.80
μ_2^h	0.8	0.8	**0.8**	0.8	0.8	0.6	0.9
μ_2^l	0	0.2	**0.4**	0.6	0.8	0.4	0.4
PSNR	42.29	44.41	**44.57**	44.22	43.47	44.39	44.40

Table 2.4: Parameter influence of vessel threshold

Thresh	10	20	30	**40**	50	60
PSNR	42.45	42.56	42.67	**44.57**	44.39	44.36

2.5 Discussion

We validate the proposed algorithm on clinical dataset with CTP deficits and normal CBF maps. The experimental results show the following facts.

1. This implicitly incorporated image reconstruction constraint benefits the quality of recovered low-dose perfusion maps. Such example-based information improves the robustness and accuracy of low-dose deconvolution algorithm, and demonstrate superior performance than existing computational methods.
2. The sparse linear combination of dictionary atoms learned from high-dose perfusion maps is able to well approximate the input low-dose CTP data.

Table 2.5: Parameter influence of dictionary size

K	64	128	**256**	512	1024	2048
PSNR	43.47	44.21	**44.57**	44.33	44.11	44.15

The l_1 norm constraint of the coefficient handles the noise and artifacts at low-dose. Different sparsity regularization parameters are applied to vessels and brain tissue in observation of the different anatomical structures further improves the results.

3. When the number of high-dose perfusion data is huge and comes in sequential fashion, it is infeasible to re-learn the entire dictionary whenever a new training sample becomes available. In this case, online dictionary learning technique is employed so our algorithm can be gracefully scaled-up to contain perfusion map priors from, theoretically, infinite number of training samples.

4. The joint spatio-temporal model overcomes the oscillation in temporal-based models and preserves the spatial image features such as smoothness and boundaries, as well as tissue structures. The proposed spatio-temporal method can be applied to various perfusion maps, such as mean transit time (MTT) and permeability surface product (PS), and different dynamic imaging modalities such as SPECT and MRI, which captures the time sequence images at cine mode. We expect to apply this method to more applications in the future.

We acknowledge the following limitations to this work:

The goal of this work was to enhance parametric maps in low-dose CTP using a model with a "residue" function convolution kernel that relates the input (arterial enhancement) and response (tissue enhancement) [76, 44, 42]. We compared to several existing models including cTSVD and KSVD-SPD, which are based on similar underlying principles but using different approaches to solve the problem. However, we did not assess other models that have been applied to CTP data to calculate perfusion parameters, such as adiabatic approximation to the tissue homogeneity model (AATH) [60, 53]. Future studies are needed to determine whether our proposed algorithm regarding the dictionary learning and sparse reconstruction is also effective for these alternative models.

Another limitation is that the analysis of CTP was predominantly performed on CBF maps and not necessarily CBV and MTT maps. CBV and MTT maps provide important and complementary information for detecting and characterizing the ischemic penumbra in stroke patients. The applicability of our proposed deconvolution algorithm to CBV and MTT maps will need to be considered and verified by additional appropriate studies.

Finally, we acknowledge the limited number of patients for evaluation of the proposed deconvolution algorithm in this work. A large-scale validation including evaluation of different cerebrovascular diseases and patient variety is needed to further validate the proposed algorithm for widespread clinical application.

2.6 Conclusions

In this chapter, we proposed a sparsity-based perfusion deconvolution algorithm for enhancing CBF parameter map estimation in low-dose CTP. We take advantage of the complementary parameter map information available in the high-dose CBF maps from the existing database to recover the missing structural information in the low-dose CTP. This is achieved by a spatio-temporal model, which uses a sparse representation approach based on learned dictionaries from the high-dose CBF maps, combined with the temporal convolution model. This framework is validated on clinical dataset with subjects with abnormal and normal CBF maps. Compared to the existing methods, our sparse perfusion deconvolution algorithm exhibits better performance.

The proposed method can be further extended in two directions. First, in clinical diagnosis, infarct core and penumbra usually locate in low-contrast tissues where the delicate tissue texture are important for neuroradiologists in diagnosis and treatment. Therefore, incorporating tissue segmentation into the reconstruction framework is worth investigating as we would learn *distinctive* dictionaries for tissue types respectively rather than a *global* dictionary. Second, since the scope of sparsity-based perfusion deconvolution is beyond the cerebral blood flow computation, we plan to apply this proposed method to other parametric maps, such as permeability surface maps, and integrate it into other medical imaging modalities.

CHAPTER 3

DISEASE DIAGNOSIS: TISSUE-SPECIFIC SPARSE DECONVOLUTION

Summary

Sparse perfusion deconvolution has been recently proposed to effectively improve the image quality and diagnostic accuracy of low-dose perfusion CT by extracting the complementary information from the high-dose perfusion maps to restore the low-dose using a joint spatio-temporal model. However the low-contrast tissue classes where infarct core and ischemic penumbra usually occur in cerebral perfusion CT tend to be over-smoothed, leading to loss of essential biomarkers. In this chapter, we extend this line of work by introducing tissue-specific sparse deconvolution to preserve the subtle perfusion information in the low-contrast tissue classes by learning tissue-specific dictionaries for each tissue class, and restore the low-dose perfusion maps by joining the tissue segments reconstructed from the corresponding dictionaries. Extensive validation on clinical datasets of patients with cerebrovascular disease demonstrates the superior performance of our proposed method with the advantage of better differentiation between abnormal and normal tissue in these patients.

3.1 Introduction

Computed tomography perfusion (CTP) [76] has been more commonly used in patients with cerebrovascular diseases to characterize tissue perfusion. Specifically, in acute stroke patients, detection of ischemic regions has been a main

focus in the literature. The associated excessive radiation exposure of CTP has aroused great concern due to over-dosage leading to biological effects including hair loss, skin burn and increased cancer risk [102]. Even currently recommended CTP scanning parameters still contribute to increased lifetime cancer risk. Sparse perfusion deconvolution (SPD) [23][27] is a recently proposed method for low-dose CTP deconvolution. Different from previous methods [43][7], whose image prior has been based on some simplifying assumptions, SPD is a data-driven method that restores the input low-dose perfusion map using a spatio-temporal model. The model is regularized by a sparse combination of atoms from a global dictionary learned from the high-dose perfusion maps. In this way, spatial priors are incorporated on-the-fly. SPD is able to remove the noise and can preserve the vascular structure and contrast in low-dose perfusion maps.

Theoretically, a global dictionary is able to capture sufficient image information for different tissue classes, given abundant training data from each class. Learned global dictionaries have been applied to various domains including image super-resolution [109] and deformable shape modeling [117]. However empirically the optimization procedure which minimizes the overall reconstruction error, tends to favor high-contrast patches to the low-contrast ones in both the learning and reconstruction procedures. For medical images, the subtle variations and changes embedded in the low-contrast tissue classes such as white matter can be crucial for disease detection and diagnosis [44].

In this chapter, we propose a tissue-specific sparse deconvolution method to address the limitations above. Our method starts from segmenting the brain into different tissue classes. A modified version of automated model-based tis-

sue classification [98] is employed to segment the brain tissue classes. Then tissue-specific dictionaries are learned from the training segments of each class. Finally we use weighted sparse deconvolution method to restore each tissue class and stitch them together. The extensive experiments demonstrate the superior performance of our method. It is important to note that all the preprocessing methods to denoise the dynamic CT data can be complimented with our proposed deconvolution algorithm to achieve better performance. Although class-specific dictionaries have been studied in other scenarios such as face recognition [113] and medical image segmentation [116], our scenarios and goals are different from these work. They aim to predict labels in recognition and segmentation problems, with one class per example. Our proposed algorithm is for reconstruction purpose, and reconstructive dictionaries allow us to recover the pixels belonging to neighboring tissue classes in the same patch.

Our main contribution is two-fold: (1) Tissue-specific dictionaries for each tissue class are employed in place of the global dictionary to capture the low-contrast tissue class and delicate structural details. (2) Weighted sparse deconvolution based on the probability of the tissue classification is proposed for a unified reconstruction of the low-dose perfusion maps. In vivo brain acute stroke and aneurysmal SAH patients data, we demonstrate the superiority of our proposed method in CBF estimation that leads to better separation between normal and ischemic tissue.

3.2 Related Work

Related studies can be traced to two categories, perfusion CT deconvolution and tissue segmentation. In the former category, most previous studies [43, 7, 79, 2] aim to regularize residue functions or denoise reconstructed CT images using an assumed prior, e.g. Mumford-Shah [43] and anisotropic diffusion [87]. SPD is the first CTP deconvolution method using learned priors and sparse representation theory. Segmentation of anatomical structures in brain imaging has gained increasing importance in clinical studies. A frequently used and very reliable statistical algorithm for MRI employs partial tissue segmentation using a model-based automated expectation-maximization algorithm [98]. [52] uses non-linear deformation to warp the tissue probability maps of MR images to the CT space and decomposes the Hounfield Unit of CT images based on the tissue probability. A combined version of these two methods with robust statistics of the dynamic CT data is developed in this work to segment the brain tissue in CTP.

3.3 Tissue-specific Approach to Sparse Deconvolution

3.3.1 Tissue Classification

We first classify the voxels in the dynamic brain CTP data into four tissue classes: vessel, gray matter (GM), white matter (WM) and cerebrospinal fluid (CSF). Since computational efficiency is very important in our framework for real-time clinical diagnosis, we choose a simple yet effective segmentation ap-

proach by adapting a tissue classification algorithm for MRI [98]. We first compute the median value for each voxel along the temporal axis since different tissue classes have different contrast perfusion characteristics. Expectation-maximization segmentation is employed on the median map to obtain probability maps of GM, WM and CSF, We initialize the bias field to zero and start the iterations by providing the algorithm with a rough prior estimation of the classification. The prior distribution is derived from a digital brain atlas that contains spatially varying prior probability maps for the location of GM, WM and CSF [97]. Affine transformation is employed to warp the prior distributions into the target CT image space. EM algorithm is used to estimate the hidden class labels and the parameters of the model, while contexture information is incorporated by a Markov Random Field (MRF). The reason for choosing median map as a robust measurement of the tissue contrast in CTP is because of its higher tissue contrast compared to other statistics in our experiments. Vessel is segmented by thresholding the original CBF value. The vessel voxels in other tissue probability maps are set to zero to guarantee mutually occlusive segmentations. Tissue probability maps on a representative dataset are shown in Fig. 3.1. The following reconstruction does not heavily depend on the segmentation accuracy, since each tissue dictionary is learned from over 10,000 patches and represents dominant patterns in the training patches.

3.3.2 Tissue-Specific Dictionary Learning

Based on the tissue classification from the previous section, we obtain M sets S_m of training patches, $m = Vessel, GM, WM, CSF$, by classifying a patch y from a training image to class i if more than 50% of voxels in the patch y belongs to

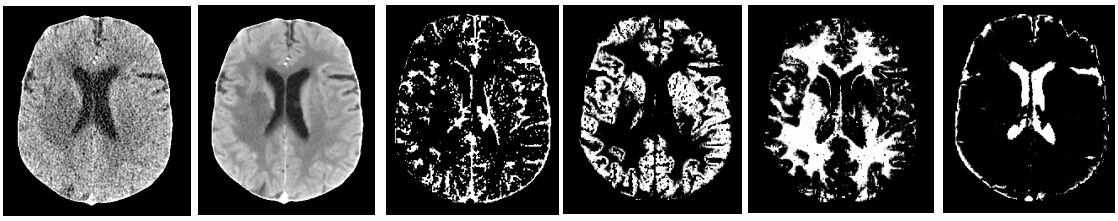

(a) (b) (c) (d) (e) (f)

Figure 3.1: Brain tissue classification by the automatic algorithm on the median map. (a) A slice in the enhanced CTP data (b) Median map. Probability maps of (c) Vessel (d) Gray matter (e) White matter (f) CSF.

class i. Voxels from other classes are then removed from the patch.

To learn the tissue-specific dictionary $\mathbf{D}^m$, $m = Vessel, GM, WM, CSF$, we use the recently developed online learning algorithm [68] which is able to update the dictionary with every batch of new training samples and avoids the time-consuming reconstruction of the entire dictionary when new samples come. Given a set of high-dose CBF patches $Y^m = \{y_i^m\}_{i=1}^N$ for a specific tissue type m, each as a column vector of size N. α_i in R^K is a sparse vector to make $\mathbf{D}\alpha_i$ an approximation to y_i^m with certain error tolerance. $A^m = [\alpha_1, \ldots, \alpha_N]$. We seek the dictionary $\mathbf{D}^m$ in $\mathbf{R}^{N \times K}$ in that minimizes

$$\min_{\mathbf{D}^m, \mathbf{A}^m} \sum_{i=1}^{N} \|y_i^m - \mathbf{D}^m \alpha_i\|_2 + \mu_2 \|\alpha_i\|_1 \tag{3.1}$$

The framework of online dictionary learning is depicted in Algorithm 1. The dictionary is updated efficiently using block-coordinate descent based on stochastic approximation. Because it only exploits a small batch of newly coming data in the dictionary update step, it is therefore much faster than K-SVD or other off-line learning algorithms. Since computational efficiency is very important in our framework, we can efficiently update the tissue-specific dictionaries

Algorithm 1: The framework of online dictionary learning in mini-batch mode.

Input: Initialized dictionary $D_0 \in \mathbf{R}^{n\times k}$, input data $y_i \in \mathbf{R}^n$, number of iterations T, regularization parameter $\lambda \in R$.

Output: Learned dictionary D_T.

$A_0 = 0$, $B_0 = 0$.

for $t = 1 \rightarrow T$ **do**

Randomly draw a set from Y: $y_{t,1}, y_{t,2}, \ldots, y_{t,\tau}$.

for $i = 1 \rightarrow \tau$ **do**

Sparse coding: $\alpha_{t,i} = \arg\min_{\alpha\in\mathbf{R}^k} \frac{1}{2}||y_{t,i} - D_{t-1}\alpha||_2^2 + \lambda||\alpha||_1$.

end for

$A_t = \beta A_{t-1} + \sum_{i=1}^{\tau} \alpha_{t,i}\alpha_{t,i}^T$, $B_t = \beta B_{t-1} + \sum_{i=1}^{\tau} y_{t,i}\alpha_{t,i}^T$,

where $\beta = \frac{\theta+1-\tau}{\theta+1}$, and $\theta = t\tau$ if $t < \tau$, $\theta = \tau^2 + t - \tau$ otherwise.

Dictionary update: Compute D_t, so that:

$\arg\min_D \frac{1}{t}\sigma_{i=1}^{t} \frac{1}{2}||y_i - D\alpha_i||_2^2 + \lambda||\alpha_i||_1 = \arg\min_D \frac{1}{t}(\frac{1}{2}Tr(D^T DA_t) - Tr(D^T B_t))$.

end for

with newly coming data using online learning. Moreover online learning also does not require the loading of all data at the same time, which is unfeasible in clinical practice, and results in less memory cost.

3.3.3 Weighted Sparse Deconvolution

Let's assume dynamic CTP data $\mathbf{C}$ in $\mathbf{R}^{N\times T}$ composed of N tissue enhancement curves (TEC) at voxels of interest (VOI) $[x, y, z]^T$ and T time points. The residue impulse function (RIF) is represented by $\mathbf{R}$ in $\mathbf{R}^{N\times T}$, indicating the delaying of

the remaining contrast tracer in the VOI. f in $\mathbf{R}^N$ is the CBF map to be estimated and $\mathbf{D}$ is the learned dictionary. The deconvolution step in SPD algorithm computes the CBF map of low-dose CTP data using both temporal convolution model and tissue-specific dictionary-based spatial regularization by solving:

$$J = \mu_1 \|\mathbf{C}^m - \mathbf{C_a}\mathbf{R}^m\|_2^2 + \|f^m - \mathbf{D}^m\alpha\|_2^2 + \mu_2\|\alpha\|_1 \tag{3.2}$$

where $\mathbf{C}^m$, $\mathbf{R}^m$, $\mathbf{D}^m$ and f^m are the corresponding TEC, RIF, dictionary and CBF for tissue class m for a patch of size $N \times N$. The final global CBF parametric map is generated by averaging the areas of neighboring patches with overlap of one pixel.

Eq. (3.2) is solved by an EM style algorithm with iterative employment of two processes: 1) sparse coding process which minimizes with respect to α with f fixed, 2) quadratic solver which efficiently minimizes this simplified linear inverse problem, as in [27]. Two procedures are iteratively employed to obtain f^m and α^m for each tissue type. Proper initialization in Eq. (3.2) with the output of cTSVD poses the optimization at a good start point and is supposed to mitigate local minima. We also observe our results are quite stable with respect to the training dataset.

The probability map of each tissue class is obtained by employing the model-based segmentation algorithm [98] on the median map of the low-dose CTP data. For every tissue class m, a tissue-specific patch $\hat{f}_i^m$ is reconstructed using the corresponding tissue-specific dictionary of tissue class m. The patch $\hat{f}_i^m$ is then weighted by the probability map of class m for patch f_i and all probability-weighted tissue-specific patches are summed together to obtain the final reconstruction.

Using tissue-specific dictionaries to enhance low-dose CTP maps, SPD ob-

tains three additional advantages: 1) Segmentation information is incorporated into the dictionary learning and reconstruction. 2) Each tissue type has sufficient atoms in the tissue-specific dictionary to reconstruct. 3) Tissue specific parameter settings can be employed according to the spatial smoothness of each tissue class.

3.4 Experiments

To evaluate the performance of the proposed tissue-specific sparse deconvolution (TS-SPD) method, we apply it to a cerebrovascular disease dataset of 20 cases CTP scanned at tube current 190mA from our medical institute. Out of 20 subjects, 10 are used as training and validation (6 with CTP deficits in the brain and 4 normal), and the remaining 10 are used for testing purpose (5 with CTP deficits and 5 normal). For all experiments of SPD, the dictionary used are of size 64×256 designed to handle perfusion image patches of 8×8 pixels with 256 atoms in the dictionary. We download the online dictionary learning for sparse representation code from the authors' website[1], and the model-based brain segmentation code[2]. The optimal parameters are obtained empirically from the training and validation dataset are: $\mu_1 = 0.01, 0.02, 0.04, 0.08$ and $\mu_2 = 0.2, 0.4, 0.8, 1$ for vessel, GM, WM and CSF. The threshold for vessel segmentation is 70 mL/100g/min on the CBF map, as found to be the optimal value in our empirical experiments.

Since repetitive scanning of the same patient at different radiation doses is unethical, correlated Gaussian noise is added to the high-dose CTP data

[1] http://spams-devel.gforge.inria.fr/
[2] http://sourceforge.net/projects/niftyseg/

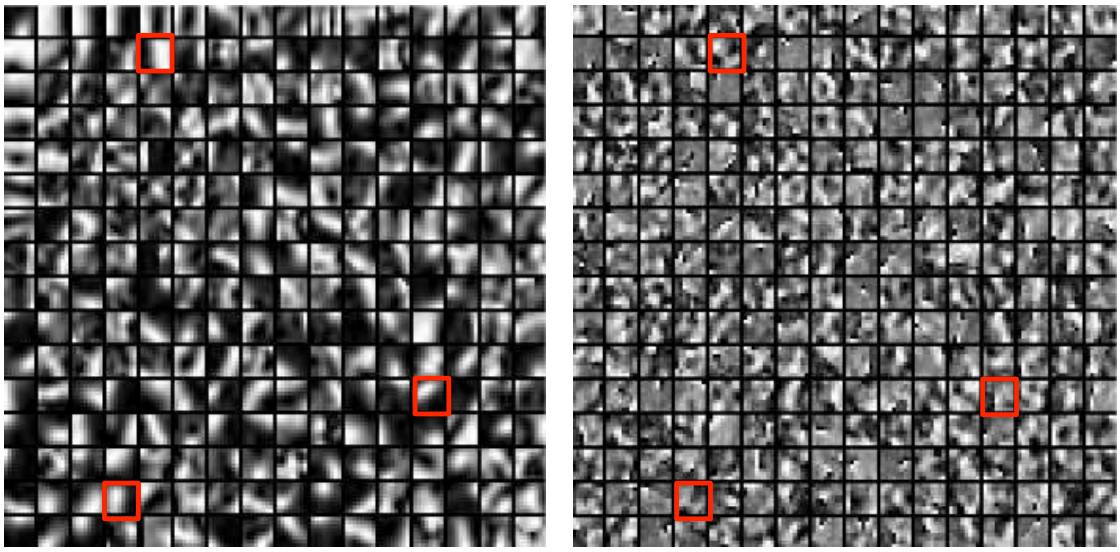

Figure 3.2: Left: Global dictionaries learned using K-SVD. Right: Tissue-specific dictionary for white matter. The global dictionary is dominated by high-contrast, edge-like atoms, while the tissue-specific dictionary for WM has more low-contrast, fine structured atoms, as highlighted by red boxes.

to simulate low-dose CTP data at I mA following the practice in [6]: $I = (K^2 \cdot I_0)/(K^2 + \sigma_a^2 \cdot I_0)$, where σ_a is the standard deviation of the added noise, $I_0 = 190\text{mA}$ is the tube current at high-dose, $K = 103.09\text{mA}^{\frac{1}{2}}$ is a constant. Low tube current of 15.6 mA was simulated by adding correlated Gaussian noise with standard deviation of 25. CBF maps computed from CTP data obtained at high tube current of 190 mA were regarded as the reference standard. We present both the visual and quantitative results to demonstrate performance of the proposed method, with the comparison to cTSVD [105] and KSVD-SPD [23].

Tissue-specific dictionaries: Figure 3.2 shows the globally learned dictionary using K-SVD and the tissue-specific dictionary for white matter. The global dictionary is trained on a dataset of 40,000 8×8 patches of high-dose CBF perfusion maps randomly sampled from 10 training subjects and initialized with

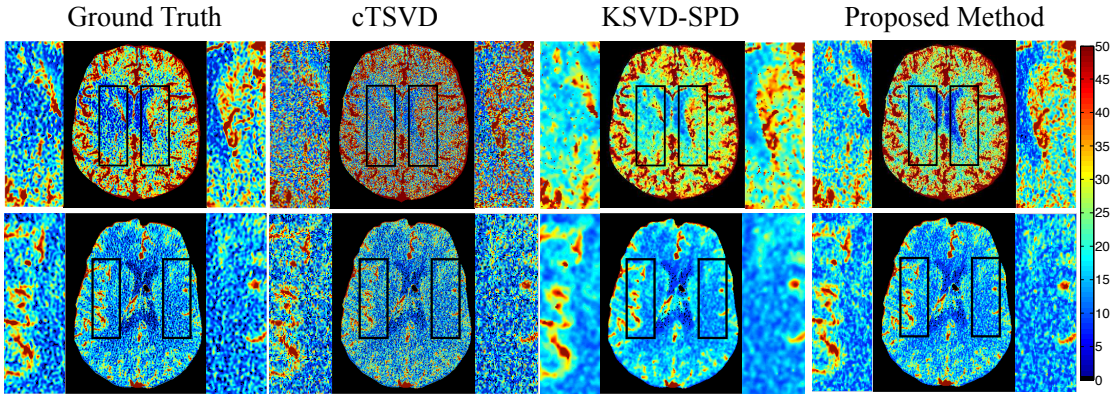

Figure 3.3: CBF maps and zoomed-in regions. A 63-year-old female with acute stroke has an ischemic region in the right hemisphere of the brain (1st row) and a 35-year-old female with left middle cerebral artery (LMCA) perfusion deficit caused by aneurysmal SAH (2nd row). (Note representations in medical images display the sides of the images in reverse order) LMCA and RMCA are enlarged for comparison next to each image. The low-contrast tissue classes in the LMCA and RMCA regions are highly noisy in cTSVD images, and are over-smoothed by KSVD-SPD, while TS-SPD preserves the subtle variations and are closest to the ground truth.

the redundant DCT dictionary. Each tissue-specific dictionary is trained using 10,000 8×8 patches of the corresponding tissue category from the same training subjects. We could observe from the global dictionary that high-contrast patches with edges and corners dominate the dictionary atoms. In comparison, the tissue-specific dictionary for white matter preserves the texture and image characteristics for this tissue class.

CBF perfusion map: We then compare three methods by visually observing the estimated CBF perfusion maps of two patients. As shown in Figs. 3.3, among the three low-dose CBF maps, the CBF maps generated using our proposed TS-SPD algorithm recovers the information of high-dose CBF maps from the low-dose CTP data with best overall performance. The arteries and veins as

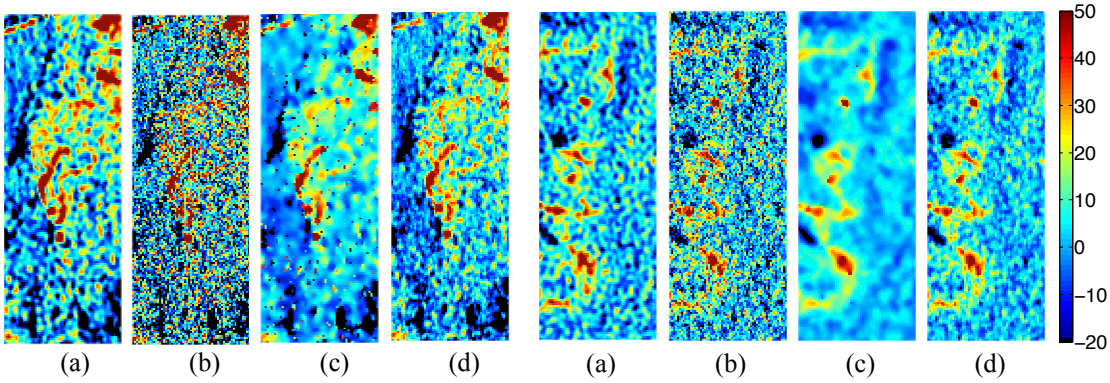

Figure 3.4: Zoomed-in regions of the intensity difference maps between LMCA and RMCA of the acute stroke (left) and SAH (right) patients estimated by (a) Ground truth (b) cTSVD (c) KSVD-SPD (d) Proposed TS-SPD. Arteries are delineated in red, CSF in blue.

well as the micro-vessels are better defined, while the delicate structures of the white matter and CSF are preserved. While the noise is greatly suppressed in the low-dose CBF maps for both enhancement algorithms, KSVD-SPD tends to smooth the image too much, especially the non-vessel structures. Our TS-SPD algorithm overcomes these drawbacks and preserves both the vessel boundaries and the low-contrast structures of WM and CSF with tissue-specific dictionaries and adaptive parameter settings for each tissue class.

Asymmetry: To visualize the asymmetry in the left and right middle cerebral artery in Fig. 3.3, we compute the intensity difference maps between LMCA and RMCA for three methods, as shown in Fig. 3.4. The intensity difference map of cTSVD is too noisy to identify the asymmetry of LMCA and RMCA vessel structures, while KSVD-SPD blurs the details of the vessel structure. The proposed method generates the difference map with better contrast and spatial resolution for diagnosis of asymmetry in LMCA and RMCA.

Table 3.1: Quantitative comparison of PSNR (dB) in CBF maps at low-dose are reported for 10 CTP cases by cTSVD, KSVD-SPD and our TS-SPD. SAH and stroke indicate the two subjects in Fig. 3.3. The best performance is in bold-face type.

PSNR	**Brain**			**GM**			**WM**		
	Stroke	**SAH**	**All data**	**Stroke**	**SAH**	**All data**	**Stroke**	**SAH**	**All data**
cTSVD	43.51	34.87	33.57	12.81	15.94	15.91	19.99	18.65	17.82
KSVD-SPD	45.80	37.11	34.91	17.53	18.08	17.88	22.80	19.75	19.41
TS-SPD	**47.84**	**38.38**	**36.65**	**18.92**	**19.66**	**19.91**	**25.02**	**22.56**	**22.28**

Table 3.2: Quantitative comparison of the normalized distance between ischemic and normal tissue clusters. The best performance of each column is in bold-face type. (Unit: mL/100g/min)

Method	**Stroke**	**SAH**	**All data**
cTSVD	42.71	46.03	49.91±5.12
KSVD-SPD	57.19	53.96	55.62±3.91
TS-SPD	**63.25**	**56.64**	**59.60±3.82**

Quantitative comparisons: We report the PSNR (peak signal-to-noise-ratio) values for two cases in Fig. 3.3 and all testing subjects on the whole brain, GM and WM in Table 3.1. The GM and WM are the tissue regions in the brain affected by stroke and other ischemic processes. The proposed method again achieves the highest PSNR (usually 2~3 dB higher) in all cases, allowing for better discrimination ability of these brain regions, by preserving the tissue structures for differentiation of infarct core and ischemic penumbra in specific regions of the brain assisting neuroradiologists in diagnosis.

Ischemic voxels clustering: We also perform the clustering experiment as

in [23] by aggregating all voxels (within VOI) from the normal hemisphere into a single "normal" cluster and the pathologic hemisphere into an "abnormal" cluster. To quantify the separability between normal and ischemic CBF values, we define the distance between these two clusters as: $d = (m_1 - m_2)/\sqrt{\sigma_1^2/n_1 + \sigma_2^2/n_2}$, where m_1, m_2 are the means, and σ_1 and σ_2 are the standard deviations of CBF in the normal and ischemic clusters, n_1 and n_2 are the number of normal voxels ischemic voxels, respectively. We hypothesized that our TS-SPD algorithm to produce larger distance d, that is, to more definitely differentiate between normal and ischemic tissues. Table 3.2 shows the distance between normal and abnormal clusters for the two cases in Fig. 3.3 and all subjects with CTP deficits. TS-SPD separates the two clusters with greatest distance. One-tail paired t-test yields $p = 0.051$ between cTSVD and KSVD-SPD, and $p = 0.015$ between KSVD-SPD and TS-SPD.

3.5 Conclusion

In this chapter, we have proposed a novel tissue-specific dictionary learning and deconvolution approach for CBF perfusion map enhancement in low-dose cerebral CTP. We take advantage of the distinctive image information of each tissue category available in the high-dose CBF maps to recover the missing texture and structural information in the low-dose CBF maps. This is achieved by performing a spatio-temporal sparse deconvolution based on tissue-specific dictionaries learned from high-dose CBF map segmentation. Our method consistently outperforms the state-of-art methods, especially in GM and WM where the cerebrovascular disease diagnoses mostly rely.

CHAPTER 4

TREATMENT PLAN: BLOOD-BRAIN BARRIER PERMEABILITY ESTIMATION

Summary

Blood-brain barrier permeability (BBBP) measurements extracted from the perfusion computed tomography (PCT) using the Patlak model can be a valuable indicator to predict hemorrhagic transformation in patients with acute stroke. Unfortunately, the standard Patlak model based PCT requires excessive radiation exposure, which raised attention on radiation safety. Minimizing radiation dose is of high value in clinical practice but can degrade the image quality due to the introduced severe noise. The purpose of this work is to construct high quality BBBP maps from low-dose PCT data by using the brain structural similarity between different individuals and the relations between the high- and low-dose maps. The proposed sparse high-dose induced (shd-Patlak) model performs by building a high-dose induced prior for the Patlak model with a set of location adaptive dictionaries, followed by an optimized estimation of BBBP map with the prior regularized Patlak model. Evaluation with the simulated low-dose clinical brain PCT datasets clearly demonstrate that the shd-Patlak model can achieve more significant gains than the standard Patlak model with improved visual quality, higher fidelity to the gold standard and more accurate details for clinical analysis.

4.1 Introduction

As the first leading cause of long-term disability in the United States, stroke imposes a substantial economic burden on individuals and society, with an annual direct and indirect costs totaling US$69 billion in 2006 [63]. Stroke may be ischemic or hemorrhagic and for the former case, intravenous rtPA(alteplase) is an effective treatment widely adopted in clinical practice [14]. However, hemorrhagic transformation (HT) is a serious and potentially fatal complication in patients with acute ischemic stroke, especially for those treated with rtPA [64]. This complication has been and is the hindrance to the administration of the rtPA for this condition [49, 91]. Blood-brain barrier (BBB) breakdown due to ischemia before reperfusion therapy is considered one of the contributing factors to HT in acute ischemic stroke patients [62]. Early detection of a damaged BBB with increased blood-brain barrier permeability (BBBP) could be a valuable tool to identify patients who are more likely to suffer from HT after acute reperfusion therapy, and assist evaluation of the benefits/risks of this treatment [5].

Perfusion computed tomography (PCT) imaging has been advocated to quantify the rate of BBBP [13] from the enhanced time series CT images, with the Patlak model [83]. The standard Patlak model states that a steady-state of contrast levels must be achieved before BBBP assessment, and therefore a delayed PCT acquisition of 240 seconds [15] is required to accurately assess BBBP. The associated excessive radiation exposure of the standard PCT scanning protocol in cine mode for about 1 minute has already raised significant concerns on radiation safety [39, 48, 102], let alone the prolong protocol for BBBP assessment. While effective radiation dose reduction in PCT is an important arena of continuing research efforts, minimizing the reasonable radiation dose for BBBP

assessment is a relatively new topic drawing accumulating research attention.

Up to now, many efforts to reduce radiation dose in PCT have been performed to optimize PCT scanning protocol [36, 104, 101, 111, 50, 3]. Among these techniques, lowering the milliampere-seconds (mAs) is a straightforward and cost-effective method to reduce the radiation dose in PCT. However the associated increased noise in the sinogram will unavoidably lead to quality degradation and the image artifacts in the reconstructed image series and hemodynamic parameter maps. Numerous approaches have been proposed to reduce the noise in the low-dose PCT data, including denoising the sinogram and/or reconstructed image series [75, 66, 67, 87, 61] and regularizing the residue functions in the deconvolution process [7, 79, 2, 106, 43, 24, 27]. However most of these approaches are not addressing the optimization of BBBP map specifically. The interweaving nature of temporal information in the Patlak model and the spatial correlation with the neighborhood tissue is also not effectively utilized.

The standard Patlak model analyzes each voxel in the region of interest independently when a steady-state phase is reached between reversible compartments. It also assumes that the radiation dosage and tracer concentration are high enough to generate high-quality, nearly noise-free tissue density curves (TDC) in the cine-mode scanning. However the noise in the PCT data due to the reduced radiation dose will unavoidably disturb the linearity between the variables in the steady-state phase for Patlak model analysis, thus degrade the accuracy of the permeability calculation. To mitigate the noise issue associated with the standard Patlak model, in this chapter, we develop a spatial-temporal formulation that interweaves the temporal relationship between TDCs of the artery and the tissue, with the spatial similarity between the high- and low-dose

BBBP maps. This is achieved by constructing a dictionary from the repository of high-dose BBBP maps available in the clinical database and imposing a sparsity prior to select a few atoms in the dictionary for the restoration of the low-dose map. In spite of the recent research that bridges the gulf between high- and low-dose perfusion maps such as CBF with a learned dictionary [27], to the best of our knowledge, it is the first attempt to enhance the BBBP map at low radiation dose by improving the standard Patlak model.

The novelty of sparse high-dose induced Patlak model (shd-Patlak) model is threefold. First, shd-Patlak explores the similarity in the brain structure across patients and the specific anatomy at each region of the brain by constructing a location adaptive dictionary from the high-dose maps of different patients. Second, a sparsity term is imposed to the optimization problem in producing the high-dose induced prior as a strategy to select the proper patches for reconstruction. Third, an iterative process with steepest descent algorithm is proposed to optimize the current shd-Patlak model. Qualitative and quantitative evaluations were carried out on the scans of clinical patients in terms of different evaluation metrics.

4.2 Related work

Since sparsity prior is used in the optimization of our works, we review the relevant work on the theoretical background and the application of sparsity prior.

Sparsity approach has inspired much research in recent years. It dates back to 2006 when [17] and [8] showed that with high probability a sparse signal could be reconstructed from a small number of its linear measurements. Since

then, numerous greedy algorithms have been developed to address the sparsity optimization problem. These algorithms include matching pursuit [71], orthogonal matching pursuit (OMP) [11], basis pursuit (BP) [12] and stagewise OMP (stOMP) [17]. Besides the greedy algorithms which solve the L_0 norm problem, relaxation to L_1 norm which is convex has been explored [8, 54, 35], leading to optimization algorithms including LARS-Lasso [96], interior-point [54], etc.

Sparsity prior have been widely applied to computer vision, multimedia processing and medical imaging communities. In the natural image domain, the applications range from the natural image and video denoising [20, 85], image super-resolution [109], image demosaicing and inpainting [70], robust face recognition [107], automatic image annotation [115]. In the medical image domain, sparsity prior has shown its advantage in shape modeling [114], deformable segmentation [117], MR reconstruction [65, 45], etc.

4.3 Background: Patlak model

Patlak model, first described by Patlak et al. [83, 82], is a theoretical model of blood-brain exchange. When a steady-state phase is reached between the reversible (arterial) intravascular and the irreversible extravascular (in this case the brain parenchyma) compartments, transfer of tracer is assumed to be unidirectional. The Patlak plot is a graphical representation of the Patlak model. The rate of transfer between the two compartments is computed from the slope of the linear part of the plot.

The Patlak model is derived from the idea that the total attenuated contrast of a current voxel or region of interest could be represented as a sum of the

tracer in the intravascular and extravascular compartments at a specified time t as:

$$T(t) = CBV \cdot c_{iv}(t) + p \int_0^t c_{iv}(\tau)d\tau = \text{Intravascular} + \text{Extravascular} \tag{4.1}$$

where $T(t)$ is the tissue density curve or tracer at time t, and $c_{iv}(t)$ is the intravascular concentration of the voxel at time t, CBV is the cerebral blood volume. The multiplication of $c_{iv}(t)$ and CBV would yield the total amount of tracer residing in the intravascular component. For the extravascular component, $\int_0^t c_{iv}(\tau)d\tau$ represents the total amount of tracer that perfused the intravascular component from time 0 up till time t, and p is the permeability constant, which is the target of Patlak analysis. The total amount of tracer that leaks from the intravascular to the extravascular component is proportional to the permeability and could be computed via the multiplication of p with $\int_0^t c_{iv}(\tau)d\tau$.

In practice, arterial input function $AIF(t)$ is used as a substitute of $c_{iv}(t)$ since the voxels in the artery contains only an intravascular component. Eq. 4.1 now becomes

$$T(t) = CBV \cdot AIF(t) + p \int_0^t AIF(\tau)d\tau \tag{4.2}$$

By dividing $AIF(t)$ from both sides, the equation yields an easily plotable line in which the slope is p:

$$\frac{T(t)}{AIF(t)} = CBV + p \cdot \frac{\int_0^t AIF(\tau)d\tau}{AIF(t)} \tag{4.3}$$

By setting

$$y = \frac{T(t)}{AIF(t)} \quad \text{and} \quad x = \frac{\int_0^t AIF(\tau)d\tau}{AIF(t)} \tag{4.4}$$

we get

$$y = CBV + p \cdot x \tag{4.5}$$

The slope of a regression line fit to the linear part of the Patlak plot is an approximation of p (the rate of transfer) at time t. The value indicates the amount of accumulated tracer in relation to the amount of tracer that has been available in the plasma and BBBP is expressed in mL×100 g^{-1}×min^{-1}. The y-axis intercept equals CBV. To correct the overestimation of BBBP due to delayed arrival of tracer in the current voxel compared to $AIF(t)$ [15], we shift the time-enhancement curve in each parenchymal voxel to match the arrival time of tracer in the artery [88]:

$$c_{iv}(t) = AIF(t - [TTP(T) - TTP(AIF)]) \tag{4.6}$$

where TTP is the time to peak of a curve. The new $c_{iv}(t)$ replaces the $AIF(t)$ for all delay-corrected calculation.

4.4 Sparse high-dose induced Patlak model

4.4.1 Basic idea

Our key assumption is that image information lost in the low-dose BBBP map due to severe noise could be recovered from the corresponding anatomical regions from the high-dose BBBP maps in the clinical repository. The similarity in the human brain structure and perfusion mechanism makes restoration of missing information of one patient from other individuals possible.

Up till now the BBBP computation with Patlak model is voxel-independent, neglecting the contextual information embedded in the neighboring voxels in the same BBBP map and the similarity between high- and low-dose BBBP maps of different patients. Thus we propose to impose a regularization prior $R(P)$ to the linear regression problem in Eq. 4.5 to improve the quality of BBBP maps, especially at low-dose. In this chapter, following the line of the previous studies for sparsity-based perfusion deconvolution for cerebral blood flow (CBF) map [27] and residue function [24] regularization, we propose a sparse high-dose induced prior for Patlak model ("shd-Patlak") with location adaptive dictionaries constructed from corresponding anatomical regions in the high-dose maps from the existing repository, and an EM style algorithm to solve the maximum a posterior (MAP) optimization. The flowchart of the shd-Patlak model is summarized in Fig. 4.1.

4.4.2 Construction of location adaptive dictionary

The structural similarity between the brains of different individuals motivates us to explore the connections between the high- and low-dose BBBP maps of distinct patients. While patch-based dictionary learning is widely adopted in computer vision for image denoising and super-resolution [20, 70, 110], a global dictionary is usually learned from hundreds of thousands of patches to achieve a universal representation of all the possible patches with enough accuracy. However, the large computational demand in the reconstructed process to evaluate every patch in the global dictionary and the existence of the unnecessary patches in the global dictionary for reconstruction of the patch of interest make us turn to location adaptive dictionaries.

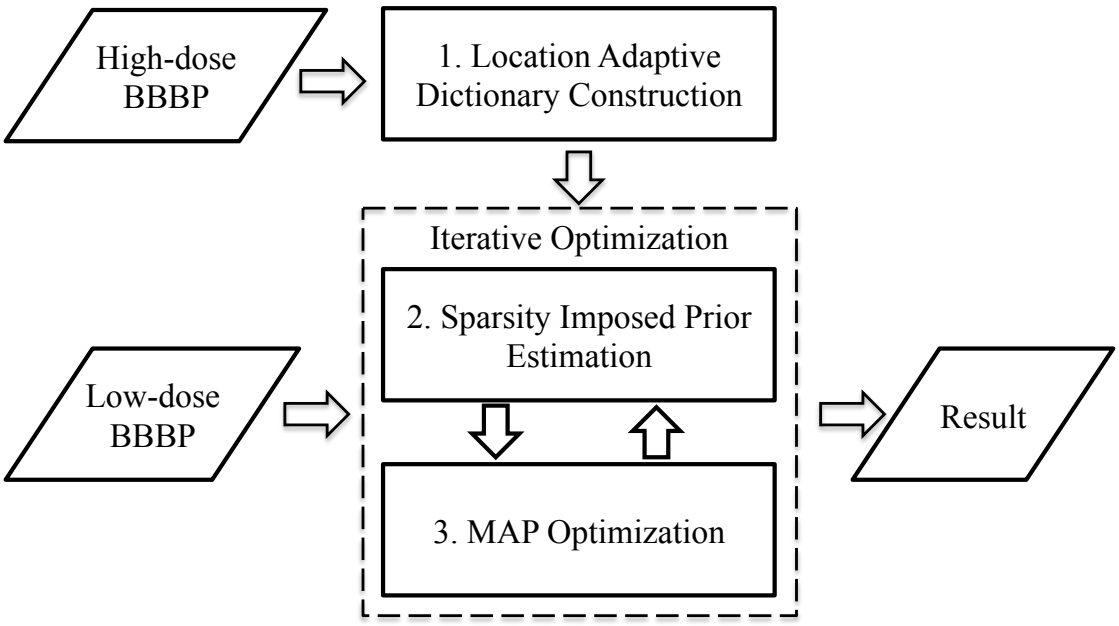

Figure 4.1: The flowchart of the low-dose map enhancement framework which consists of three modules: location adaptive dictionary construction, sparsity imposed prior estimation and MAP optimization. Using the high-dose repository, high-quality parameter maps are computed as training data from which we are able to construct location adaptive dictionaries. Then an iterative process consisting of prior estimation and MAP optimization is applied to enhance the low-dose map.

Assuming that the space of a low-dose BBBP map P has been divided into overlapping patches, we use p_i, a column vector to denote the intensity values of a patch at location i. The search for patches to be included in the location adaptive dictionary is based on a search-window S_i surrounding the location i in the high-dose maps. For each high-dose map H_j for training, we extract with respect to p_i a $L \times m$ dictionary matrix $D_j = [p_j^1, \ldots, p_j^m]$, where L is the length of p_i, and m is the number of patches to select from each high-dose map. The search process is repeated for all available high-dose maps j ($j = 1, \ldots, n$) to build the final $L \times M$ dictionary matrix $D = [D_1, \ldots, D_M]$, where $M = mn$. The location adaptive dictionary relaxes the need for accurate registration via its patch-based

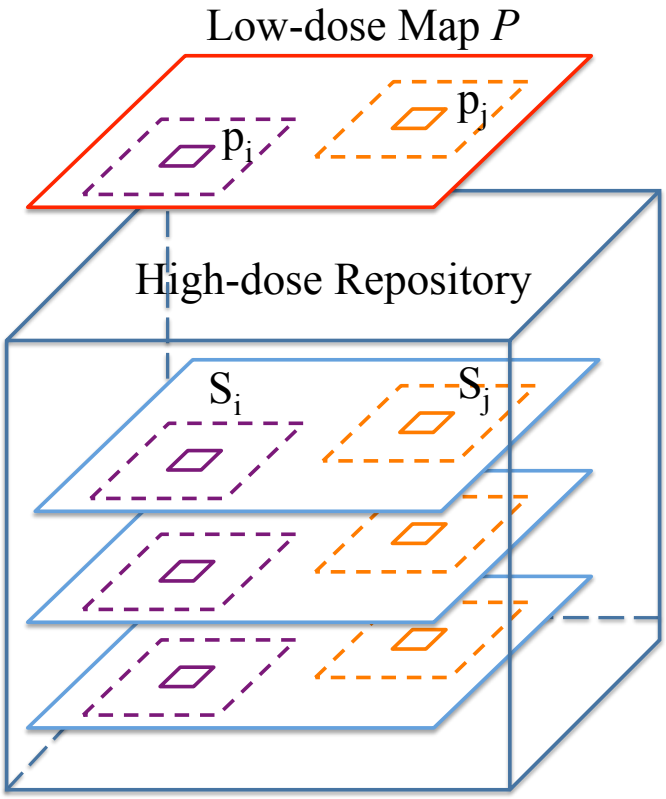

Figure 4.2: Construction of location adaptive dictionaries for a low-dose map P (red) from the high-dose repository (blue). Search bounding box is adaptively determined for each patch P (such as the purple box p_i or the orange box p_j) by using the location of the current patch as reference. After determining the bounding box (dashed line S_i and S_j) for the current patch, a certain number of patches across different training samples are selected into the dictionary D.

search mechanism, and saves the computational demand at restoration. The concept of the location adaptive dictionary is shown in Fig. 4.2.

4.4.3 Sparse high-dose induced prior

Without loss of generality, the BBBP measurement can be approximately expressed as a linear regression problem:

$$Y = CBV + X \otimes P \tag{4.7}$$

where P in $\mathbf{R}^{N\times 1}$ is the vector of BBBP values to be estimated by stacking the pixels in the 2-D map vertically. Y, X and CBV in $\mathbf{R}^{T\times N}$ are the dependent, the independent variables and the intercept derived from Eq. 4.5 for all pixels in P. The operator $\otimes$ indicates that the column i in X is multiplied by the i^{th} value in P. The goal of blood-brain barrier permeability computation is to estimate the parameter P according to the measurement model in Eq. 4.7.

Direct linear regression for each pixel independently may lead to unreliable outcome given the noisy sinogram data at low-dose PCT with various artifacts. To address this problem, we propose a penalized least square approach based on the MAP estimation criterion by adding a *priori* term $R(P)$ to the least square form of the problem:

$$P* = \arg\min_{P\geq 0} ||Y - V - X \otimes P||_2^2 + \beta R(P) \tag{4.8}$$

The priori term $R(P)$ plays an important role for reliable BBBP estimation in low-dose condition. Here based on the previous studies using sparse and redundant dictionaries for sinogram denoising in regular CT [89] and cerebral blood flow map enhancement [27] in perfusion CT, a sparse high-dose induced prior (named shd prior) is proposed:

$$R(P) = ||P - shd(P)||_2^2 \tag{4.9}$$

where $shd(P)$ represents a sparse high-dose induced reconstruction.

Upon obtaining the corresponding location adaptive dictionary D_i for patch p_i in the low-dose BBBP map P, the denoised version of p_i is assumed to be formulated as a linear combination of a few patches in the dictionary D_i as $p_i = D_i\alpha$, where α is a $M \times 1$ column weight vector to choose the appropriate dictionary atoms.

$$shd(p_i) = D_i \cdot \arg\min_{\alpha} \|p_i - D_i\alpha\|_2^2 \quad \text{subject to } \|\alpha\|_0 < K \tag{4.10}$$

where $\|\cdot\|_0$ represents the L_0 norm which constrains the number of atoms to combine the reconstructed patch to less than K.

The sparsity constraint in Eq. 4.10 is necessary in two ways. First the noise may be perfectly reconstructed if any combination can be used. Second, the solution to the problem may not be unique when the dictionary D is overcomplete ($M > L$). Sparsity constraint has been shown effective in various scenarios, including natural image denoising, image super-resolution, video denoising, MR reconstruction, etc. [20, 110, 85, 45], by imposing a regularization term that limits the number of examples to select from the training repository. Another important advantage of the sparse L_0-based constraint over the L_2-based constraint is that the L_0 constraint is less sensitive to the outliers, which in image processing applications indicates sharp edges.

The constraint in Eq. 4.10 is not directly tractable due to non-convexity of the L_0 norm. Greedy algorithms can be used to solve this NP-hard L_0 norm minimization problem. Yet there is no guarantee to find the global minima. Generally, no known algorithms can search for the sparsest solution more efficiently than exhausting all possible subsets of α. Fortunately, the recent development in the sparse representation theory [17] proves that L_1 norm can be applied to impose sparsity while making the problem convex. So Eq. 4.10 is relaxed to

$$shd(p_i) = D_i \cdot \underset{\alpha}{arg\,min}(\|p_i - D_i\alpha\|_2^2 + \lambda\|\alpha\|_1) \tag{4.11}$$

where $\|\alpha\|_1$ stands for the sum of the absolute values of the components of α.

The sparse high-dose induced prior of BBBP map P can thus be reconstructed by overlapping and averaging the reconstructed patches from Eq. 4.11. And the final cost function to optimize is

$$P^* = \underset{P\geq 0}{\arg\min}\|Y - CBV - X \otimes P\|_2^2 + \beta\|P - shd(P)\|_2^2 \tag{4.12}$$

The cost function composes of two terms: the temporal linear regression model from the Patlak assumption, and the spatial regularization term of sparse reconstruction induced from the high-dose maps. The interweaving of the temporal and spatial information can overcome the high noise sensitivity of the Patlak model with sole temporal term and pave the way for a robust model for low-dose BBBP estimation.

4.4.4 Problem reformulation

Given that the weight vector α in Eq. 4.11 is a function of the objective map P, solving the cost function in Eq. 4.12 is not straightforward. Therefore an iterative approach is adopted to optimize the cost function, which automatically adjust the weight vector α in Eq. 4.11 according to the current estimation P^t at t^{th} iteration and the location adaptive dictionaries during each iteration. To solve the objective function with the operator $\otimes$ in Eq. 4.12, we first reformulate it to conventional matrix multiplication. The Patlak model in Eq. 4.7 can be

expressed as

$$\bar{Y} = X \cdot diag(P) = \bar{X}P \tag{4.13}$$

where $\bar{Y}$ in $R^{TN\times 1}$ is formed by stacking the columns of $Y - CBV$ vertically. $\bar{X}$ is a $TN \times N$ matrix formed by positioning the columns of matrix X on the diagonal of the new matrix $\bar{X}$, so that

$$\bar{X} = \begin{pmatrix} X_{.,1} & 0 & \cdots & 0 \\ 0 & X_{.,2} & \cdots & 0 \\ \vdots & \vdots & \ddots & \vdots \\ 0 & 0 & \cdots & X_{.,N} \end{pmatrix} \tag{4.14}$$

Now the objective function in Eq. 4.12 becomes

$$P^* = \arg\min_{P\geq 0} ||\bar{Y} - \bar{X}P||_2^2 + \beta||P - shd(P)||_2^2 \tag{4.15}$$

4.4.5 MAP optimization framework

The shd-Patlak algorithm optimizes the estimated low-dose BBBP map by an EM style MAP algorithm, which iterates the following two steps:

1. *shd prior estimation.* Given the current map estimation P^t and the high-dose map repository, location adaptive dictionaries are built for each patch p_i^t in P^t. Eq. 4.11 can be solved by multiple algorithms and we use Lasso [96] in this work. The regularization term $R(P)$ is then obtained in Eq. 4.9.
2. *Steepest descent optimization.* The steepest descent optimization is applied to Eq. 4.15 to generate the new map estimation. We denote $\bar{X}' = \bar{X} + \beta I$ and

$\bar{Y}' = \bar{Y} + \beta shd(P)$. The updated estimation of BBBP map, i.e. P^{t+1}, can be expressed as:

$$P^{t+1} = P^t + \gamma^{t+1}(\bar{X}'^T(\bar{Y}' - \bar{X}'P)) \tag{4.16}$$

where γ^{t+1} indicates the gradient step-size which can be computed adaptively following the estimator [92]

$$\gamma^{t+1} = \frac{Q^T Q}{(\bar{X}'Q)^T(\bar{X}'Q)} \text{ where } Q \equiv \bar{X}'^T(\bar{X}'P^t - \bar{Y}') \tag{4.17}$$

The updated P^{t+1} is put back to step 1 again to obtain the new shd prior estimation.

The optimization framework of the algorithm is detailed in Algorithm 2. We observe that our results are quite stable with respect to the local random perturbations of the subject space (e.g. the initialization). This shows that slight differences of the initial estimation algorithm do not affect the final results.

4.5 Experiment setup

4.5.1 Data acquisition

To evaluate the performance of the proposed shd-Patlak algorithm on BBBP map computation in PCT, clinical brain PCT images were acquired with GE Pro-16 scanners (General Electric Medical Systems, Milwaukee, WI) located at NewYork-Presbyterian Hospital at Weill Cornell Medical College in New York City, NY. First, 45 mL of non-ionic iodinated contrast was administrated intravenously at 4.0 mL/s using a power injector. Then with a 5 s delay, the cine

Algorithm 2: The iterative optimization framework to solve Eq. 4.15

Input: Location adaptive dictionaries $D_{i\in I} \in \mathbf{R}^{L\times M}$ (I is the set of all possible patch locations), input low-dose BBBP map $P \in \mathbf{R}^N$. Independent and dependent parameters in Patlak model $\bar{X} \in \mathbf{R}^{TN\times N}$ and $\bar{Y} \in \mathbf{R}^{TN\times 1}$.

Output: Updated low-dose BBBP map $P^t \in \mathbf{R}^N$.

$R(P) = 0$.

repeat

for $i = 1, 2, \ldots, |I|$ **do**

Compute the sparsity-induced prior using Lasso

$$shd(p_i) = \arg\min_{p_i} ||p_i - D_i\alpha||_2^2 + \lambda||\alpha||_1 \tag{4.18}$$

end for

Update $shd(P^t)$ by overlapping and averaging patches $shd(p_i)$.

Update regularization prior $R(P^t) = ||P^t - shd(P^t)||_2^2$

Update P^t using steepest descent optimization

$$P^{t+1} = P^t + \gamma^{t+1}(\bar{X}'^T(\bar{Y}' - \bar{X}'P)) \tag{4.19}$$

where $\bar{X}' = \bar{X} + \beta I$, $\bar{Y}' = \bar{Y} + \beta shd(P)$, $\gamma^{t+1} = \frac{Q^T Q}{(\bar{X}'Q)^T(\bar{X}'Q)}$, $Q \equiv \bar{X}'^T(\bar{X}'P^t - \bar{Y}')$

until Stop criteria

(continuous) enhanced high-dose scan was performed at tube voltage of 80 kVp, tube current of 190 mA, 1 rotation per second for duration of 45 s. The scanning volume of 2.0 cm consists of 4 slices at 5.0 mm thickness with its inferior extent selected at the level of basal ganglia, above the orbits, to minimize radiation exposure to the lenses. The source-to-detector distance was 946 mm, and the

source-to-patient distance was 538 mm. CT dose index volume (CTDI-vol) was 725.21 mGy, and the dose-length product was 1450.42 mGy-cm.

4.5.2 Low-dose data simulation

Repetitive scanning of the same patient at different radiation doses is unethical. So instead of scanning the patients twice, researchers simulate low-dose CT images from the acquired high-dose data with noise models of varying complexity [6, 99, 112, 37, 40, 41, 72, 94]. Among these techniques, we use the approach described by [6], which demonstrated that low-dose scan can be simulated by adding spatially correlated statistical noise to the reconstructed CT images (before processing to generate perfusion maps), for its simplicity and effective low-dose simulation.

Quantum noise is linearly related to the square root of the absorbed dose in the detector. The absorbed dose is proportional to the tube current level multiplied by the X-ray exposure time, mAs. When the X-ray exposure time is fixed, the noise standard deviation σ and the tube current I (mA) has an inverse relationship as below:

$$\sigma = \frac{K}{\sqrt{I}} \tag{4.20}$$

Let's define I_0 as the original high-dose tube current level in mA, I the desired low-dose tube current level. σ_0 and σ are the corresponding standard deviation of the pixels in the reconstructed CT images at the above tube current levels. The distribution of the noise is independent, so the standard deviation

σ_G of the added Gaussian noise can be derived from

$$\sigma_G^2 = \sigma^2 - \sigma_0^2 = (I_0/I - 1)\sigma_0^2 = K^2(1/I - 1/I_0) \tag{4.21}$$

To generate the spatially correlated statistical noise, we first measure the spectral properties of CT noise from the phantom data and then calculate the noise power spectrum for each tube current setting. The shape of the normalized noise power spectra is stable at different mAs, so the same spectrum model is used for all cases and noise levels. Following the practice in [6], we generate the noise autocorrelation function (ACF) from these data and choose the 11×11 window around the autocorrelation peak as a convolution filter for producing colored noise in subsequent experiments.

The autocorrelation function is convolved with the white Gaussian noise to simulate noise with a proper power spectrum then the convolved noise is scaled to the desired standard deviation σ_G. The noise image is masked by a filter of valid pixels in the PCT data and is added to the same image. The noise spectrum of any simulated noise added to any image by this procedure is guaranteed to have the spectral properties observed in an actual CT scan of the phantom on this scanner.

In this study, the constant K in Eq. 4.20 is calibrated with 22 patients under I_0 = 190 mA and the average value of K is 103.09 $\text{mA}^{1/2}$. The reduced tube current I is chosen to represent the ultra-low dose at 15 mAs to match previously published techniques highlighting ultra-low exposure in lung CT perfusion examinations [111]. However it is important to note that the technique introduced in that work enhances the reconstructed CT images instead of the perfusion maps and is based on the nonlinear filtering of the difference image between the low-dose scan and the previous normal dose scan. This technique can be in-

corporated with our proposed spatio-temporal method to achieve further dose reduction and quality improvement.

4.5.3 Performance evaluation metrics

We adopted the following three metrics to evaluate the noise reduction for the quantitative comparison:

(1) Local signal to noise ratio (LSNR)

$$LSNR = \frac{\frac{1}{N}\sum_{i=1}^{N} P(i)}{\sqrt{\frac{1}{N}\sum_{i=1}^{N}(P(i) - \frac{1}{N}\sum_{i=1}^{N} P(i))^2}} \tag{4.22}$$

(2) Root-mean-square error (RMSE)

$$RMSE = \sqrt{\frac{1}{N}\sum_{i=1}^{N}[P(i) - P_{hd}(i)]^2} \tag{4.23}$$

where $P(i)$ is the permeability value at voxel i in the low-dose map, N is the total number of voxels in the region of interest (ROI). $P_{hd}(i)$ is the permeability value at voxel i in the corresponding high-dose map.

(3) Structural similarity index (SSIM) [100]

$$SSIM(x, y) = \frac{(2\mu_x\mu_y + C_1)(2\sigma_{xy} + C_2)}{(\mu_x^2 + \mu_y^2 + C_1)(\sigma_x^2 + \sigma_y^2 + C_2)} \tag{4.24}$$

where μ_x, μ_y are the expectation (mean) of image x and y, σ_x and σ_y are the unbiased standard deviation of image x and y. σ_{xy} is estimated as

$$\sigma_{xy} = \frac{1}{N-1}\sum_{i=1}^{N}(x_i - \mu_x)(y_i - \mu_y) \tag{4.25}$$

$C_1 = (K_1L)^2$, and $C_2 = (K_2L)^2$, where L is the dynamic range of the pixel values, and $K_1 = 0.01$, $K_2 = 0.03$ are used in this work.

4.5.4 Statistical analysis

The hypothesis for the quantitative evaluation of the BBBP maps was that each low-dose permeability maps enhanced using the proposed shd-Patlak model had no change in terms of above mentioned three metrics compared with the maps estimated by Patlak model, first across designated ROIs, and second over the whole brain region, while the maps estimated at high-dose 190 mA were regarded as golden standard for metric computation. The metric values were computed for each patient individually. Therefore, it was considered statistically appropriate to analyze these quantitative data by using the paired t-test. All P values were 2-sided, and $P < .05$ was considered statistically significant.

4.5.5 Implementation details

The implementation of the Patlak and shd-Patlak models was conducted on a MacBook Pro with 2.80 GHz Intel Core i7 processor with dual cores and 4 GB of RAM memory in MATLAB 2013a environment (The Math Works Inc., Natick, MA). BBBP maps using Patlak model on the high-dose 190 mA scan served as gold standard for the testing cases. A trained neuroradiologist (P.S.) with 12 years of experience reviewed permeability maps of all high-dose datasets and identified regions with visual perfusion deficits, defined as focal areas with elevated BBBP.

The training cases for location adaptive dictionary construction in Section 4.6 except Section 4.6.6 include the BBBP maps processed by Patlak model on the 190 mA scan of 10 cases (5 with brain deficits and 5 normal). For Section 4.6.6, 10 cases of pathological patients and 10 cases of healthy controls were used respec-

tively for two experimental settings. No additional smoothing was performed in BBBP map estimation.

The related parameters in the implementation were selected as follows:

(1) The size of the search-window S_i was 11×11. Since there was no registration performed, for the voxels on the boundary of the test image, the search space might consist of only background from the training data. Thus search window was moderately expanded based on the percentage of background voxels in the current patch on the boundary. (2) The patch size L was 5×5 with a overlap of 3. (3) The number of patches extracted from each training image m was 5. (4) The sparsity weight λ was 0.05. (5) The weighting parameter of high-dose induced prior β was 0.3. The choice of the parameters will be detailed in Section 4.6.7.

4.6 Results

4.6.1 Clinical BBBP maps

Fig. 4.3 shows the cerebral BBBP maps computed from the high-dose 190 mA and simulated low-dose PCT data at different exposure levels (mAs) (50 mA, 25 mA and 15 mA) using different computation methods. In the BBBP map computed by Patlak model from the simulated low-dose 15 mA and 30 mA PCT data, serious noise-induced artifacts can be observed, which obscure the permeability information. In the low-dose BBBP maps computed by shd-Patlak model, the clearly delineated signal with clear-cut edges in the shd-Patlak im-

ages are better reproduced than those from the Patlak model with independent computation of each voxel.

4.6.2 Vertical profiles

Fig. 4.4 depicts the vertical profiles of the BBBP maps shown in Fig. 4.3, where the profile from the high-dose map is regarded as a reference standard. The profiles from the shd-Patlak model matches better with that from the reference standard than the profile from the standard Patlak mode. In other words, the gains from the present shd-Patlak model are more noticeable than those from the Patlak model.

To quantitatively measure the consistency between the vertical profiles from the high-dose BBBP map and the vertical profiles from the simulated low-dose maps computed by the Patlak model and the shd-Patlak model, Table 4.1 lists the Lin's concordance correlation coefficients [59] of the two vertical profiles indicated by the white lines in Fig. 4.4. The results demonstrated that in profiles (a) and (b), Lin's concordance correlation coefficients from the low-dose Patlak maps are below 0.7 while the corresponding Lin's concordance correlation coefficient from the BBBP maps by the present shd-Patlak model is higher than 0.9, with all lower bounds of the 95% confidence interval of the concordance correlation coefficients higher than 0.9. In other words, the results may suggest a significant agreement between the profiles from the shd-Patlak maps and the high-dose maps.

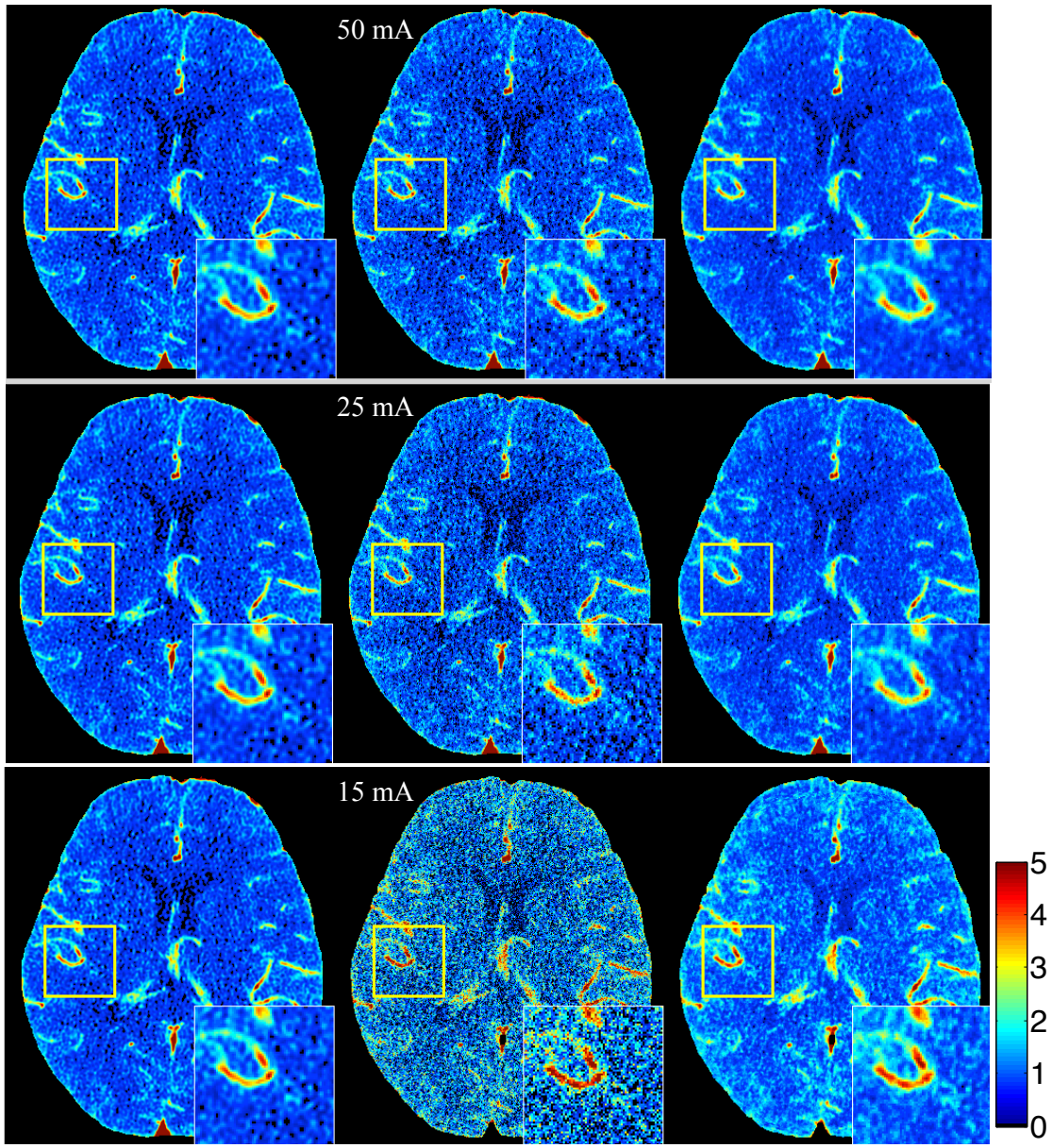

Figure 4.3: Cerebral BBBP maps computed by different methods from simulated low-dose PCT data at different exposure levels (mAs). The 1st column is the BBBP map estimated from high-dose 190 mA data (gold standard). The 2nd column is the BBBP maps estimated using Patlak model at simulated low-dose. Dose reduction, achieved through tube current reduction, primarily results in increased image noise, demonstrated as increased "graininess" in the map of the simulated low-dose scan. The 3rd column is the enhanced low-dose BBBP maps using shd-Patlak model. The 1st row is at tube current 50 mA (σ_G = 12.51), 2nd row at 25 mA (σ_G = 17.27), and 3rd row at 15 mA (σ_G = 25.54). The display window option: width is 5 HU, level is 2.5 HU. (Color)

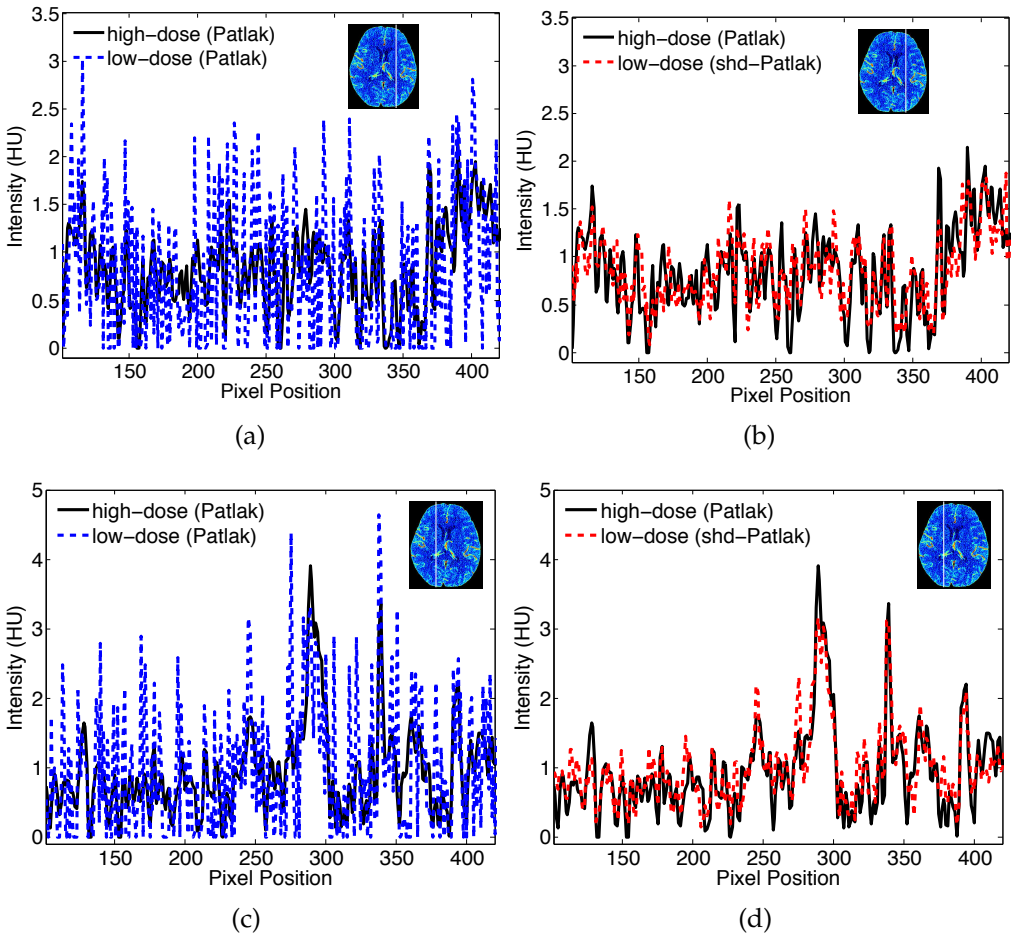

Figure 4.4: Vertical profiles of the BBBP map at high-dose and simulated at tube current of 15 mA in Fig. 4.3 at (a) x=320 using Patlak model, (b) x=320 using shd-Patlak model, (c) x=220 using Patlak model and (d) x=220 using shd-Patlak model. Profile between y=101 and 420 is shown and used for quantitative evaluation. The 'dash line' is from Patlak model or the shd-Patlak model. The 'solid line' is from the high-dose map which acts as the ground-truth for comparison.

Table 4.1: Lin's concordance correlation coefficient between the vertical profiles from the high-dose map and from the low-dose maps computed by the Patlak model and the shd-Patlak model.

Profile	Methods	Sample size	Lin's concordance correlation coefficient	95% confidence interval of concordance coefficient	P-value of significance level
a	Patlak	320	0.6810	(0.6791, 0.6829)	$P < 0.0001$
	shd-Patlak	320	0.9033	(0.9026, 0.9291)	$P < 0.0001$
b	Patlak	320	0.6846	(0.6826, 0.6865)	$P < 0.0001$
	shd-Patlak	320	0.9247	(0.9242, 0.9253)	$P < 0.0001$

4.6.3 Visual analysis

Fig. 4.5 shows the BBBP parameter maps calculated from the original high-dose images and the low-dose images computed by different methods from the noisy data, which is 15 mA, about one-twelfth radiation dose of the high-dose scan. The BBBP maps have a relatively small dynamic range compared to other hemodynamic parameter maps such as cerebral blood flow (CBF) and mean transit time (MTT), so that the errors in the low-dose maps are not as significant in its absolute value as those in other maps. We could still observe that the BBBP maps derived from the shd-Patlak model is similar to that derived from the original high-dose images. The shd-Patlak model can yield sharper edges and higher contrast between gray and white matter than the standard Patlak model. To further show the performance of the present shd-Patlak model, the zoomed

ROIs of the BBBP maps are shown in Fig. 4.6. The results clearly demonstrate that the shd-Patlak model has more gains than the standard Patlak model in preserving dynamic detail information (as indicated by the arrows in Fig. 4.6), which further indicates more reliable cerebral permeability parameter.

4.6.4 Quantitative analysis

Table 4.2 lists the LSNR, RMSE and SSIM metrics of three ROIs and the whole brain from the low-dose PCT by two different methods. The results from shd-Patlak model exhibits significant gains over the standard Patlak model in terms of the three metrics. On average, the shd-Patlak model performs better than Patlak model. On ROI1, the performance of shd-Patlak has 58.58%, 49.37% and 54.17% gain over Patlak model in terms of LSNR, RMSE and SSIM. Experimental results on other two ROIs and the whole brain also further demonstrate better performance of the present shd-Patlak approach. P-values from the paired t-test show that our proposed method shd-Patlak consistently and significantly improve the performance of permeability computation at low-dose in three different metrics.

4.6.5 Correlation analysis

To further demonstrate the merits of the present shd-Patlak model quantitatively, we manually select 20 specific ROIs of size 3×3 pixels from the second and third subjects in Fig. 4.5 which exclude the areas that contain major blood vessel branches and suspected abnormal signs. The ROIs are located at both

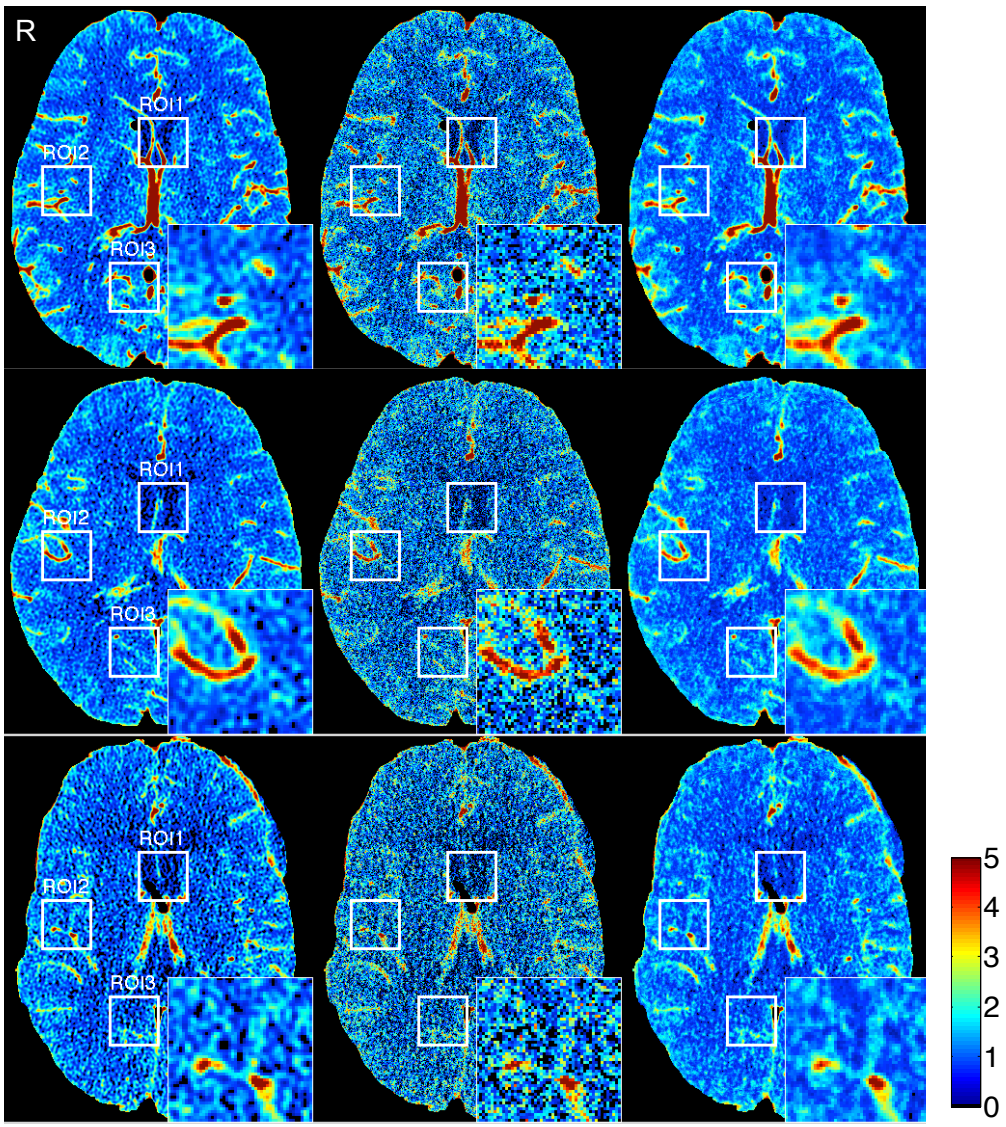

Figure 4.5: BBBP maps of 3 patients calculated from the different brain PCT images. Every row contains BBBP maps of one patient at different exposure and computation methods. The first column was calculated from the high-dose 190 mA images using Patlak model (the gold standard); the second and third columns were calculated from the simulated low-dose images by the Patlak model and the shd-Patlak model, respectively. The radiation dose in the low-dose data simulated is 15 mA, which equals to a 92% reduction of radiation exposure compared to the high-dose. Three ROIs of size 50×50 pixels are selected for all patients and quantitative evaluation is shown in Section 4.6.4. ROI2 is enlarged and displayed on the lower right corner of the maps. The first two patients are normal, while the third patient has brain deficit in the right middle cerebral artery (RMCA).

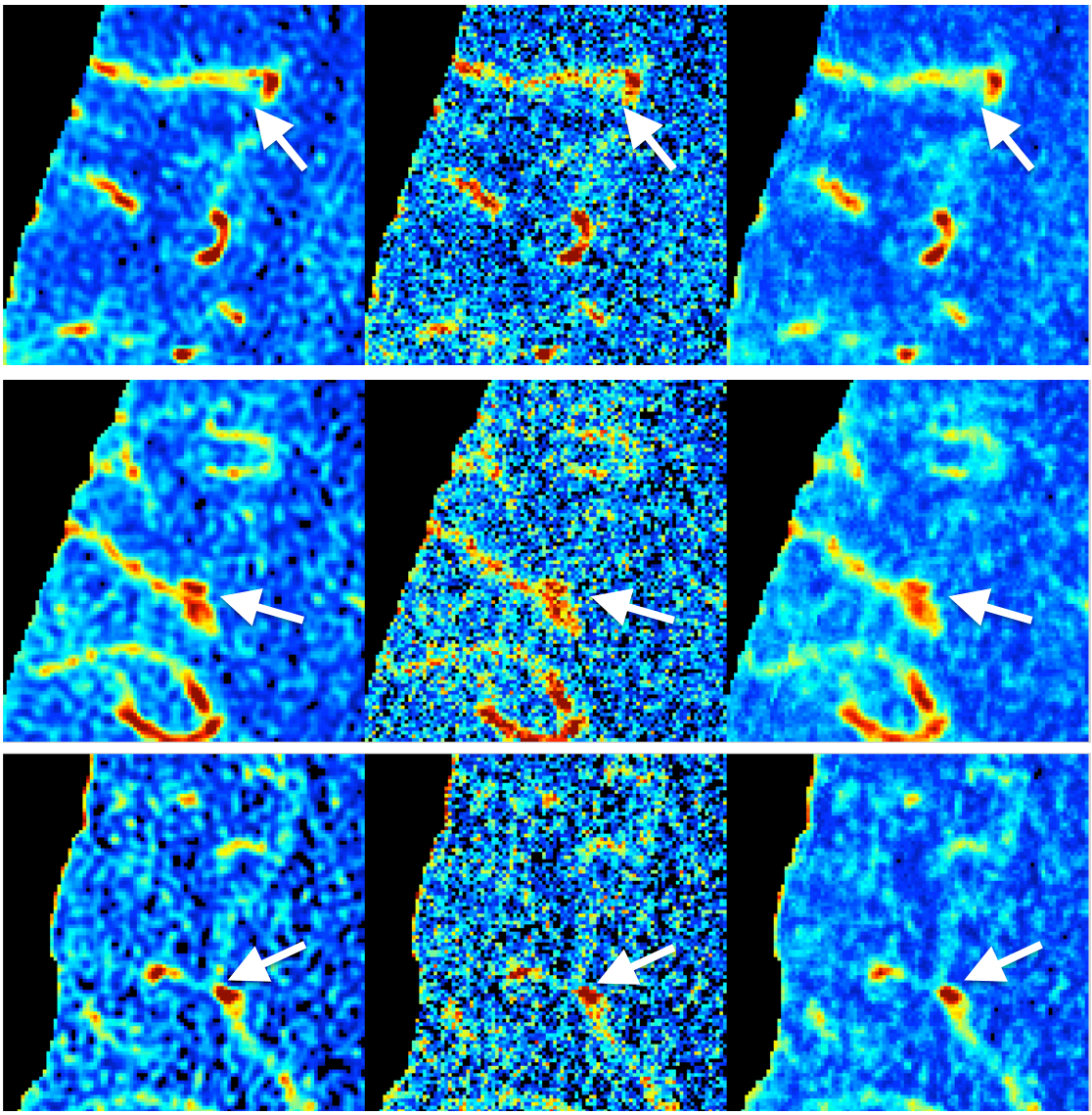

Figure 4.6: Zoomed regions of the BBBP maps shown in Fig. 4.5. The first column was calculated from the high-dose 190 mA images using Patlak model (the gold standard); the second and third columns were calculated from the simulated low-dose images by the Patlak model and the shd-Patlak model, respectively. The radiation dose in the low-dose data simulated is 15 mA, which equals to a 92% reduction of radiation exposure compared to the high-dose. The arrows highlight the tissue and blood vessels which are enhanced in the simulated low-dose maps.

hemispheres in basal ganglia, gray matter and white matter. Fig. 4.7 and 4.8 illustrate the regression equation, Pearson correlation coefficients and the corresponding Bland-Altman plots of BBBP values under different conditions for the these two patients in Fig. 4.5. It can be observed that the correlation coefficients derived from the high- and the low-dose maps computed by the shd-Patlak model are consistently higher than those from the low-dose maps of the Patlak model, whereas the difference in the ordinate axis on the Bland-Altman plot is smaller. For the BBBP parameters shown in Fig. 4.7 the bias from the shd-Patlak model is also less than that from the Patlak model. These figures suggest that the shd-Patlak model can achieve noticeable performance in low-dose PCT map estimation with the accuracy of diagnostic physiological parameters.

Table 4.2: Image quality metrics of 16 patients on the three ROIs indicated by the squares in Fig. 4.5. Each section divided by horizontal lines is for one patient. The first row in each section is the results of Patlak model, and the second row is the results of shd-Patlak model. The best performance in the average value for each metric and region is highlighted with bold font.

ID	ROI1			ROI2			ROI3		
	LSNR	RMSE	SSIM	LSNR	RMSE	SSIM	LSNR	RMSE	SSIM
1	0.93	0.73	0.47	1.20	0.83	0.46	1.13	0.83	0.46
	1.54	0.36	0.76	2.10	0.39	0.79	2.09	0.38	0.78
2	1.05	0.20	0.44	1.11	0.20	0.48	1.14	0.20	0.48
	1.62	0.09	0.74	1.59	0.10	0.76	1.64	0.10	0.74

Continued on next page

Table 4.2 – *Continued from previous page*

ID	ROI1			ROI2			ROI3		
	LSNR	RMSE	SSIM	LSNR	RMSE	SSIM	LSNR	RMSE	SSIM
3	0.73	0.62	0.74	1.15	0.67	0.67	0.82	0.69	0.72
	0.82	0.36	0.90	1.52	0.36	0.89	0.92	0.48	0.91
4	1.18	1.12	0.39	1.23	1.16	0.43	1.20	1.16	0.38
	2.50	0.53	0.68	1.86	0.47	0.76	1.89	0.53	0.68
5	1.04	0.86	0.43	1.18	0.92	0.45	1.27	0.94	0.52
	1.85	0.42	0.70	1.98	0.45	0.73	2.22	0.44	0.77
6	0.76	0.64	0.53	1.11	0.75	0.54	1.08	0.72	0.56
	0.95	0.35	0.74	1.73	0.39	0.77	1.60	0.39	0.76
7	0.87	0.61	0.44	1.15	0.75	0.50	1.19	0.73	0.44
	1.43	0.31	0.71	1.57	0.35	0.78	1.78	0.35	0.75
8	1.27	0.85	0.35	1.58	0.90	0.41	1.35	0.86	0.38
	2.22	0.38	0.68	2.49	0.38	0.75	2.55	0.38	0.69
9	0.86	0.72	0.41	1.43	0.91	0.49	1.14	0.85	0.46
	1.43	0.38	0.66	2.48	0.45	0.74	2.38	0.43	0.72
10	1.03	0.99	0.55	1.57	1.10	0.51	1.27	1.10	0.58
	1.23	0.61	0.76	2.61	0.54	0.76	1.54	0.58	0.79
11	0.84	0.85	0.59	1.09	0.97	0.60	0.94	0.88	0.65
	1.10	0.44	0.82	1.60	0.47	0.84	1.28	0.44	0.86
12	1.04	0.95	0.76	1.02	0.98	0.75	1.06	0.99	0.76
	1.31	0.48	0.92	1.39	0.53	0.91	1.29	0.55	0.91

Continued on next page

Table 4.2 – *Continued from previous page*

ID	ROI1			ROI2			ROI3		
	LSNR	RMSE	SSIM	LSNR	RMSE	SSIM	LSNR	RMSE	SSIM
13	0.88	0.80	0.37	1.39	0.96	0.45	1.03	0.87	0.46
	1.25	0.41	0.63	2.17	0.44	0.74	1.41	0.41	0.73
14	0.95	0.67	0.54	1.20	0.78	0.53	1.00	0.70	0.52
	1.44	0.36	0.77	1.91	0.40	0.79	1.48	0.38	0.77
15	1.22	1.13	0.44	1.50	1.23	0.44	1.30	1.22	0.50
	1.79	0.55	0.71	2.55	0.57	0.74	1.58	0.57	0.77
16	1.15	0.85	0.31	1.13	0.83	0.36	1.17	0.87	0.45
	2.45	0.41	0.62	2.70	0.40	0.63	1.78	0.42	0.72
Mean	0.99	0.79	0.48	1.25	0.87	0.50	1.13	0.85	0.52
	1.56	**0.40**	**0.74**	**2.01**	**0.42**	**0.77**	**1.72**	**0.43**	**0.77**
Std	0.16	0.22	0.13	0.18	0.24	0.10	0.14	0.23	0.11
	0.50	0.12	0.08	0.44	0.11	0.07	0.42	0.11	0.07
P	< 0.001	<0.001	<0.001	<0.001	<0.001	<0.001	<0.001	<0.001	<0.001

4.6.6 Evaluation of training data

To evaluate the impact of pathological and normal training data on the low-dose enhancement results, we choose 6 patients with brain deficits among the 16 patients and enhance them by training on only the healthy controls or the pathological cases. Each of the 6 low-dose testing cases has brain deficits due to subarachnoid aneurysmal hemorrhage (SAH) at one or more regions

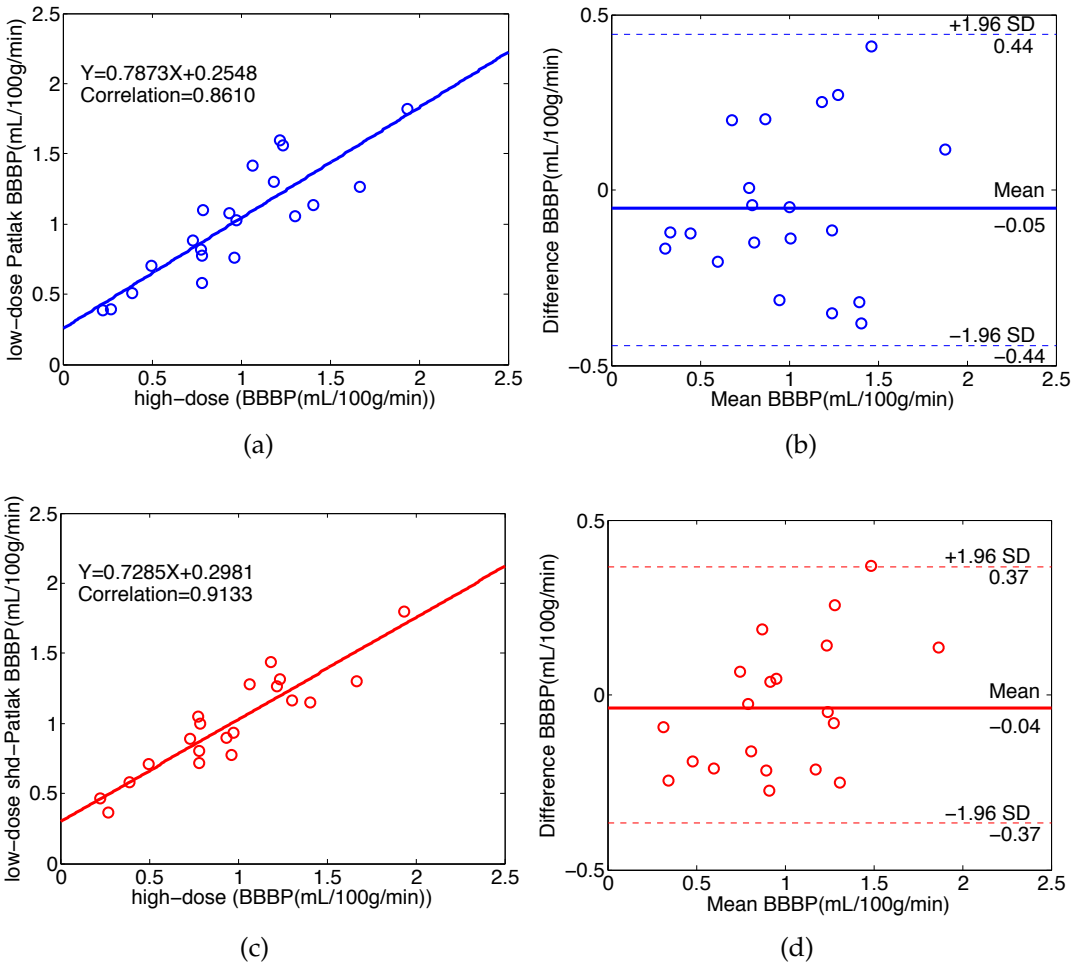

Figure 4.7: The correlation (left column) and Bland-Altman plot (right column) between the BBBP values computed from the high-dose images and the low-dose images by different methods for the patient in the second row in Fig. 4.5. Plots (a) and (b) represent the results obtained from the high- and low-dose by the Patlak model. Plots (c) and (d) represent the corresponding results obtained from the high- and low-dose by the shd-Patlak model.

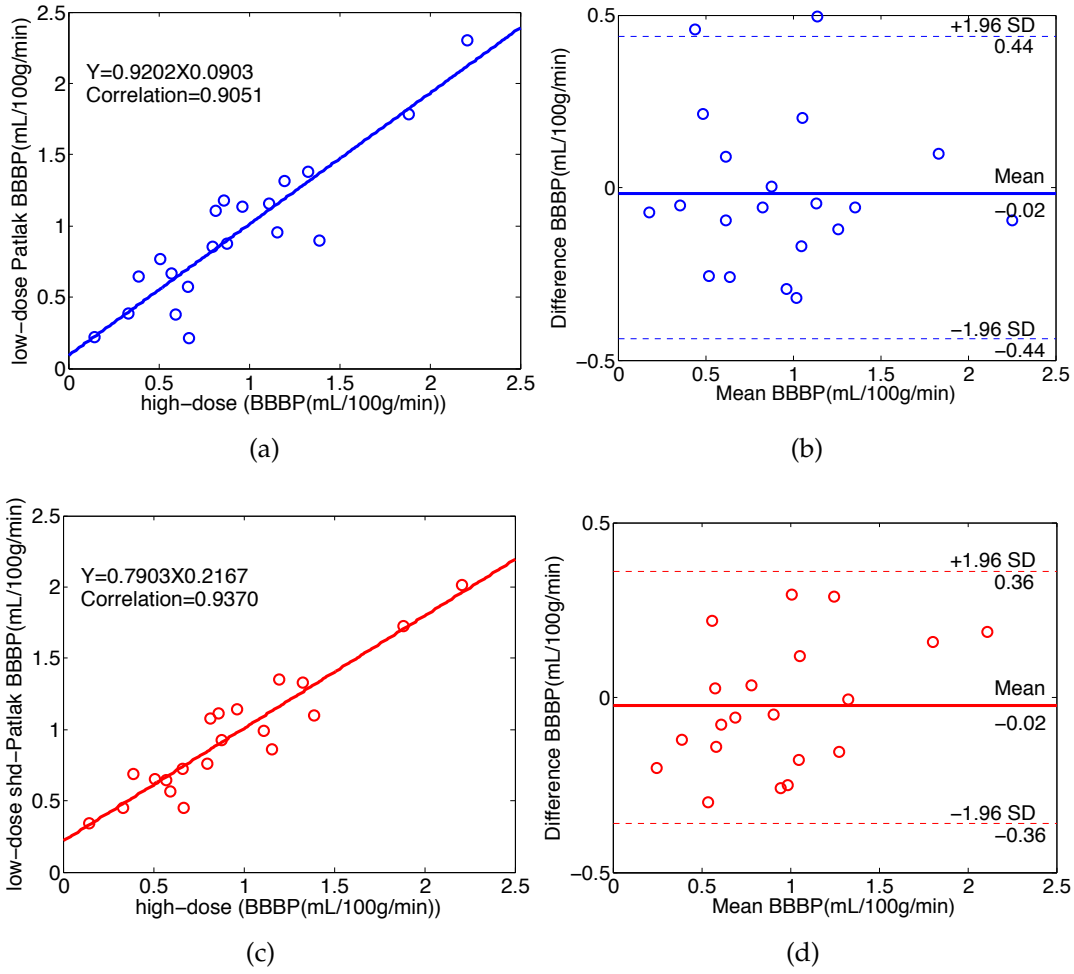

Figure 4.8: The correlation (left column) and Bland-Altman plot (right column) between the BBBP values computed from the high-dose images and the low-dose images by different methods for the patient in the third row in Fig. 4.5. Plots (a) and (b) represent the results obtained from the high- and low-dose by the Patlak model. Plots (c) and (d) represent the corresponding results obtained from the high- and low-dose by the shd-Patlak model.

from the following: right anterior cerebral artery (RACA), left anterior cerebral artery (LACA), right middle cerebral artery (RMCA), left middle cerebral artery (LMCA). The pathological training cases include deficits caused by SAH in all of the above mentioned regions. The healthy controls do not have any deficit in the BBBP maps. Fig. 4.9 shows the BBBP maps of Patient 8 at different experimental settings. Visual inspection indicates that while the BBBP maps estimated by both shd-Patlak models (either trained on cases with deficits or normal controls) outperform the maps generated by the standard Patlak model at low-dose 15 mA, there is no obvious visual differences between the maps estimated by the two shd-Patlak models. The abnormalities in the brain of the testing data are well preserved by using shd-Patlak model in both cases. Table lists the LSNR, RMSE and SSIM metrics of LMCA, RMCA and the whole brain region from the 6 pathological testing cases at low-dose exposure by three approaches: Patlak model, shd-Patlak trained on pathological and shd-Patlak trained on normal cases. Both shd-Patlak models significantly outperform the standard Patlak model in terms of three metrics on two regions and the whole brain area ($P1$ and $P2$). The hypothesis for $P3$ is that the permeability maps enhanced using the shd-Patlak model trained on healthy controls have no change in terms of three metrics compared with the maps enhanced by shd-Patlak trained on pathological cases. Paired t-test demonstrates that in terms of RMSE and SSIM, in general the two approaches are not statistically different. For LSNR, the two approaches are statistically different. Further one-tail t-test shows that shd-Patlak model trained on cases with deficits yields higher LSNR compared to that trained on normal controls for low-dose enhancement of pathological cases.

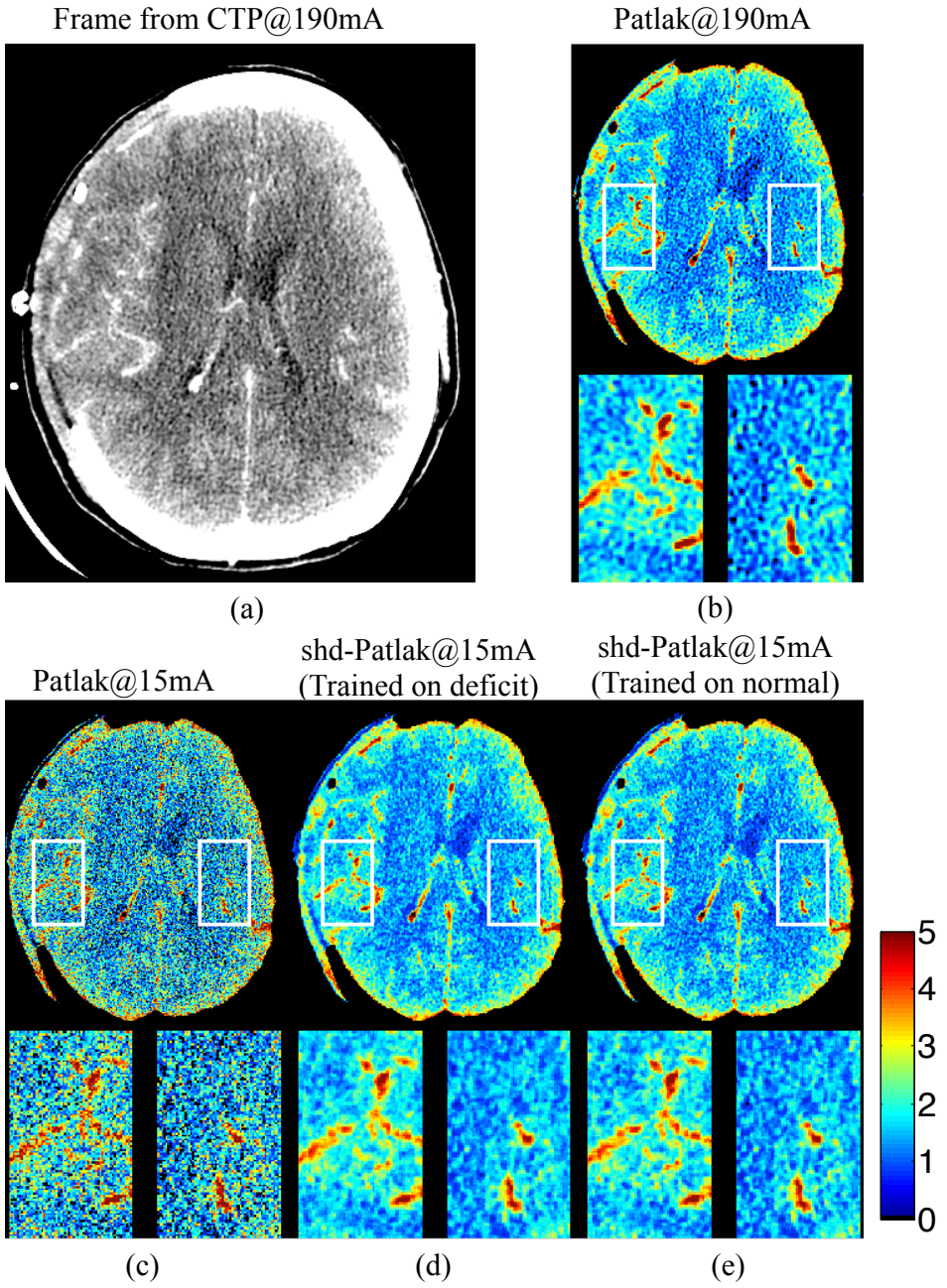

Figure 4.9: BBBP maps of Patient No. 8 at different experimental settings. (a) A frame from the PCT data of Patient 8, who has RACA deficit due to ventriculostomy catheter and the blood in the brain vessel flows into the skull. (b) Map calculated using Patlak model at 190 mA. (c) Map calculated using Patlak model at 15 mA. (d) Map calculated using shd-Patlak model at 15 mA and trained on deficit cases. (e) Map calculated using shd-Patlak model at 15 mA and trained on normal cases. Left and right middle cerebral arteries (LMCA and RMCA) are enlarged below the map.

Table 4.3: Image quality metrics of 6 patients with brain deficits on either RMCA or LMCA indicated by the rectangles in Fig. 4.9 and on the whole brain. Each section divided by a horizontal line is the metric values for one patient. The first row in each section is the results of Patlak model. The second row is of using shd-Patlak trained on deficit subjects. The third row is of using shd-Patlak trained on normal subjects. The best performance in the average value for each metric and region is highlighted with bold font. $P1$ is the p-value for comparison between Patlak and shd-Patlak trained on deficit cases. $P2$ is the p-value for the comparison between Patlak and shd-Patlak trained on normal cases. $P3$ is the p-value for the comparison between shd-Patlak model trained on the deficit cases and shd-Patlak trained on normal cases.

ID	RMCA			LMCA			Brain		
	LSNR	RMSE	SSIM	LSNR	RMSE	SSIM	LSNR	RMSE	SSIM
	1.21	0.20	0.52	1.18	0.20	0.51	0.88	0.17	0.58
2	1.63	0.10	0.79	1.68	0.10	0.78	1.11	0.09	0.82
	1.58	0.10	0.81	1.66	0.10	0.78	1.09	0.08	0.83
	1.27	1.16	0.40	1.30	1.18	0.38	0.87	0.97	0.52
4	2.03	0.51	0.71	2.32	0.52	0.71	1.17	0.44	0.77
	1.94	0.53	0.69	2.18	0.52	0.71	1.15	0.44	0.77

Continued on next page

Table 4.3 – *Continued from previous page*

ID	RMCA			LMCA			Brain		
	LSNR	RMSE	SSIM	LSNR	RMSE	SSIM	LSNR	RMSE	SSIM
	1.19	0.74	0.55	1.24	0.76	0.54	0.82	0.62	0.63
6	1.91	0.39	0.78	2.00	0.39	0.77	1.07	0.33	0.82
	1.88	0.40	0.78	1.84	0.38	0.79	1.05	0.33	0.83
	1.59	0.91	0.39	1.38	0.88	0.37	1.01	0.77	0.48
8	2.52	0.39	0.72	2.41	0.39	0.69	1.28	0.34	0.76
	2.43	0.40	0.72	2.29	0.40	0.69	1.27	0.35	0.75
	1.35	0.91	0.48	1.22	0.86	0.46	0.81	0.71	0.61
9	2.17	0.42	0.77	2.20	0.41	0.74	1.06	0.35	0.82
	2.02	0.42	0.78	2.07	0.41	0.76	1.04	0.35	0.83
	1.62	1.11	0.49	1.49	1.11	0.49	1.01	0.94	0.59
10	2.52	0.54	0.75	2.10	0.53	0.76	1.21	0.47	0.81
	2.49	0.55	0.74	2.07	0.55	0.75	1.20	0.48	0.80
	1.37	0.84	0.47	1.30	0.83	0.46	0.90	0.70	0.57
Mean	**2.13**	**0.39**	**0.75**	**2.12**	**0.37**	0.74	**1.15**	**0.34**	**0.80**
	2.06	0.40	**0.75**	2.02	0.39	**0.75**	1.13	**0.34**	**0.80**
	0.19	0.35	0.06	0.12	0.35	0.07	0.09	0.29	0.06
Std	0.35	0.16	0.03	0.26	0.16	0.04	0.09	0.13	0.03
	0.35	0.16	0.04	0.23	0.16	0.04	0.09	0.14	0.03
$P1$	<0.001	<0.01	<0.001	<0.001	<0.01	<0.001	<0.001	<0.01	<0.001
$P2$	<0.001	<0.01	<0.001	<0.001	<0.01	<0.001	<0.001	<0.01	<0.001
$P3$	0.01	0.04	1.00	0.01	0.47	0.36	<0.001	0.61	0.69

4.6.7 Evaluation of Convergence and Parameter Sensitivity

We also conducted experiments of the convergence rate and parameter sensitivity (Fig. 4.10). The cost function in Eq. 4.15 drops fast and usually converges after 2 or 3 iterations, as shown in Fig. 4.10(a). In our framework, five parameters should be selected manually, namely the patch-size L, the search-window S_i, the atom number m, the weighting parameters λ and β, which controls the sparsity the coefficient α and the importance of the regularization term. It is worthwhile to mention that all the related parameters are likely dependent on the application in practice. In general, the performance was stable for all parameters, and the optimum parameters were chosen for the above mentioned experiments. From Fig. 4.10(b), the optimal patch size of 5×5 was adequate for effective noise and artifact suppression while retaining computational efficiency. The search-window S_i should be sufficiently large to acquire more similarity information while minimizing the influence of the mismatched tissues. The size of the search window will also influence the searching time. To find sufficient similar patches in reasonable time, based on the analysis in Fig. 4.10(c), we chose a search window of 11×11. For the parameters λ and β, in this work, we briefly fixed the sizes of the search-window and patch-size, and compared the results estimated with a broad range of parameter values in term of visual inspection and quantitative measurements. The atom number from each training sample m depends on the size of the training dataset, and for the current experiment setting, $m = 5$ generated sufficient training patches. The sparse weight λ should not be too large, otherwise it will produce over-smoothed results and we found that $\lambda = 0.05$ generates satisfactory results for the cases in general. The weighting parameter β reflects the importance of the sparse high-dose induced prior and $\beta = 0.3$ was adequate for the reconstruction. More theoretical analysis in optimizing the

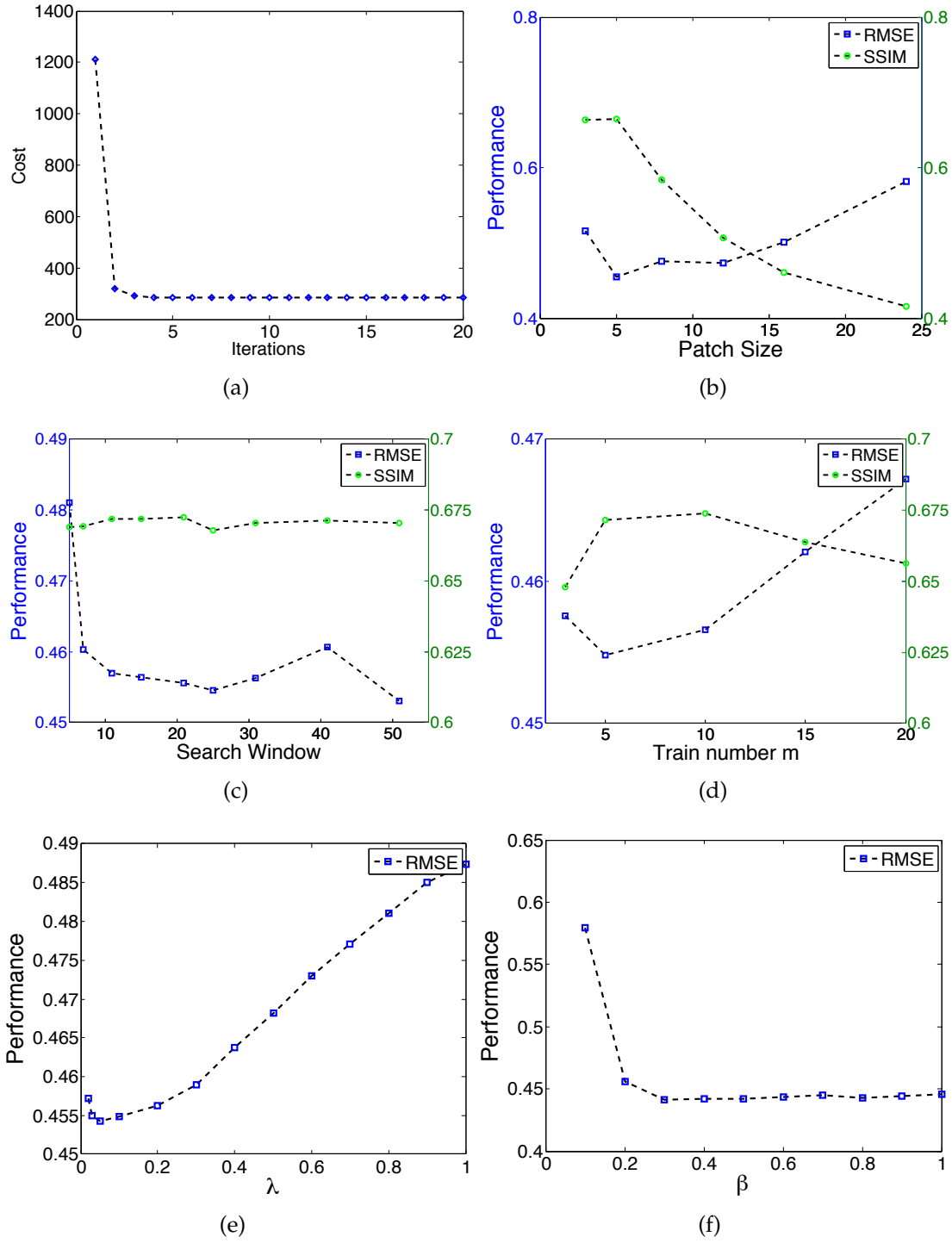

Figure 4.10: Convergence rate and parameter sensitivity of patch size, search window size, training samples per image, λ and β. A set of parameter values is tested. The cost function drops fast and usually converges after 2 or 3 iterations. Generally the performance is stable and the optimum values are chosen in the following experiments.

parameters are necessary, which may be a topic for future research.

4.7 Discussion

In this chapter, we present a high-dose induced prior for the low-dose blood-brain barrier permeability estimation in cerebral PCT. The experimental results show that the present shd-Patlak model can yield more significant performance gains than the existing Patlak model in terms of different measurement metrics and visual quality.

The penalty prior reflects the information of the desired BBBP map. The traditional image prior to tackle the inverse problems relies on some simplifying assumptions. These assumptions include local spatial smoothness, sparsity in the transformed domain and low/max-entropy, etc. In general, given that these assumptions are in accordance with the properties of the desired BBBP maps with a low noise level, these priors might work well. On the other hand, given that the noise level is relatively significant and the image information is deteriorated by the high noise level in the low-dose map, these priors would tend to produce the over-smoothed regions. More importantly, such condition is misleading in clinical scenarios because the related over-smoothed effect may average the neighboring pixels with the abnormal tissue and lead to neglect of the abnormality.

In PCT imaging, scans performed at higher tube current following the outdated and current protocols are available in the clinical data repository at hospitals. The high-dose high-quality BBBP maps provide strong a *priori* information of the general brain structure and permeability pattern. It would be a natural

choice to use the high-dose BBBP maps to induce low-dose BBBP map estimation from the measured noisy data. However, the patient distinction and the tissue deformation make such application challenging. Thus to fully use the high-dose permeability maps of different patients, dedicated image registration techniques are needed. Sparse high-dose induced prior may be a good candidate to use the high-dose maps for the current patient BBBP estimation because it does not heavily depend on the accuracy of the image registration due to its patch searching mechanism. Consequently, an important novelty of the present shd-Patlak model in this work is the utilization of the existent high-dose maps without the need of accurate image registration. In other words, the shd-Patlak model can relax the need for accurate image registration processing through its patch-based search mechanism during construction of the location adaptive dictionaries and selection of a sparse set of useful atoms from the dictionary during the reconstruction process.

The enhanced BBBP maps with abnormalities trained on healthy controls or the subjects with abnormalities are not statistically different in terms of RMSE and SSIM, while those trained on subjects with abnormalities have slightly higher LSNR. Visual inspection by neuroradiologists indicates that no significant difference can be found between the two cases and both of them significantly outperform the results using the standard Patlak model. Since RMSE and SSIM reflect the differences between the enhanced images and the gold standard, while LSNR is a metric that reflects the relationship of the signal value and the variance of the enhanced test image itself, the former two metrics reflect the fidelity between the enhanced low-dose image and the gold standard. When the patch size is sufficiently small (much smaller than the size of the abnormalities), the patches from the training data can represent the tissue structures at

the corresponding anatomical regions of the test data despite of the differences in subjects and types of deficits. Hence, an important advantage of the proposed shd-Patlak model is the independence between the abnormalities in the training and the testing data. In another word, the shd-Patlak model does not strictly require the same pathologies to be seen in the training data for reliable enhancement of the corresponding abnormalities in the testing cases.

Visual inspection on the enhanced low-dose BBBP maps by using shd-Patlak model shows minor loss of spatial resolution and color contrast. To address this, a neuroradiologist with 12 years of experience (P.C.S.) reviewed the simulated low-dose BBBP maps estimated using the standard Patlak model and shd-Patlak model in pairs while using the high-dose 190 mA BBBP maps as the reference. It shows that the minor loss of spatial resolution and color contrast in the BBBP maps of 16 cases did not significantly hamper the clinical diagnosis, while the severe noise (or "graininess") in the low-dose maps did hinder the accurate diagnosis of brain abnormality, especially at vessel boundaries and lobes. Further subjective evaluation by the neuroradiologists on clinical diagnosis could be a future research direction.

The EM-style algorithm converges fast, as shown in Fig. 4.10 (a) and usually converges in 2-3 iterations. Every step in the EM algorithm decreases or maintains the global energy without increasing it, leading to convergence in the end. Although there is no theoretical guarantee of the global optimum for this iterative algorithm, local random perturbations of the initialization yields stable optimization results. With good initialization using the BBBP map estimated using the standard Patlak model from the low-dose PCT data, the cost function generally converges to ideal solution. With proper parameter setting, the present

shd-Patlak model takes 40 s to process a PCT dataset of $512 \times 512 \times 119$ voxels, while the Patlak model takes 20 s in the same experimental setting. Considering the improved qualitative and quantitative results, the extended computation time is worthwhile. Obviously with faster computers, dedicated hardware and implementation of the algorithm in C++ environment would boost up the execution time and make the processing time clinically acceptable.

4.8 Conclusion

In this chapter, we propose an approach to restore the missing information in the low-dose BBBP maps generated from PCT with Patlak model. The standard Patlak model based PCT requires excessive radiation exposure, which raised attentions on the radiation safety. The proposed method constructs high quality BBBP maps from low-dose PCT by using the brain structural similarity between different individuals and the relations between high- and low-dose maps, leading to a reduction of 92% necessary radiation exposure.

The proposed approach first builds a high-dose induced prior for the Patlak model with a set of location adaptive dictionaries obtained from the corresponding anatomical regions in the high-dose maps from the repository, followed by an optimized estimation of BBBP map with the prior regularized Patlak model.

The shd-Patlak model was validated on a series of high-dose brain PCT datasets and the corresponding low-dose images simulated from the high-dose images. Evaluations were performed with visual inspection, profile comparison, three quantitative performance evaluation metrics and correlation analysis. The impact of abnormalities in the training data and parameter sensitivity were

also analyzed.

Currently our efforts were focused on the noise suppression in BBBP estimation using an iterative algorithm with a sparse high-dose induced prior. For future work, besides noise, bias and data corruption are also important problems in the low-dose PCT imaging which are worth future study. In clinics, the present algorithm can be applied to other spatial-temporal medical data and applications in which high-quality prior image is available and subsequent acquisition is performed, such as radiotherapy and magnetic resonance perfusion. Thus the present model can be adapted to the associated application for radiation dose reduction, opening another topic for future research.

CHAPTER 5

TREATMENT PLAN: TENSOR TOTAL VARIATION REGULARIZED DECONVOLUTION

Summary

Acute brain diseases such as acute stroke and transit ischemic attacks are the leading causes of mortality and morbidity worldwide, responsible for 9% of total death every year. 'Time is brain' is a widely accepted concept in acute cerebrovascular disease treatment. Efficient and accurate computational framework for hemodynamic parameters estimation can save critical time for thrombolytic therapy. Meanwhile the high level of accumulated radiation dosage due to continuous image acquisition in CT perfusion (CTP) raised concerns on patient safety and public health. However, low-radiation will lead to increased noise and artifacts which require more sophisticated and time-consuming algorithms for robust estimation. We propose a novel efficient framework using tensor total-variation (TTV) regularization to achieve both high efficiency and accuracy in deconvolution for low-dose CTP. The method reduces the necessary radiation dose to only 8% of the original level and outperforms the state-of-art algorithms with estimation error reduced by 40%. It also corrects over-estimation of cerebral blood flow (CBF) and under-estimation of mean transit time (MTT), at both normal and reduced sampling rate. An efficient computational algorithm is proposed to find the solution with fast convergence.

5.1 Introduction

Computed tomography perfusion (CTP) has important advantages in clinical practice due to its widespread availability, rapid acquisition time, high spatial resolution and few patient contraindications. Brain CTP has been proposed for improving the detection of ischemic stroke and evaluation of the extent and severity of hypoperfusion [55, 78]. Recently, the radiation exposure associated with CTP has raised significant public concerns regarding its potential biologic effects, including hair and skin damage, cataract formation and very small but finite cancer induction [102, 19]. Consensus has been reached that the "as low as reasonably achievable" (ALARA) principle should be executed more consistently. The low-dose protocols are unfortunately leading to higher image noise, which is compensated by using spatial smoothing, reduced matrix reconstruction and/or thick-slices, at the cost of lowering spatial resolution [56, 104].

Recent efforts have been focused on reducing radiation exposure from CTP while maintaining the spatial resolution and quantitative accuracy. Various algorithms have been proposed to reduce the noise in the reconstructed CT image series from the sinogram, including the low-pass filtering, edge-preserving filtering such as anisotropic diffusion [87], bilateral filtering [75], non-local means [66], total variation regularization [95], spatio-temporal filtering such as highly constrained back projection (HYPR) [93] and multi-band filtering (MBF). While edge-preserving filtering algorithms are relatively slow in computation, HYPR and MRF require motion-free images across the scan duration. Furthermore, these algorithms attempt to reduce the noise in the reconstructed CT image series, instead of improving the deconvolution algorithms or the quantification of perfusion maps. While improving the reconstructed CT images is an impor-

tant step towards robust and accurate hemodynamic parameter estimation, the deconvolution process itself to quantify the hemodynamic parameter maps is the essential procedure that generates the perfusion maps for disease diagnosis and treatment assessment. Perfusion parameter estimation via robust deconvolution is the task we are tackling in this work.

In this work, we propose a new robust deconvolution algorithm to improve the quantification of the perfusion parameter estimation at low dose by tensor total variation (TTV) regularized optimization. All the previously mentioned noise reduction algorithms for CT image series can complement our model to further reduce the noise and improve the image quality. Spatio-temporal regularization methods to stabilize the residue functions in the deconvolution process have been proposed, including weighted derivative [43], sparse residue representation [24] and sparse perfusion deconvolution using learned dictionaries [27, 26]. The deconvolution approach proposed in this work to accurately and robustly estimate the hemodynamic parameters is distinct from the previous work using edge-preserving total variation [95] for low-dose CT reconstruction. In [95], it focuses on the reconstruction procedure from sinogram to images using inverse Radon transform while our work addresses the deconvolution procedure from image sequences to perfusion maps based on Indicator dilution theory [74]. Besides this, both the data term and the regularization terms in our work have substantially different meanings from their definitions. For CT reconstruction, the data term is a projection process, while for deconvolution, it is a spatial-temporal convolution. The TV regularization term is a regularization on 2D CT images for CT reconstruction, while we extended it to 4D tensor regularization involving both the temporal and the spatial correlation information in the deconvolution. To our knowledge, this is the first research

proposing tensor total-variation to stabilize the deconvolution process.

The purpose of this original research is to develop and evaluate a tensor total variation (TTV) regularized deconvolution for low dose CTP data. The method is retrospectively evaluated in terms of image quality and signal characteristics of low dose brain CTP on both synthetic and clinical data.

The contribution of our work is three-fold. First, we propose to regularize the impulse residue functions instead of the perfusion parameter maps. Second, the optimization is performed globally on the entire spatio-temporal data, instead of each patch individually. Third, total variation regularizer is extended into the four dimensional sequence to consider the regional effect and temporal correlation of the tissue. The method reduces the necessary radiation dose to only 8% of the original level and outperforms the state-of-art algorithms with estimation error reduced by 40%. It also corrects over-estimation of cerebral blood flow (CBF) and under-estimation of mean transit time (MTT), at both normal and reduced sampling rate. An efficient computational algorithm is proposed to find the solution with fast convergence.

5.2 Materials and methods

5.2.1 Data acquisition and preprocessing

Clinical dataset

Retrospective review of consecutive CTP exams performed on aneurysmal subarachnoid hemorrhage patients enrolled in an IRB-approved and HIPAA-compliant clinical trial from August 2007-June 2014 was used. Ten consecutive patients (9 women, 1 men) admitted to the Weill Cornell Medical College, with mean age (range) of 54 (35-83) years were included. 5 patients (Patients 1-5) had brain deficits shown in the CTP images and the other 5 patients (Patients 6-10) had normal brain images. The brain deficits were caused by aneurysmal subarachnoid hemorrhage (SAH), which could lead to vasospasm, a serious complication of SAH, and may cause ischemic brain injury. CTP was performed with a standard protocol using GE Lightspeed Pro-16 scanners (General Electric Medical Systems, Milwaukee, WI) with cine 4i scanning mode and 45 second acquisition at 1 rotation per second using 80kVp and 190mA. Four 5-mm-thick sections were assessed at the level of the third ventricle and the basal ganglia. Approximately 45 mL of nonionic iodinated contrast was administered intravenously at 5 mL/s using a power injector with a 5 second delay. These acquired CTP data at high-dose were considered the reference standard for comparison to lower-dose CTP. For data analysis, vascular pixel elimination was applied by using a previously described method [57], in which the threshold for a vascular pixel was 1.5 times the average CBV of the unaffected hemisphere.

Low-dose simulation

To avoid the unethical repetitive scanning of the same patient at different radiation doses, we follow the practice in [6, 51] to simulate low-dose CT scan by adding spatially correlated statistical noise to the reconstructed CT images (before deconvolution). The tube current-exposure time product (mAs) varies linearly with the radiation dosage level. The dominant source of noise in CT imaging is quantum mottle and it is inversely proportional to the square root of mAs ($1/\sqrt{\text{mAs}}$).

The standard deviation of the added noise is computed by

$$\sigma_a = K \cdot (\frac{1}{I} - \frac{1}{I_0})^{\frac{1}{2}} \tag{5.1}$$

where I and I_0 are the tube current-exposure time product (mAs) at low-dose and normal dose. K is calibrated on 22 patients and the average value of $K = 103.09\text{mA}^{\frac{1}{2}}$. Gaussian noise is convolved with the noise autocorrelation function (ACF) generated from scanned low-dose phantom and scaled to the desired σ_a. For low-dose tube current of 30, 15 and 10 mAs gives the standard deviation $\sigma_a = 17.27, 25.54, 31.73$. The noise spectrum of any simulated noise added to any image by this procedure is guaranteed to have the spectral property observed in an actual CT scan of the phantom on the same scanner.

Synthetic dataset

Because the clinical CTP does not have ground truth perfusion parameter values for comparison, we first use synthetic data to evaluate the proposed algorithm. The arterial input function (AIF) is simulated using a gamma-variant function

[81] with the analytical form of:

$$c_{art}(t) = \begin{cases} 0 & \text{if } t \leq t_a \\ a(t - t_a)^b e^{-(t-t_a)/c} & \text{if } t > t_a \end{cases} \tag{5.2}$$

where t_a is bolus arrival time to any given region. Generally, $a = 1, b = 3, c = 1.5$ s, $t_a = 0$ are used to generate AIF typically obtained for a standard injection scheme. The transpose function $h(t)$ is

$$h(t; \alpha, \beta) = \frac{1}{\beta^\alpha \Gamma(\alpha)} t^{\alpha-1} e^{-t/\beta} \qquad \alpha, \beta > 0 \tag{5.3}$$

We set $\beta = MTT/\alpha$ to satisfy the central volume theorem [44]. Three types of experiments were performance on synthetic data: residue function recovery, uniform region estimation and contrast preserving.

5.2.2 Computation of perfusion parameters using deconvolution

For a volume under consideration v_{voi}, let c_{art} be the local contrast agent concentration at the artery inlet, and c_{voi} be the average contrast agent concentration in v_{voi}. ρ_{voi} is the mean density of the volume v_{voi}. The cerebral blood flow (CBF) is defined as the blood volume flow normalized by the mass of the volume v_{voi} and is typically measured in mL/100g/min. The cerebral blood volume (CBV) quantifies the blood volume normalized by the mass of v_{voi} and is typically measured in mL/100g. The mean transit time (MTT), usually measured in seconds, is defined as the first moment of the probability density function $h(t)$ of the transit times.

Furthermore, the (dimensionless) residue function $R(t)$ quantifies the relative amount of contrast agent that is still inside the volume v_{voi} of interest at time t after a contrast agent bolus has entered the volume at the arterial inlet at time $t = 0$, as

$$R(t) = \begin{cases} 1 - \int_0^t h(\tau)d\tau & \text{if } t \geq 0 \\ 0 & \text{if } t < 0 \end{cases} \tag{5.4}$$

Due to the various transit times within the capillary bed, the contrast will leave the volume gradually overtime. According to indicator-dilution theory,

$$\begin{aligned} c_{voi} &= CBF \cdot \rho_{voi} \cdot \int_{-\infty}^{\infty} c_{art}(\tau)R(t-\tau)d\tau \\ &= CBF \cdot \rho_{voi} \cdot (c_{art} \otimes R)(t) \end{aligned} \tag{5.5}$$

where $\otimes$ denotes the convolution operator. Here the variables $c_{voi}(t)$ and $c_{art}(t)$ can be measured and have known values, whereas the values of CBF, $R(t)$ and ρ_{voi} are unknown. To compute the perfusion parameters, an intermediate variable, the flow-scaled residue function $K(t)$ is introduced:

$$K(t) = CBF \cdot \rho_{voi} \cdot R(t) \tag{5.6}$$

which is given in units of $1/s$. The function $c_{art}(t)$ is usually replaced by a global arterial input function (AIF) measured in a larger feeding artery in order to achieve a reasonable signal-to-noise ratio (SNR). In brain perfusion imaging, the anterior cerebral artery is often selected. Thus, Eq. 5.4 can be rewritten as

$$c_{voi}(t) = (AIF \otimes K)(t) \tag{5.7}$$

Hence $K(t)$ can be computed from the measured data $AIF(t)$ and $c_{voi}(t)$ using

a deconvolution method, and the perfusion parameters may be determined as

$$\begin{aligned} CBF &= \frac{1}{\rho_{voi}} \cdot \max\left(K(t)\right) \\ MTT &= \frac{1}{\max\left(K(t)\right)} \cdot \int_0^\infty K(\tau)d\tau \\ CBV &= MTT \cdot CBF = \frac{1}{\rho_{voi}} \cdot \int_0^\infty K(\tau)d\tau \end{aligned} \tag{5.8}$$

Here using $\max\left(K(t)\right)$ instead of $K(0)$ has particular practical advantages due to bolus delay, defined as the delay time between the contrast arrival at tissue and the artery due to disease or other reasons.

In practice, AIF and $c_{voi}(t)$ are sampled at discrete time points, $t_i = (i-1) \cdot \Delta t$ with $i = 1, \ldots, T$ and typically $\Delta t = 1s$. Eq. 5.7 can be discretized as

$$\begin{aligned} c_{voi}(t_i) &= \int_0^\infty AIF(\tau)K(t-\tau)d\tau \\ &\approx \Delta t \sum_{j=1}^{T} AIF(t_j)K(t_{i-j+1}) \\ &= \Delta t \sum_{j=1}^{T} AIF(t_{i-j+1})K(t_j) \end{aligned} \tag{5.9}$$

In matrix-vector notation, we have

$$\begin{aligned} &\begin{pmatrix} c_{voi}(t_1) \\ c_{voi}(t_2) \\ \vdots \\ c_{voi}(t_T) \end{pmatrix} \\ = \Delta t &\begin{pmatrix} AIF(t_1) & 0 & \cdots & 0 \\ AIF(t_2) & AIF(t_1) & \cdots & 0 \\ \vdots & \vdots & \ddots & \vdots \\ AIF(t_T) & AIF(t_{T-1}) & \cdots & AIF(t_1) \end{pmatrix} \begin{pmatrix} K(t_1) \\ K(t_2) \\ \vdots \\ K(t_T) \end{pmatrix} \end{aligned} \tag{5.10}$$

Here we assume that the values of $AIF(t)$ can be neglected for $t > T$. The end of summation index can also be set to j instead of T since $K(t) = 0$ for $t < 0$. For a voxel of interest, Eq. 5.10 can be abbreviated as

$$c = Ak \tag{5.11}$$

where Δt and $AIF(t_j)$ are incorporated in the matrix $A \in \mathbb{R}^{T\times T}$, $c_{voi}(t_j)$ and $K(t_j)$ represent the entries in vectors $c \in \mathbb{R}^T$ and $k \in \mathbb{R}^T$. For a volume of interest with N voxels, we have

$$C = AK \tag{5.12}$$

where $C = [c_1, \ldots, c_N] \in \mathbb{R}^{T\times N}$, $K = [k_1, \ldots, k_N] \in \mathbb{R}^{T\times N}$ represent the contrast agent concentration and scaled residue function for the N voxels in the volume of interest.

In practice, the causality assumption in Eq. 5.10, i.e. the voxel signal cannot arrive before the AIF, may not hold. The AIF can lag $c_{voi}(t)$ by a time delay t_d in practice because the measured AIF is not necessarily the true AIF for that voxel, thus resulting in $AIF(t) = c_{art}(t - t_d)$. For instance, this lag can happen when the chosen AIF comes from a highly blocked vessel. Thus the calculated $R'(t)$ should be $R(t+t_d)$ to yield $c_{voi}(t)$ at the voxel. However the causuality assumption in Eq. 5.10 makes the estimation of $R'(t)$ improper. Circular deconvolution has been introduced to reduce the influence of bolus delay [108], where $R'(t)$ can be represented by time shifting $R(t)$ circularly by t_d.

Specifically, $c_{art}(t)$ and $c_{voi}(t)$ are zero-padded to length L, to avoid time aliasing in circular deconvolution, where $L \geq 2T$. We denote the zero-padded time series as $\bar{c}_{art} \in \mathbb{R}^{L\times 1}$ and $\bar{c}_{voi} \in \mathbb{R}^{L\times 1}$. Matrix A is replaced with its block-circulant version A_{circ}, with the elements $(a_{circ})_{i,j}$ of the block-circulant matrix $A_{circ} \in \mathbb{R}^{L\times L}$

defined as

$$(a_{circ})_{i,j} = \begin{cases} c_{art}(t_{i-j+1}), & \text{for } j \leq i \\ c_{art}(t_{L+i-j+1}), & \text{for } j > i \end{cases} \tag{5.13}$$

As an example, for $L = 2T$, the matrix A_{circ} has the following structure:

$$A_{circ} = \Delta t \left(\begin{array}{cccc|cccc} c_{art}(t_1) & 0 & \cdots & 0 & 0 & c_{art}(t_N) & \cdots & c_{art}(t_2) \\ c_{art}(t_2) & c_{art}(t_1) & \cdots & 0 & 0 & 0 & \cdots & c_{art}(t_3) \\ \vdots & \vdots & \ddots & \vdots & \vdots & \vdots & \ddots & \vdots \\ c_{art}(t_N) & c_{art}(t_{N-1}) & \cdots & c_{art}(t_1) & 0 & 0 & \cdots & 0 \\ \hline 0 & c_{art}(t_N) & \cdots & c_{art}(t_2) & c_{art}(t_1) & 0 & \cdots & 0 \\ 0 & 0 & \cdots & c_{art}(t_3) & c_{art}(t_2) & c_{art}(t_1) & \cdots & 0 \\ \vdots & \vdots & \ddots & \vdots & \vdots & \vdots & \ddots & \vdots \\ 0 & 0 & \cdots & 0 & c_{art}(t_N) & c_{art}(t_{N-1}) & \cdots & c_{art}(t_1) \end{array}\right) \tag{5.14}$$

Thus Eq. 5.11 can be replaced by

$$\bar{c} = A_{circ}\bar{k} \tag{5.15}$$

and Eq. 5.12 can be replaced by

$$\bar{C} = A_{circ}\bar{K} \tag{5.16}$$

where $\bar{c} \in \mathbb{R}^{L\times 1}$ and $\bar{k} \in \mathbb{R}^{L\times 1}$ are the zero-padded time series of c and k, and $\bar{C} \in \mathbb{R}^{L\times N}$ and $\bar{K} \in \mathbb{R}^{L\times N}$ are the zero-padded time series of C and K. For simplicity, we use C, A and K to represent the block-circulant version in Eq. 5.16 in the rest of the chapter.

5.2.3 Tensor total variation regularized deconvolution

The least square solution of Eq. 5.12 is equivalent to minimizing the squared Euclidean residual norm of the linear system given by Eq. 5.12 as

$$K_{ls} = \underset{K \in \mathbb{R}^{T \times N}}{\arg\min}(||AK - C||_2^2) \tag{5.17}$$

However, for the ill-conditioned Toeplitz matrix A, the least-square solution K_{ls} does not represent a suitable solution. A small change in C (e.g. due to projection noise or low-dose scan) can cause a large change in K_{ls}. Regularization is necessary to avoid the strong oscillation in the solution due to small singular values of matrix A.

Our assumption is that since the voxel dimensions in a typical CTP image are much smaller than tissue structures and changes in perfusion are regional effects rather than single voxel effects, within extended voxel neighborhoods the perfusion parameters will be constant or of low-variation, while it is also important to identify edges between different regions where tissues undergo perfusion changes, particularly ischemic regions.

We introduce the tensor total variation regularizer to the data fidelity term in Eq. 5.17 as

$$K_{ttv} = \underset{K \in \mathbb{R}^{T \times N}}{\arg\min}(\frac{1}{2}||AK - C||_2^2 + ||K||_{TV}) \tag{5.18}$$

It is based on the assumption that the piecewise smooth residue functions in CTP should have small total variation. The tensor total variation term is defined

as

$$\begin{aligned} \|K\|_{TV}^{\gamma} = \sum_{t,i,j,k} \Big[& \gamma_t |\tilde{K}_{t+1,i,j,k} - \tilde{K}_{t,i,j,k}| \\ & + \gamma_x |\tilde{K}_{t,i+1,j,k} - \tilde{K}_{t,i,j,k}| \\ & + \gamma_y |\tilde{K}_{t,i,j+1,k} - \tilde{K}_{t,i,j,k}| \\ & + \gamma_z |\tilde{K}_{t,i,j,k+1} - \tilde{K}_{t,i,j,k}| \Big] \end{aligned} \tag{5.19}$$

where $\tilde{K} \in \mathbb{R}^{T \times N_1 \times N_2 \times N_3}$ is the 4-D volume obtained by reshaping matrix K based on the spatial and temporal dimension sizes. Here $N = N_1 \times N_2 \times N_3$ and T is the time duration. The tensor total variation term here uses the forward finite difference operator using L_1 norm. The regularization parameter $\gamma_i, i = t, x, y, z$ controls the regularization strength for the temporal and spatial dimension. The larger the γ_i, the more smoothing the TV term imposes on the residue function in i^{th} dimension.

Since the TV term is non-smooth, this problem is difficult to solve. The conjugate gradient (CG) and PDE methods could be used to attack it, but they are very slow and impractical for real CTP images. Motivated by the effective acceleration scheme in Fast Iterative Shrinkage-Thresholding Algorithm (FISTA) [4], we propose an algorithm to efficiently solve the problem in Eq. 5.18 based on the framework of [45]

The proposed scheme include the following well-known important algorithms:

FISTA: FISTA considers minimizing the following problem:

$$\min f(x) + g(x), x \in \mathbb{R}^p \tag{5.20}$$

where f is a smooth convex function with Lipschitz constant L_f and g is a convex

function which may be non-smooth. An accelerated scheme is conceived in FISTA to obtain ϵ-optimal solution in $O(\frac{1}{\sqrt{\epsilon}})$ iterations.

Steepest gradient descent: To find a local minimum of a function, steepest gradient descent takes steps proportional to the negative of the gradient of the function at the current point. An adaptive step size s [92] is used due to the ill-conditioned matrix A makes the solution sensitive to noise in the observation C.

The proximal map: Given a continuous convex function $g(x)$ and any scalar $\rho > 0$, the proximal map associated to function g is defined as follows [4]

$$\text{prox}_{\rho}(g)(x) := \arg\min_{u}\left\{ g(u) + \frac{1}{2\rho}\|u - x\|^2 \right\} \tag{5.21}$$

For the proximal map, we extended the 2-dimensional TV regularizer in [4] to 4-dimensional and adapted the algorithm to tensor total variation regularization. The entire algorithm is shown in Algorithm 3.

5.2.4 Implementation details

All algorithms were implemented using MATLAB 2013a (MathWorks Inc, Natick, MA) on a MacBook Pro with Intel Core i7 2.8G Hz Duo CPU and 8GB RAM. Four baseline methods were compared: standard truncated singular value decomposition (sSVD) [81], block-circulant truncated SVD (bSVD) [108], Tikhonov regularization [34] and sparse perfusion deconvolution (SPD)[27]. A threshold value λ is empirically chosen as 0.1 (10% of the maximum singular value) to yield optimal performance for SVD-based algorithms. One-tail student test is used to determine whether there is significant difference between the evaluation

Algorithm 3: The framework of TTV algorithm.

Input: Regularization parameters γ_i, $i = t, x, y, z$

Output: Flow-scaled residue functions $K \in \mathbb{R}^{T \times N_1 \times N_2 \times N_3}$.

$K^0 = 0$

$t^1 = r^1 = K^0$

for $n = 1, 2, \ldots, N$ **do**

(1) Steepest gradient descent

$$K_g = r^n + s^{n+1}(A^T(C - Ar^n))$$

where $s^{n+1} = \frac{Q^T Q}{(AQ^T)(AQ)}$, $Q \equiv A^T(Ar^n - C)$

(2) Proximal map:

$$K^n = \text{prox}_\gamma(2\|K\|_{TV})(K_g)$$

where $\text{prox}_\rho(g)(x) := \arg\min_u \left\{ g(u) + \frac{1}{2\rho}\|u - x\|^2 \right\}$

(3) Update t, r

$$t^{n+1} = (1 + \sqrt{1 + 4(t^n)^2})/2$$

$$r^{n+1} = K^n + ((t^n - 1)/t^{n+1})(K^n - K^{n-1})$$

end for

metrics of the comparing algorithms. A α level of .05 is used for all statistical tests to indicate significance.

5.2.5 Evaluation metrics

Three metrics were used to evaluate the image fidelity to the reference: Root mean-squared-error (RMSE), Lin's Concordance Correlation Coefficient (CCC) and linear regression. RMSE evaluates the variability of the estimated low-dose maps compared to the reference. A value close to 0 indicates a smaller difference of data compared to the reference. Lin's CCC measures how well a new set of observations reproduce an original set, or the degree to which pairs of observations fall on the 45 line through the origin. Values of ±1 denote perfect concordance and discordance; a value of zero denotes its complete absence. Peak signal-to-noise ratio (PSNR) is also used to describe the noise level. In clinical CTP data, the maximum value in CT data is around 2600 HU, and simulated low-dose of 15 mAs yields $\sigma_a = 25.54$, which gives PSNR=40. In the synthetic evaluations, we conducted experiments at much lower PSNRs to highlight the differences between algorithms at even lower radiation.

5.3 Results

5.3.1 Synthetic evaluation

Because the clinical CTP does not have ground truth perfusion parameter values for comparison, we first use synthetic data to evaluate the proposed algorithm.

The simulated noise power spectrum (NPS) at 15 mAs is compared with the NPS of the real scanned phantom image at 15 mA, as shown in Figure 5.1 (a). In the experiments, three baseline methods were compared: sSVD, bSVD, Tikhonov and SPD regularizations.The first three methods are the most widely used regularized deconvolution methods for CTP, and widely adopted by commercial medical software [58]. SPD is the state-of-art algorithm for low-dose CTP deconvolution.

Residue function recovery

1) **Normal arterial input function**: The residue function recovered by the baseline methods and TTV are shown in Figure 5.1(b-f). The baseline methods show severe oscillation and elevated peak value, while the residue function recovered by TTV is in agreement with the reference.

2) **Tracer delay in arterial input function**: Circular deconvolution has been used to correct the delay effect using circular representation of AIF and c_{voi}, but with limited improvement, as shown in Fig. 5.2. The arterial input function is delayed by 5 s. bSVD and TTV use the block-circulant version of AIF and c_{voi}, while sSVD and Tikhonov use linear deconvolution. Though bSVD using block-circulant representation show relatively improved performance compared to sSVD, the estimated CBF (the maximum value of residue function) is still over-estimated around 30 mL/100g/min, while TTV with tensor total variation regularization in both temporal and spatial dimension could well correct the delay effect and output accurate residue function.

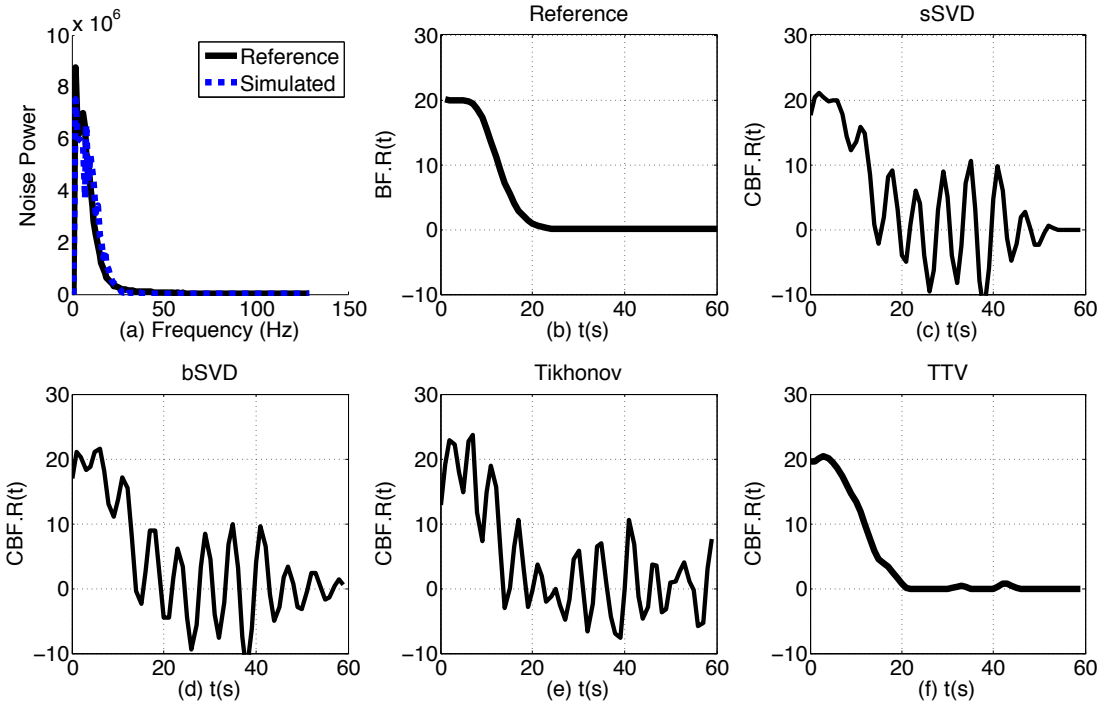

Figure 5.1: The Noise power spectrum and the recovered residue functions by baseline methods and TTV. (a) The noise power spectrum is of the scanned phantom image at 15 mAs and simulated statistical correlated Gaussian noise at 15 mA. (b)-(f) The parameters used for residue function recovery are the simulation is CBV = 4 mL/100 g, CBF = 20 mL/100 g/min, PSNR=25. SPD is not included since it optimizes the perfusion maps directly.

Uniform region estimation

From the recovered residue function, perfusion parameters CBF, CBV and MTT can be estimated using Eq. 5.8. We generate a small region containing 40 $\times$ 40 voxels with the same perfusion characteristics, and compute the mean and standard deviation of the perfusion parameters over this region.

1) Fig. 5.3 (a)-(b) show the estimated CBF and MTT values when the true perfusion parameter values vary. All the baseline methods overestimate the

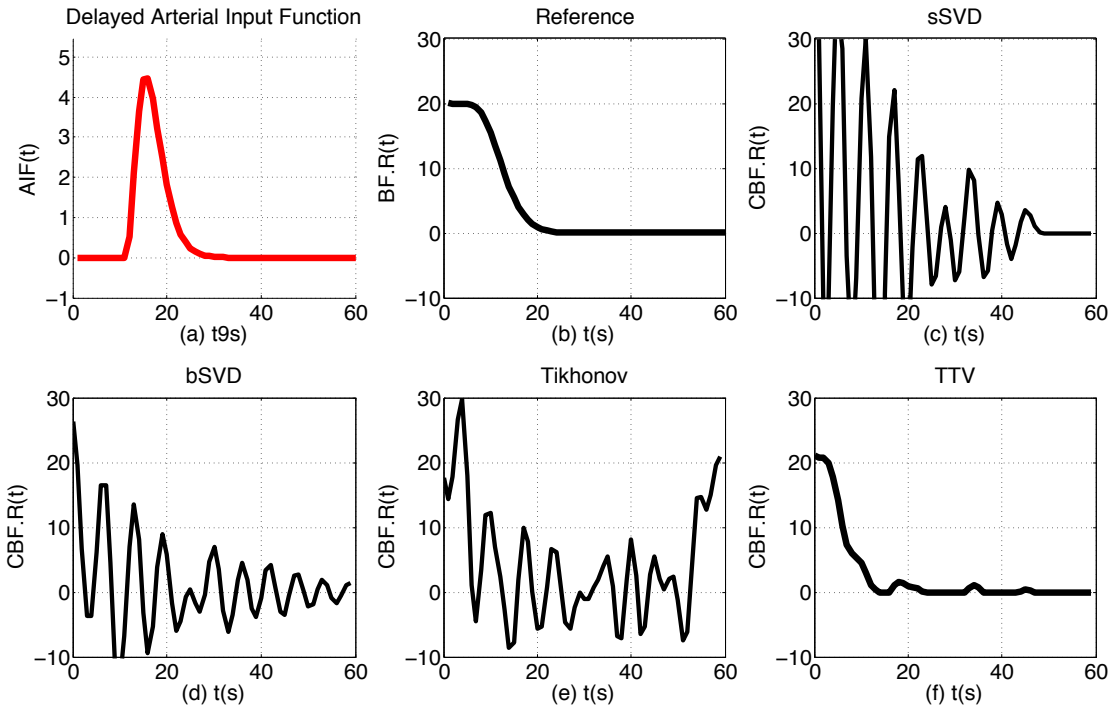

Figure 5.2: The delayed arterial input function and the recovered residue functions by baseline methods and TTV. (a) The delayed arterial input function with 5 s delay compared to tracer arrival at the tissue. (b)-(f) The parameters used for residue function recovery are the simulation is CBV = 4 mL/100 g, CBF = 20 mL/100 g/min, PSNR=25. SPD is not included since it optimizes the perfusion maps directly.

CBF values and under-estimate the MTT values while TTV yields accurate CBF and MTT estimations.

2) To explore the effect of noise levels on the performance of perfusion parameter estimation, we simulate different levels of noise (PSNR varies from 5 to 60) and fix CBF at 30 mL/100 g/min or MTT at 12 s. Fig. 5.3 (c)-(d) show the estimation results. TTV consistently generates more accurate estimation of CBF than the baseline methods across a broad rage of noise levels. Moreover, while the accuracy of the baseline methods degrades dramatically as the noise level

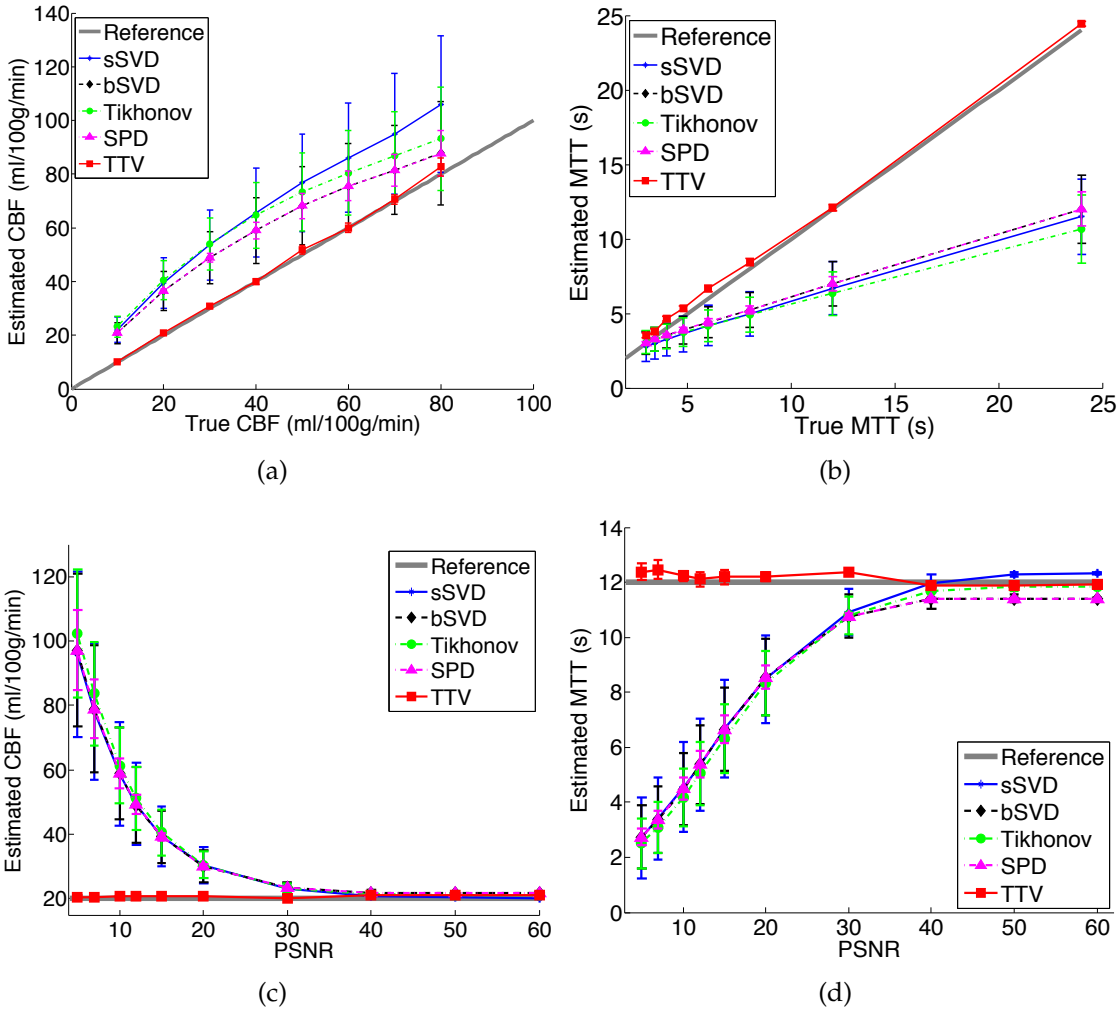

Figure 5.3: Comparison of the accuracy in estimating CBF and MTT by sSVD, bSVD, Tikhonov and TTV deconvolution methods. True CBV = 4 mL/100 g. The error bar denotes the standard deviation. (a) Estimated CBF values at different true with PSNR=15. (b) Estimated MTT values at different true MTT with PNSR=15. (c) Estimated CBF values at different PSNRs with true CBF=20 mL/100 g/min. (d) Estimated MTT values at different PSNRs with true MTT = 12 s.

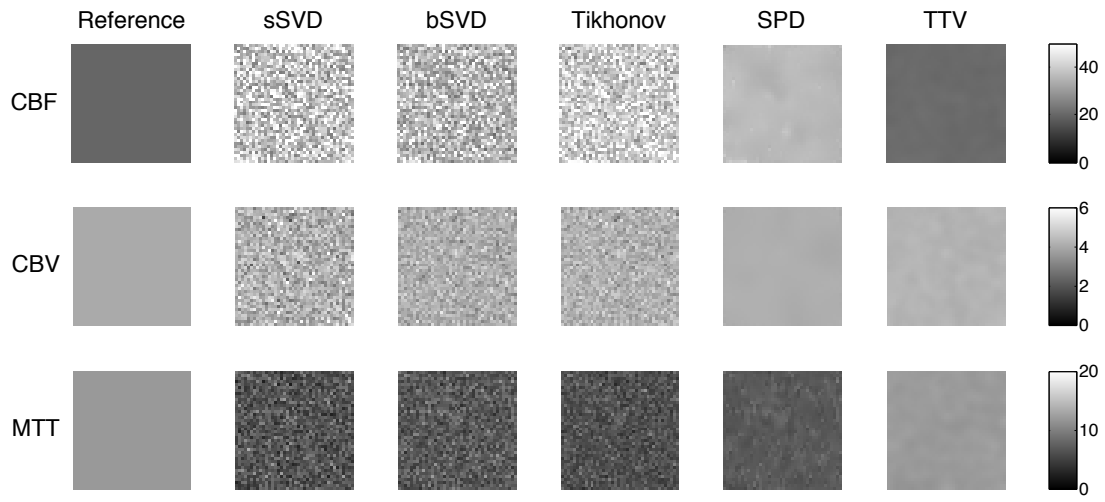

Figure 5.4: Visual comparison in a uniform regions of perfusion parameter estimation using baseline methods and TTV. The ideal variation is 0. The reference is the ground truth at CBV = 4 mL/100 g, CBF = 20 mL/100 g/min, MTT = 12 s, PSNR = 15.

increases, TTV method appears to be more robust.

3) The ideal variability of the uniform region should be zero. Fig. 5.4 shows the estimated perfusion maps of the reference and four methods on the uniform region. While the baseline methods behave poorly in recovering the smooth region, TTV results in uniform perfusion maps for all three parameters at PSNR = 15. SPD reduces the noise level in estimating the three maps compared to other baseline methods, but the over-estimation in CBF and under-estimation in MTT could not be corrected using SPD. In comparison, TTV not only decreases the noise standard deviation in the estimated perfusion maps, but also restores the accurate quantitative parameters for CBF and MTT.

4) Quantitative comparison is shown in Fig. 5.5(a)-(b) (where CBF or MTT varies) and Fig. 5.5 (c)-(d) (where PSNR varies). All figures show that TTV produces lower CBF and MTT variations than the sSVD, bSVD and Tikhonov meth-

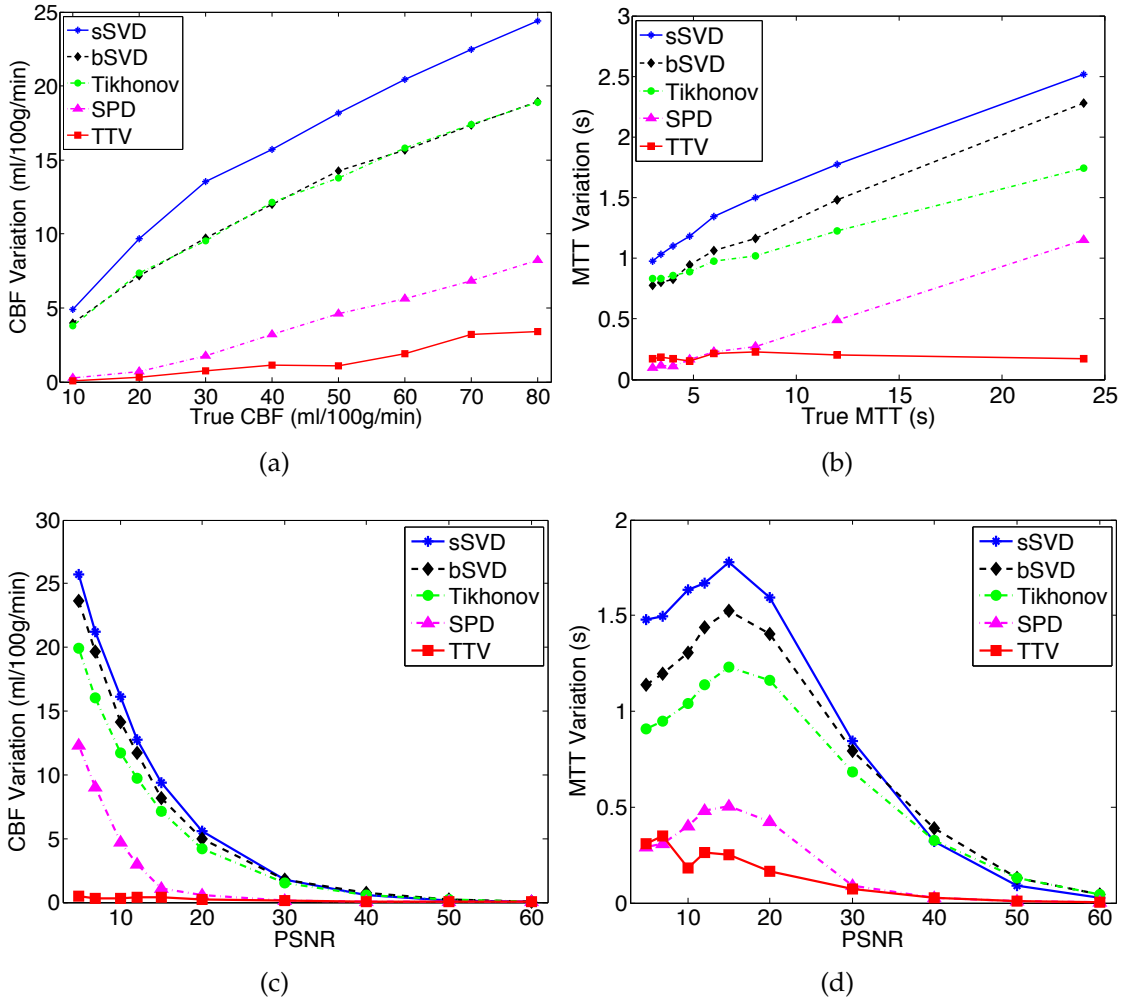

Figure 5.5: Comparisons of reducing variations over homogeneous region of (a) CBF at different CBF values with PSNR = 15. (b) MTT at different true MTT values with PSNR = 15. (c) CBF at different PSNR values with true CBF = 20 mL/100 g/min. (d) MTT at different PSNR values with true MTT = 12 s.

ods. SPD achieves relatively lower variation, but the mean estimated values of CBF and MTT in Fig. 5.3(c)-(d) shows under-estimation of MTT, compared to the ground truth. Table 5.1 shows the quantitative evaluation of the different methods in terms of RMSE and Lin's CCC for the results in Fig. 5.3-5.5.

Table 5.1: Quantitative evaluation of the perfusion parameters in Fig. 5.3-5.5. 'Estimated' mean the perfusion parameter to be estimated, 'varying' means the varying condition in the evaluation. The best performance is highlighted in bold font. Lin's CCC are not shown for varying PSNR because the true value for the estimated perfusion parameter does not change and thus Lin's CCC becomes zero. CBV does not change value in the experiment so for CBV estimation there is no varying CBV.

Estimated	CBF			MTT		
Varying	CBF		PSNR	MTT		PSNR
Method/Metric	RMSE	Lin's CCC	RMSE	RMSE	Lin's CCC	RMSE
sSVD	23.52	0.6878	52.07	6.056	0.4283	6.278
bSVD	15.05	0.8129	52.01	5.827	0.4567	6.309
Tikhonov	19.94	0.7198	43.92	5.64	0.4748	6.015
SPD	15.02	0.8294	44.36	5.804	0.4586	3.3323
TTV	**0.993**	**0.9991**	**0.7954**	**0.6847**	**0.9945**	**0.294**

Contrast preserving

Contrast is an important indicator of how well two neighboring different regions can be distinguished. The contrast of perfusion parameters between the normal and abnormal tissue computed using the deconvolution algorithm from the noisy data should be comparable to that of the noise-free CTP data. To compare the performance of the baseline methods and TTV in preserving contrast, we generate synthetic CTP data spatially containing two 40×20 uniform regions with different perfusion characteristic. Peak contrast-to-noise ratio (PCNR) is defined as PCNR = $\max|I_1 - I_2|/\sigma$, where I_1 and I_2 are the perfusion parameter values of then two images to be compared for contrast.

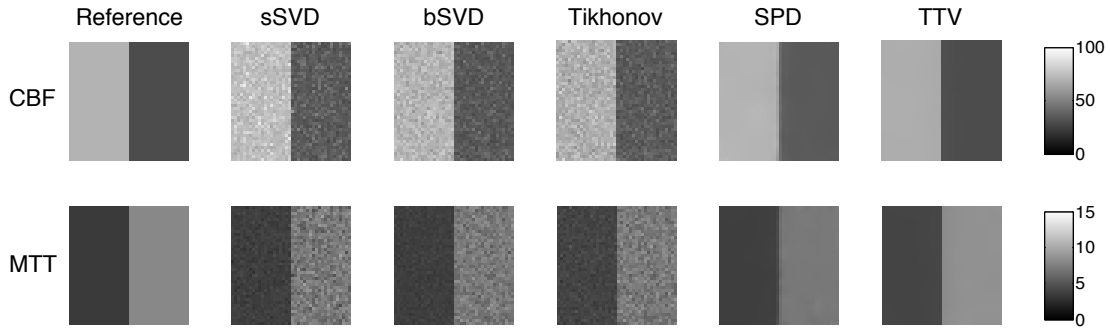

(a) PCNR=1

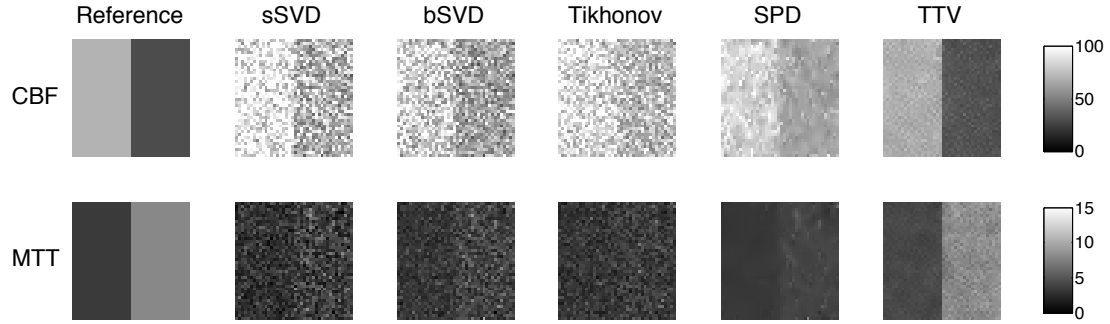

(b) PCNR=0.2

Figure 5.6: Comparisons of CBF and MTT estimated by the different deconvolution algorithms in preserving edges between two adjacent regions at PCNR=1 and 0.2. CBV is not shown because it is uniform in the region. True CBF is 70 and 30 mL/100 g/min on the left and right halves of the region. CBV is uniform in the region at 4 mL/100g. True MTT is 3.43 and 8 s on the left and right halves. Temporal resolution is 1 sec and total duration of 60 sec.

Fig. 5.6 shows the estimated CBF and MTT by the different algorithms when PCNR=1 and 0.2. The corresponding σ=40 and 200. While baseline methods sSVD, bSVD and Tikhonov perform poorly at both PCNR levels, SPD and TTV yield improved CBF and MTT maps with regard to the reference. When the PCNR = 1 and the noise level is moderate, both SPD and TTV are capable of removing the noise and preserve the contrast. However the spatial resolution at the boundary of two regions is smoothed by SPD, compared to the clear-cut

boundary using TTV. When the PCNR is as low as 0.2, the contrast to noise ratio is extremely low. sSVD, bSVD and Tikhonov generate severely biased perfusion parameters. SPD reduces the noise level to certain extent, but is unable to correct the estimation bias in CBF and MTT. TTV performs favorably compared to all baseline methods in preserving the edges between two adjacent regions in CBF and MTT, as well as accurate estimation of perfusion parameters.

5.3.2 Clinical evaluation

Because repetitive scanning of the same patient under different radiation levels is unethical, low-dose Perfusion maps are simulated from the high-dose 190 mAs by adding correlated statistical noise [6] with standard deviation of σ_a = 25.54, which yields PSNR=40. The maps calculated using bSVD from the 190 mAs high-dose CTP data is regarded as the "gold standard" or reference images in clinical experiments.

Visual Comparison

1) At reduced tube current-exposure time product (mAs), Fig. 5.7 shows significant differences visually between the CBF maps of the different deconvolution methods, where sSVD, bSVD, Tikhonov and SPD overestimate CBF while TTV estimates accurately. With decreased mAs and therefore reduced radiation dosage level, the over-estimation and the increased noise level become more apparent for the baseline algorithms. At all mAs levels, TTV is capable to accurately estimate CBF values compared to the reference.

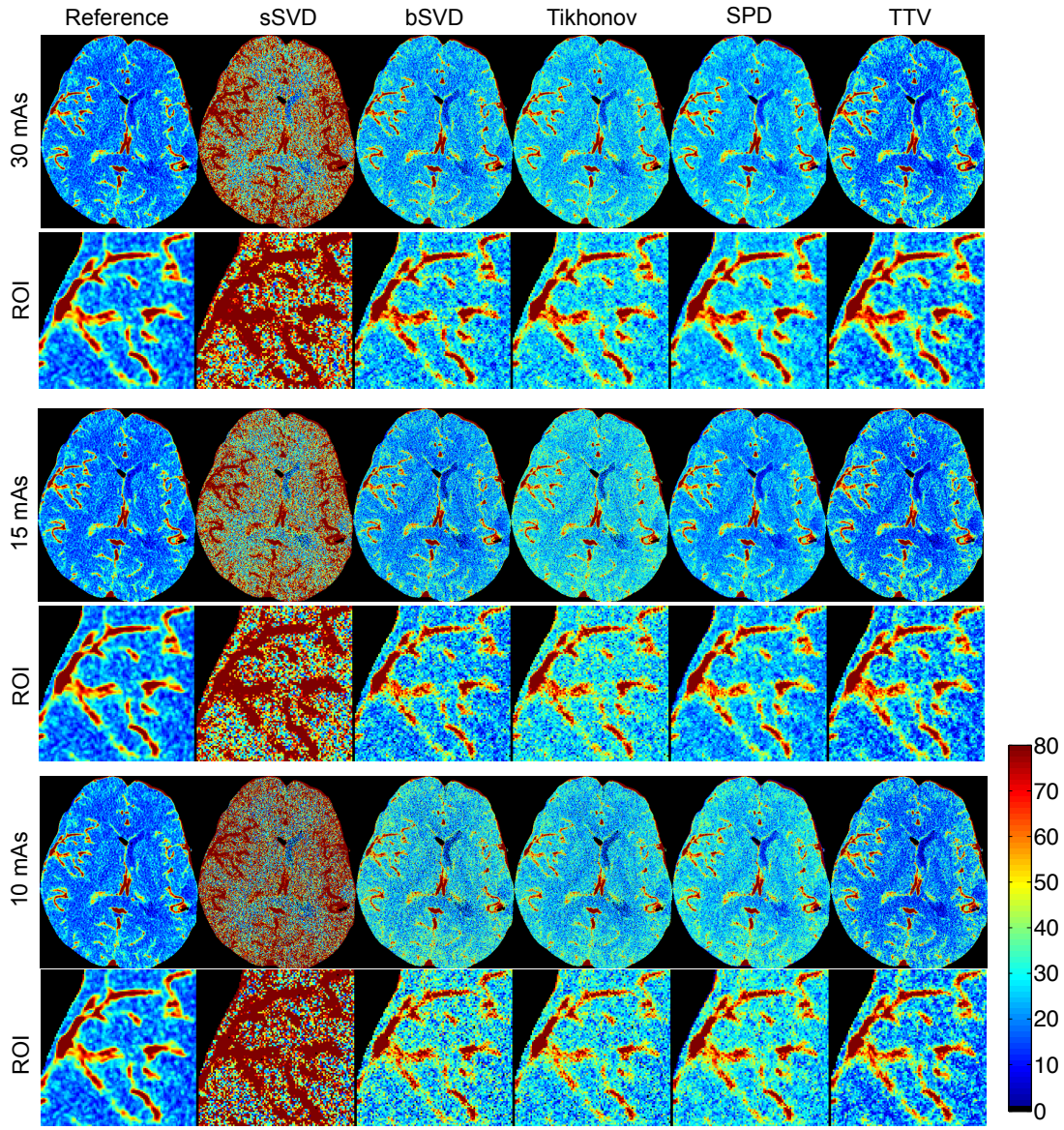

Figure 5.7: The CBF maps with zoomed ROI regions of a patients (ID 3) calculated using different deconvolution algorithms at tube current of 30, 15 and 10 mAs with normal sampling rate. Baseline methods sSVD, bSVD, Tikhonov and SPD overestimate CBF values, while TTV corresponds with the reference. As the tube current decreases and the radiation level reduces, the over-estimation of CBF values using baseline methods become more apparent. SPD method could remove the noise to certain extent compared to other baseline methods, but has limited ability to correct the over-estimation in the CBF value. (Color image)

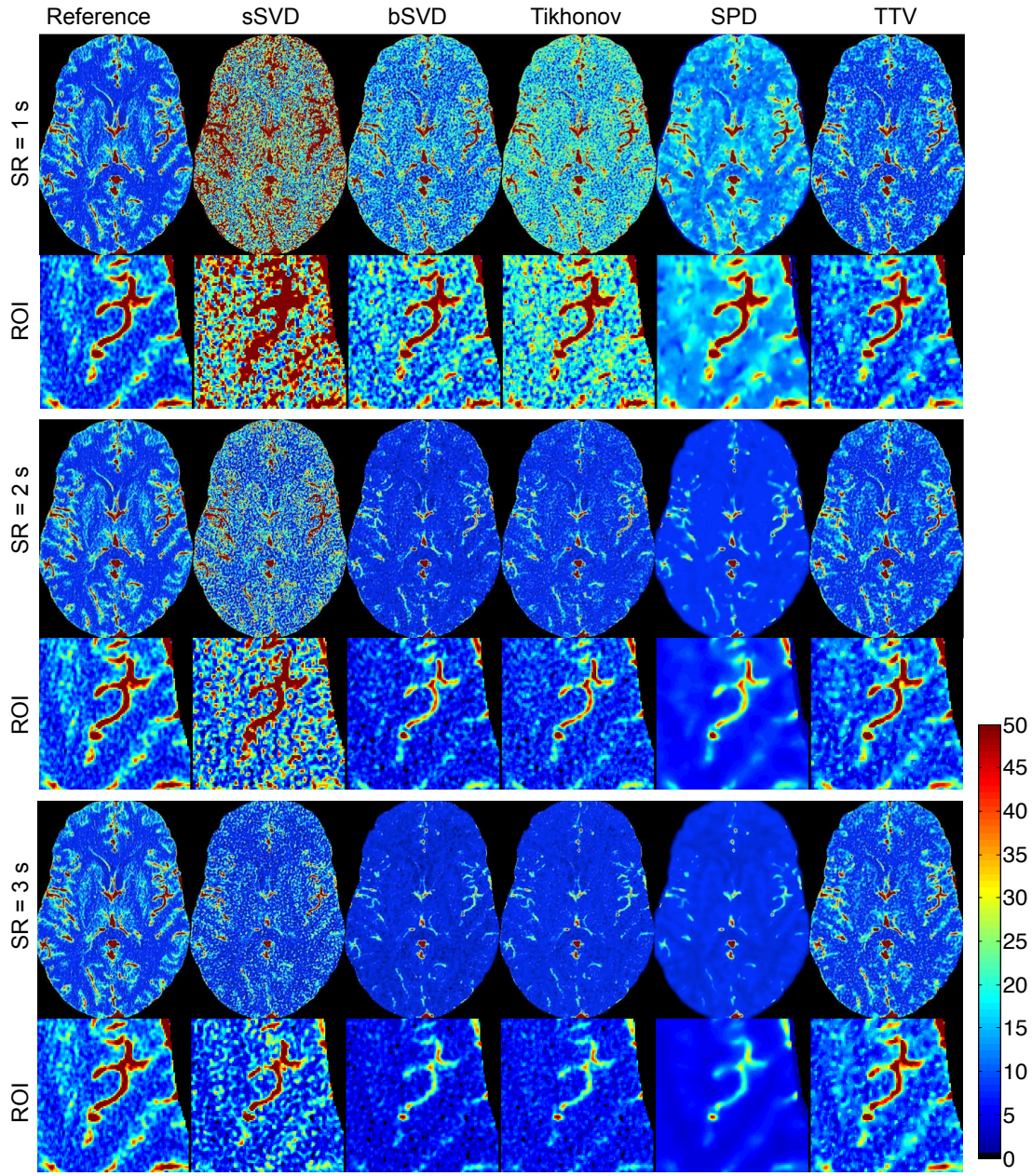

Figure 5.8: The CBF maps with roomed ROI regions of a patient (ID 9) computed using different deconvolution methods at sampling rate (SR) of 1 s, 2 s and 3 s with 15 mAs tube current. At normal sampling rate 1 s, baseline methods over-estimate CBF values. At reduced sampling frequency 2 s, sSVD still over-estimate while bSVD, Tikhonov and SPD under-estimate CBF values. At reduced sampling rate of 3 s, all baseline algorithms under-estimate CBF values. At all sampling rates, TTV accurately estimate the CBF values. (Color image)

2) At reduced temporal sampling rate of 2 s and 3 s, the errors of CBF estimation in the four baseline algorithms increase, while TTV maintains accurate estimation for CBF value at all sampling rates.

Quantitative comparison

There is significant improvement in image fidelity between the low-dose CBF maps and the high-dose CBF maps by using the TTV algorithm compared to the baseline methods. On average, the RMSE decreases by 40%, Lins CCC increases by 89% from the best performance by using the baseline methods (Table 2, Fig. 5.9). The quantitative values are computed with the vascular pixel elimination to exclude the influence of high blood flow values in the blood vessels.

Computation Time

It takes approximately 25 s to process a clinical dataset of $512 \times 512 \times 118$ by TTV method with 5 iterations, and approximately 0.83 s, 2.04 s and 1.35 s for sSVD, bSVD and Tikhonov algorithms. For SPD, it takes 80.6 s for the whole image. The TTV algorithm usually converges within 5 iterations. Though SVD and Tikhonov based methods are faster, the over-estimation, low spatial resolution, less differentiable tissue types and graining in the images are not acceptable. SPD and TTV have comparable high-quality results for the low-dose recovery, however TTV takes only 30% of the computation time compared to the time for SPD. Moreover, the output of TTV can generate all perfusion maps at the same time from optimized residue functions, while SPD needs to compute each perfusion map separately, resulting in 240 s for all three maps.

Table 5.2: Quantitative comparison of four methods on ten patients in terms of RMSE, Lins CCC and linear regression. Patients 1-5 have brain deficits due to aneurysmal SAH, while patients 6-10 have normal brain maps. The mean value for the deficit and normal subjects are computed respectively, as well as the mean value for all cases. The best performance is highlighted in bold font. Best performance among all methods is highlighted with bold font for each case and the average. * $P < .001$ in one-tail student test.

Methods	**Case**	**RMSE**	**Lin's CCC**	**Linear Regression**
sSVD		30.01	0.0242	y=0.289x-0.549
bSVD		6.41	0.156	y=0.826-1.457
Tikhonov	1	10.09	0.0454	y=0.693x-2.185
SPD		6.05	0.095	y=0.928x-5.219
TTV		**2.94**	**0.572**	y=1.069x-1.351
sSVD		22.42	0.059	y=0.416x-0.369
bSVD		7.3	0.207	y=0.877x-2.277
Tikhonov	2	10.44	0.114	y=0.781x-3.167
SPD		6.3907	0.3498	y=0.949x-3.327
TTV		**4.1**	**0.60**	y=1.164x+1.025
sSVD		18.65	0.034	y=0.192x+1.911
bSVD		6.1	0.117	y=0.516x-0.764
Tikhonov	3	9.9	0.044	y=0.405x+0.495

Continued on next page

Table 5.2 – *Continued from previous page*

Methods	Case	RMSE	Lin's CCC	Linear Regression
SPD		4.26	0.165	y=0.872x-7.704
TTV		**2.22**	**0.622**	y=0.829x+0.514
sSVD		25.68	0.0539	y=0.192x+1.91
bSVD		7.91	0.132	y=0.516x+0.764
Tikhonov	4	9.84	0.080	y=0.405x-0.495
SPD		6.73	0.171	y=0.822x-7.025
TTV		**4.59**	**0.451**	y=0.829x+0.514
sSVD		29.67	0.0322	y=0.192x+1.911
bSVD		9.09	0.117	y=0.516x+0.764
Tikhonov	5	12.22	0.0745	y=0.405x-0.495
SPD		5.23	0.183	y=1.183x-3.757
TTV		**4.78**	**0.338**	y=0.829x+0.514
sSVD		38.3	0.09	y=0.346x+0.232
bSVD		7.89	0.415	y=0.900x-2.13
Tikhonov	6	11.5	0.215	y=0.346x-3.41
SPD		6.35	0.702	y=1.045x-4.107
TTV		**3.39**	**0.807**	y=1.31x-1.77
sSVD		28.7	0.0391	y=0.382x-0.316
bSVD		11.7	0.1072	y=0.786x-2.959
Tikhonov	7	15.5	0.0605	y=0.714x-4.004
SPD		12.31	0.065	y=0.813x-9.093
TTV		**4.79**	**0.459**	y=1.127x+1.082

Continued on next page

Table 5.2 – *Continued from previous page*

Methods	Case	RMSE	Lin's CCC	Linear Regression
sSVD		23.5	0.0454	y=0.327x+1.008
bSVD		7.42	0.1626	y=0.799x-1.633
Tikhonov	8	11.6	0.0739	y=0.673x-2.398
SPD		4.91	0.1922	y-0.914x-4.985
TTV		**3.02**	**0.6398**	y=1.030x-0.618
sSVD		18.4	0.077	y=0.421x-0.539
bSVD		4.88	0.3571	y=0.917x-1.484
Tikhonov	9	11.00	0.0989	y=0.733x-3.46
SPD		3.71	0.513	y=1.033x-2.656
TTV		**2.29**	**0.7956**	y=1.045x-0.765
sSVD		21.55	0.0361	y=0.215x+2.298
bSVD		7.27	0.0801	y=0.542x+0.844
Tikhonov	10	10.63	0.147	y=0.457x+0.595
SPD		4.32	0.232	y=1.028x-3.968
TTV		**4.21**	**0.308**	y=1.012x+1.667
sSVD		29.22	0.052	
bSVD		7.72	0.205	
Tikhonov	Deficit	10.82	0.106	
SPD		6.15	0.300	
TTV		**3.96***	**0.554**	
sSVD		22.16	0.046	
bSVD		7.47	0.165	

Continued on next page

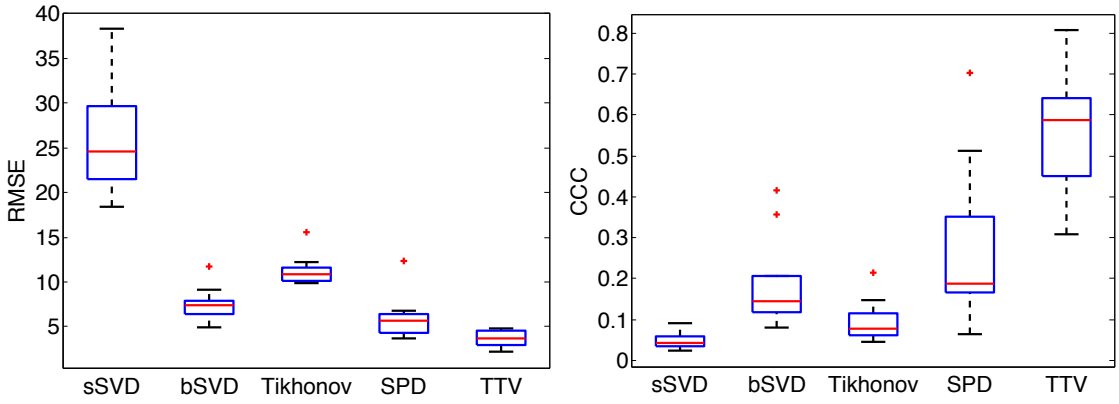

(a) (b)

Figure 5.9: Comparisons of RMSE and Lin's CCC among the four methods. TTV results in significant ($P < 0.001$) lower RMSE and higher Lin's CCC compared with all the baseline methods.

Table 5.2 – *Continued from previous page*

Methods	**Case**	**RMSE**	**Lin's CCC**	**Linear Regression**
Tikhonov	Normal	11.73	0.085	
SPD		5.90	0.233	
TTV		**3.31***	**0.565**	
sSVD		25.69	0.049	
bSVD		7.60	0.185	
Tikhonov	All	11.27	0.095	
SPD		6.03	0.267	
TTV		**3.63***	**0.505**	

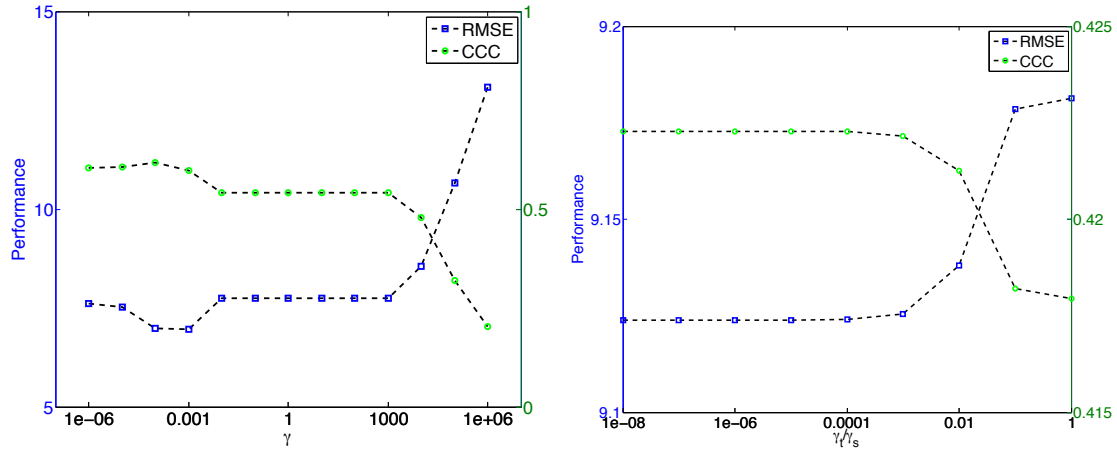

Figure 5.10: Performace in terms of root-mean-square-error (RMSE) for different parameters (a) γ and (b) ratio γ_t/γ_s.

Parameters

In the TTV algorithm, there is only a single type of tunable parameter: the TV regularization weight. If the spatial and temporal regularization are treated equally, only one weighting parameter γ needs to be determined. Fig. 5.10(a) show the RMSE and Lin's CCC at different γ values. When $\gamma < 10^3$, RMSE and Lin's CCC does not change much. The optimal γ is between 10^{-4} to 10^{-3}.

Since the temporal and the spatial dimensions of the residue impulse functions have different scaling, regularization parameters for t and x, y, z should be different too. We set the spatial $\gamma_s = \gamma_{x,y,z} = 10^{-4}$ since the spatial dimensions have similar scaling, and tune the ratio between the temporal weight γ_t and spatial weight γ_s. Fig. 5.10(b) shows that when the ratio $\gamma_t/\gamma_s < 10^{-4}$, the performance is stable. Thus we set $\gamma_t = 10^{-8}$ and $\gamma_s = 10^{-4}$ for all experiments.

5.4 Discussion

In this study, a new total variation regularization algorithm is proposed to improve the quality and quantification of the low-dose CTP perfusion maps and extensively compared with the existing widely used algorithms, e.g. sSVD, bSVD, Tikhonov and SPD regularizations. Synthetic evaluation with accurate ground truth data is used to compare the quality of the residue functions, uniform regions, contrast preserving, sensitivity to blood flow value, noise levels and sampling rate. Clinical evaluation using high-dose perfusion maps as the reference image is conducted to show the visual quality of the perfusion maps at low-dose and the sampling rate compared with the high-dose maps.

When the SVD-based algorithms were first introduced in 1996 [81, 80], the perfusion parameters were computed from each tissue voxel independently. It assumes the X-ray radiation and intravenous injection were high enough to generate accurate tissue enhancement curves and AIF for deconvolution. However, SVD-based methods tend to introduce unwanted oscillations [77, 7] and results in overestimation of CBF and underestimation of MTT, especially in low-dose scan setting. The severely distorted residue functions estimated by the baseline methods at simulate 15 mAs tube current in our synthetic evaluation reveal the inherent problem existent in the SVD-based methods: instability. These methods are sensitive to noise in the low-dose environment, and lead to unrealistic oscillations in the residue function, which is the starting point for all perfusion parameter computation.

This instability could be alleviated using the context information in the neighboring tissue voxels with the assumption of a piece-wise smooth model:

The residue functions within the extended neighborhood of a tissue voxel will have constant or similar shape, while the changes on the boundary between different regions where tissues undergo perfusion changes should be identified and preserved. The tensor total variation term in the objective function Eq. 5.18 penalizes large variation of residue functions within the extended neighborhood of the tissue voxels, and adopting the L_1 norm in summing the gradient of all voxels. It avoids the much greater quadratic penalty of L_2 norm at boundaries between different regions where large change in the residue functions occur. In one word, the contextual tissue voxels jointly identify the ground truth residue functions while reducing the statistical correlated noise due to the low-dose radiation.

The synthetic evaluations show that the residue functions computed by the baseline methods are unrealistically oscillating, leading to erroneous values of CBF, CBV and MTT. These baseline methods constantly over-estimate the value of CBF and the errors increase exponentially as PSNR decreases. This misleading over-estimation may cause neglect of infarct core or ischemic penumbra in the patients with acute stroke or other cerebral deficits, resulting in delay in diagnosis and treatment. The large variation in the uniform synthetic region and contrast regions are also caused by the oscillating nature of the results, and introduce misleading information in judging the perfusion condition of the healthy and the ischemic regions.

On the contrary, the proposed TTV method performs comparably to the 190 mAs high-dose results on the 15 mAs low-dose data, which is approximately 8% of the original dose used. The residue functions are stable and have the same shape as the ground truth. Perfusion parameters correlate well with the

ground truth, without significant overestimation or under-estimation. The variation in the uniform regions is significantly suppressed, while the edges in the contrast regions are more identifiable. The clinical evaluations show similar performance comparing the baseline methods and TTV algorithm. While the baseline methods significantly over-estimate CBF values, one of the most important perfusion parameter for stroke diagnosis in recently research [103], TTV yields comparable CBF maps to the reference maps. Moreover, the vascular structure and tissue details are well preserved by the TTV algorithm by removing the noise and maintaining the spatial resolution. Different evaluation metrics and statistical tests further verify the correlation between the perfusion parameters of the low-dose maps computed by TTV and the reference maps.

There is only one type of parameter γ in the model, which determines the trade-off between data fidelity and TV regularization. Through extensive evaluation, we find that the results are not sensitive to the change of γ in the range of 10^{-6} to 10^{-4}, and the ratio between the temporal and spatial regularization weight in the range of 10_{-8} to 10^{-4}. So we set $\gamma_s = 10^{-4}$ and $\gamma_t = 10^{-8}$ for all the experiments.

There are several limitations to our study. First, CT perfusion imaging data from only 10 patients are used. Some patients have perfusion deficits due to SAH, but other brain perfusion deficits such as acute stroke are not included. Further validation should be conducted by using larger and more diverse data sets. However the aim of our study is to propose a new robust low-dose deconvolution algorithm and validate it preliminarily on synthetic and clinical data, and the improvement on low-dose quantification is significant enough to show the advantage of the proposed method. Second, SVD-based algorithms are used

as baseline methods to compare with the proposed TTV. There are other existing methods to post-process the CTP imaging data, including maximum slope (MS), inverse filter (IF) and box-modulated transfer function (bMTF). Further comparison with these post-processing methods should be conducted. But MS, IF and bMTF are not designed for low-dose CTP imaging data, while TTV uses the contextual information for low-dose CTP deconvolution.

In conclusion, we propose a robust low-dose CTP deconvolution algorithm using tensor total variation regularization that significantly improves the quantification of the perfusion maps in CTP data at a dose level as low as 8% of the original level. In particular, the over-estimation of CBF and under-estimation of MTT, presumably owing to the oscillatory nature of the results produced by the existing methods, is overcome by the total variation regularization in the proposed method. The proposed method could potentially reduce the necessary radiation exposure in clinical practices and significantly improve patient safety in CTP imaging.

CHAPTER 6

CONCLUSIONS

Robust deconvolution for low-dose medical imaging has received significant attention in recent works. Intra-subject contextual information is often exploited to remove the noise and artifacts in the restored hemodynamic maps. In this thesis, we took a closer look at the role of inter-subject contextual information in robust deconvolution. Specifically, we explored its importance in three aspects. First: *Informatics* acquisition. We found, through synthetic evaluation as well as in-vivo clinical data, that inter-subject context provide complimentary information to improve the accuracy of cerebral blood flow map estimation and increase the differentiation between normal and deficit tissue. Second: Disease *diagnosis*. We showed that apart from the global learned dictionary for hemodynamic maps, the tissue-specific dictionaries can be effectively leveraged for disease diagnosis tasks as well, especially for low-contrast tissue types where the brain deficits usually occur. Lastly: *Treatment* plan. We proposed a generalized framework with inter-subject context through dictionary learning and sparse representation possible for any hemodynamic parameter estimation, such as blood-brain-barrier permeability. We also extended to include inter-subject context through tensor total variation. The diverse hemodynamic maps provide necessary information for treatment plan decision making. We presented results of our approaches on a variety of datasets and clinical tasks, such as uniform regions estimation, contrast preservation, data acquired at low-sampling rate and

low radiation dose levels.

6.1 Future Work

The following are different directions I would like to pursue in the future using my previous work as a stepping stone, via collaborations with researchers in neuroscience, data science and artificial intelligence.

6.1.1 Extension to other imaging modalities

I would like to investigate a similar approach in a variety of medical imaging modalities such as MRI and SPECT/CT for dictionary learning of inter-subject context. High-quality dictionary can be learned from high quality medical data to capture the spatio-temporal patterns. For instance, for arterial spin labeling MRI (ASL-MRI), repetitive scans are usually performed numerous times to obtain an average spatio-temporal MRI sequence with high signal-to-noise ratio (SNR). We can learn a dictionary from the existing average ASL-MRI data with high SNR, and utilize the atoms in the dictionary as building blocks to restore the new ASL-MRI data with fewer repetitive scans. Although it may seem like a direct application of the above algorithm developed for MRI modality, it opens up a new realm of possible applications as such fast ASL-MRI to capture transit functional changes, high resolution functional imaging and SPECT with lower dose of radioactive tracer.

6.1.2 Incorporating multi-modality and information beyond images

So far my current work has relied mostly on inter- or intra-subject visual data of the same imaging modality. Multi-modality information such as dMRI, fMRI, EEG and PET can also be incorporated. This would allow us to leverage a new set of statistics to better learn the spatio-temporal patterns. Moreover, incorporating multi-modality information would allow for more robust recovery of certain structures such as ligament and tendon injuries, spinal cord that are currently with limited clarity in CTP.

It would be interesting to explore other forms of information such as text associated with medical images, and perhaps learn a meaningful pattern on the textual signals, so that the visual and textual information enhance each other in selecting the suitable dictionary patches. Alternatively, the textual entities can be incorporated into the visual dictionary. Thus the patterns learned can now represent the visual spatio-temporal patterns as well the demographical and diagnosis records of the subjects. For example, the dictionary of brain tumor patients can be learned based on the age, gender, ethnics and medical history of the patient database. Each of these elements can be further leveraged when a new subject's low quality data needs to be restored. This would allow for a very rich and multi-modal dictionary of certain disease or demographical group.

6.1.3 Structured Sparsity

So far the tissue-specific dictionaries are learned from the segments of each tissue types from the training data. Only the labels of the voxels are considered in this proposed model, without exploiting the interactions between the tissue labels and the positions of the voxels with different labels. It is desirable to further employ the connectivity among the voxels with their labels. For instance, deep gray matter is usually located near the cerebrospinal fluid in the anterior central arterial area of the brain. The relative position of the tissue types and their connectivity can be incorporated as prior constraint using structured sparsity or group sparsity [46, 47]. Spatial connectivity can be encoded as groups and modeled as a regularization term. Thus all voxels within the same group have similar probability to be classified as one tissue type in the restoration.

Furthermore, the segmentation and the restoration could help each other in an iterative manner. Improved signal-to-noise ratio in the perfusion maps using the proposed deconvolution could assist more accurate segmentation of the tissue structures. More accurate segmentation of the tissue structure would in turn improve the patch selection in the sparse representation stage from the corresponding dictionary. This iterative process would be an interesting direction to explore to boost both segmentation accuracy and deconvolution robustness.

6.1.4 Clinical Trials

Another interesting future work that I wish to explore is to perform large-scale clinical trials with real low-dose scans. So we could understand the extent to which the radiation dose can be reduced by our proposed sparse representa-

tion algorithm for normal and different diseased cases. For instance, we could scan the voluntary subjects twice at a normal dose and a low-dose, for instance, 100 mAs and 10 mAs, where the total radiation dose level is below the FDA regulation of maximum 200 mAs.

We would apply our algorithm to leverage the inter-patient contextual information and evaluate the quantitative differences between the normal-dose perfusion maps and the restored low-dose perfusion maps. We would also present the three types of maps (normal-dose, low-dose and restored low-dose) to the neuroradiologists to evaluate the diagnosis accuracy and then determine the lowest achievable tube current level with acceptable image quality and without any substantial artifacts affecting diagnostic confidence using our algorithm. The subjective evaluation include assessment of image noise, visibility of small structures, ischemic region size, delineation and conspicuity, and diagnostic confidence in a blinded fashion. Statistical analysis will also be performed to evaluate the statistical significance of the results. The clinical trials would allow possibility to evaluate the effectiveness of the deconvolution algorithm on real low radiation dose data, instead of the simulated low-dose data, therefore giving way to potential clinical application of the proposed deconvolution algorithms and dose reduction in CTP scans.

APPENDIX A

RELATED PUBLICATIONS

Journal papers:

- Ruogu Fang, Kolbeinn Karlsson, Tsuhan Chen, Pina C. Sanelli. Improving Low-Dose Blood-Brain Barrier Permeability Quantification Using Sparse High-Dose Induced Prior for Patlak Model. Medical Image Analysis, Volume 18, Issue 6, Pages 866-880, 2014.
- Ruogu Fang, Tsuhan Chen, Pina Sanelli. Towards Robust Deconvolution of Low-Dose Perfusion CT: Sparse Perfusion Deconvolution Using Online Dictionary Learning. Medical Image Analysis, Volume 17, Issue 4, Pages 417-428, 2013.

Conference papers:

- Ruogu Fang, Pina Sanelli, Shaoting Zhang, Tsuhan Chen. Tensor Total-Variation Regularized Deconvolution for Efficient Low-Dose CT Perfusion. The 17th Annual International Conference on Medical Image Computing and Computer Assisted Intervention, 2014 (MICCAI 2014)
- Ruogu Fang, Tsuhan Chen, Pina Sanelli. Tissue-Specific Sparse Deconvolution for Low-Dose CT Perfusion. The 16th Annual International Conference on Medical Image Computing and Computer Assisted Intervention, 2013 (MICCAI 2013)

- Ruogu Fang, Andrew C. Gallagher, Tsuhan Chen, Alexander Loui. Kinship Classification by Modeling Facial Feature Heredity. The 20th International Conference on Image Processing, 2013 (ICIP 2013)
- Ruogu Fang, Tsuhan Chen, Pina Sanelli. Sparsity-Based Deconvolution of Low-Dose Perfusion CT Using Learned Dictionaries. The 15th Annual International Conference on Medical Image Computing and Computer Assisted Intervention, Lecture Notes in Computer Science Volume 7510, pp. 272-280, 2012 (MICCAI 2012)
- Ruogu Fang, Tsuhan Chen, Pina Sanelli. Sparsity-Based Deconvolution Of Low-Dose Brain Perfusion CT In Subarachnoid Hemorrhage Patients. The 9th International Symposium on Biomedical Imaging, pp. 872-875, 2012 (ISBI 2012)
- Ruogu Fang, Ashish Raj, Tsuhan Chen, Pina C. Sanelli. Radiation dose reduction in computed tomography perfusion using spatial-temporal Bayesian methods. In Proceedings of SPIE Medical Imaging, Volume 8313, Paper 831345, 2012 (SPIE 2012)
- Ruogu Fang, Ramin Zabih, Ashish Raj, Tsuhan Chen. Segmentation of Liver Tumor Using Efficient Global Optimal Tree Metrics Graph Cuts. Abdominal Imaging, pp. 51-59, 2011. (AI 2011)
- Ruogu Fang, Kevin D. Tang, Noah Snavely, Tsuhan Chen. Towards Computational Models of Kinship Verification. The 17th IEEE International Conference on Image Processing, 2010 (ICIP 2010)
- Ruogu Fang, Joyce Yu-hsin Chen, Ramin Zabih, Tsuhan Chen. Tree-Metrics Graph Cuts For Brain MRI Segmentation With Tree Cutting. IEEE Western New York Image Processing Workshop, pp. 10-13, 2010 (WNYIPW 2010)

BIBLIOGRAPHY

[1] M. Aharon, M. Elad, and A. Bruckstein. K-SVD: An algorithm for designing of overcomplete dictionaries for sparse representation. *Signal Processing, IEEE Transactions on*, 54(11):4311–4322, 2006.

[2] I.K. Andersen, A. Szymkowiak, C.E. Rasmussen, LG Hanson, JR Marstrand, H.B.W. Larsson, and L.K. Hansen. Perfusion quantification using Gaussian process deconvolution. *Magnetic Resonance in Medicine*, 48(2):351–361, 2002.

[3] Cristian T Badea, Samuel M Johnston, Yi Qi, and G Allan Johnson. 4D micro-CT for cardiac and perfusion applications with view under sampling. *Physics in medicine and biology*, 56(11):3351, 2011.

[4] Amir Beck and Marc Teboulle. A fast iterative shrinkage-thresholding algorithm with application to wavelet-based image deblurring. In *Acoustics, Speech and Signal Processing, 2009. ICASSP 2009. IEEE International Conference on*, pages 693–696. IEEE, 2009.

[5] S Bisdas, M Hartel, LH Cheong, TS Koh, and TJ Vogl. Prediction of subsequent hemorrhage in acute ischemic stroke using permeability CT imaging and a distributed parameter tracer kinetic model. *Journal of neuroradiology*, 34(2):101–108, 2007.

[6] AJ Britten, M. Crotty, H. Kiremidjian, A. Grundy, and EJ Adam. The addition of computer simulated noise to investigate radiation dose and image quality in images with spatial correlation of statistical noise: an example application to X-ray CT of the brain. *British journal of radiology*, 77(916):323–328, 2004.

[7] F. Calamante, D.G. Gadian, and A. Connelly. Quantification of bolus-tracking MRI: Improved characterization of the tissue residue function using Tikhonov regularization. *Magnetic resonance in medicine*, 50(6):1237–1247, 2003.

[8] E.J. Candès, J. Romberg, and T. Tao. Robust uncertainty principles: exact signal reconstruction from highly incomplete frequency information. *Information Theory, IEEE Transactions on*, 52(2):489–509, February 2006.

[9] Aleksa Cenic, Darius G. Nabavi, Rosemary A. Craen, Adrian W. Gelb, and Ting-Yim Lee. Dynamic CT measurement of cerebral blood flow: A validation study. *American Journal of Neuroradiology*, 20(1):63–73, 1999.

[10] Aleksa Cenic, Darius G. Nabavi, Rosemary A. Craen, Adrian W. Gelb, and Ting-Yim Lee. A CT method to measure hemodynamics in brain tumors: Validation and application of cerebral blood flow maps. *American Journal of Neuroradiology*, 21(3):462–470, 2000.

[11] S. Chen, S.A. Billings, and W. Luo. Orthogonal least squares methods and their application to non-linear system identification. *International Journal of Control*, 50(5):1873–1896, 1989.

[12] S.S. Chen, D.L. Donoho, and M.A. Saunders. Atomic decomposition by basis pursuit. *SIAM review*, 43(1):129–159, 2001.

[13] A Cianfoni, S Cha, WG Bradley, WP Dillon, and M Wintermark. Quantitative measurement of blood-brain barrier permeability using perfusion-CT in extra-axial brain tumors. *Journal of neuroradiology*, 33(3):164–168, 2006.

[14] Wayne M Clark, Gregory W Albers, Kenneth P Madden, Scott Hamilton, et al. The rtPA (Alteplase) 0-to 6-hour acute stroke trial, part A (A0276g) Results of a double-blind, placebo-controlled, multicenter study. *Stroke*, 31(4):811–816, 2000.

[15] JW Dankbaar, J Hom, T Schneider, S-C Cheng, BC Lau, I van der Schaaf, S Virmani, S Pohlman, WP Dillon, and M Wintermark. Dynamic perfusion CT assessment of the blood-brain barrier permeability: first pass versus delayed acquisition. *American Journal of Neuroradiology*, 29(9):1671–1676, 2008.

[16] D.L. Donoho. Compressed sensing. *Information Theory, IEEE Transactions on*, 52(4):1289–1306, 2006.

[17] D.L. Donoho. For most large underdetermined systems of linear equations the minimal 1-norm solution is also the sparsest solution. *Communications on pure and applied mathematics*, 59(6):797–829, 2006.

[18] B. Efron, T. Hastie, I. Johnstone, and R. Tibshirani. Least angle regression. *The Annals of statistics*, 32(2):407–499, 2004.

[19] Andrew J Einstein, Milena J Henzlova, and Sanjay Rajagopalan. Estimating risk of cancer associated with radiation exposure from 64-slice computed tomography coronary angiography. *JAMA: the journal of the American Medical Association*, 298(3):317–323, 2007.

[20] Michael Elad and Michal Aharon. Image denoising via sparse and redundant representations over learned dictionaries. *Image Processing, IEEE Transactions on*, 15(12):3736–3745, 2006.

[21] K. Engan, S.O. Aase, and J. Hakon Husoy. Method of optimal directions for frame design. In *Acoustics, Speech, and Signal Processing, 1999. Proceedings., 1999 IEEE International Conference on*, volume 5, pages 2443–2446. IEEE, 1999.

[22] R. Eslami and H. Radha. Translation-invariant contourlet transform and its application to image denoising. *Image Processing, IEEE Transactions on*, 15(11):3362–3374, 2006.

[23] R. Fang, T. Chen, and P. Sanelli. Sparsity-based deconvolution of low-dose perfusion CT using learned dictionaries. *Medical Image Computing and Computer-Assisted Intervention–MICCAI 2012*, pages 272–280, 2012.

[24] R. Fang, T. Chen, and P. C. Sanelli. Sparsity-based deconvolution of low-dose brain perfusion CT in subarachnoid hemorrhage patients. In *Biomedical Imaging (ISBI), 2012 9th IEEE International Symposium on*, pages 872–875. IEEE, 2012.

[25] R. Fang, A. Raj, T. Chen, and P.C. Sanelli. Radiation dose reduction in computed tomography perfusion using spatial-temporal bayesian methods. *Proc. SPIE Medical Imaging 2012: Physics of Medical Imaging*, 8313, 2012.

[26] Ruogu Fang, Tsuhan Chen, and Pina C Sanelli. Tissue-specific sparse deconvolution for low-dose ct perfusion. In *Medical Image Computing and Computer-Assisted Intervention–MICCAI 2013*, pages 114–121. Springer, 2013.

[27] Ruogu Fang, Tsuhan Chen, and Pina C. Sanelli. Towards robust deconvolution of low-dose perfusion CT: Sparse perfusion deconvolution using online dictionary learning. *Medical Image Analysis*, 17(4):417 – 428, 2013.

[28] Ruogu Fang, Y.J. Chen, R. Zabih, and Tsuhan Chen. Tree-metrics graph cuts for brain mri segmentation with tree cutting. In *Image Processing Workshop (WNYIPW), 2010 Western New York*, pages 10–13, 2010.

[29] Ruogu Fang, Andrew C Gallagher, Tsuhan Chen, and Alexander C Loui. Kinship classification by modeling facial feature heredity. In *The 20th International Conference on Image Processing*, pages 2983–2987, 2013.

[30] Ruogu Fang, Kolbeinn Karlsson, Tsuhan Chen, and Pina C Sanelli. Improving low-dose blood–brain barrier permeability quantification using sparse high-dose induced prior for patlak model. *Medical image analysis*, 18(6):866–880, 2014.

[31] Ruogu Fang, Pina C Sanelli, and Tsuhan Chen. Tensor total-variation regularized deconvolution for efficient low-dose ct perfusion. In *The 17th Annual International Conference on Medical Image Computing and Computer-Assisted Intervention–MICCAI 2014*. Springer, 2014.

[32] Ruogu Fang, K.D. Tang, N. Snavely, and Tsuhan Chen. Towards computational models of kinship verification. In *Image Processing (ICIP), 2010 17th IEEE International Conference on*, pages 1577–1580, 2010.

[33] Ruogu Fang, Ramin Zabih, Ashish Raj, and Tsuhan Chen. Segmentation of liver tumor using efficient global optimal tree metrics graph cuts. In Hiroyuki Yoshida, Georgios Sakas, and MariusGeorge Linguraru, editors, *Abdominal Imaging. Computational and Clinical Applications*, volume 7029 of *Lecture Notes in Computer Science*, pages 51–59. Springer Berlin Heidelberg, 2012.

[34] A. Fieselmann, M. Kowarschik, A. Ganguly, J. Hornegger, and R. Fahrig. Deconvolution-based CT and MR brain perfusion measurement: theoretical model revisited and practical implementation details. *Journal of Biomedical Imaging*, 2011:14, 2011.

[35] M.A.T. Figueiredo, R.D. Nowak, and S.J. Wright. Gradient projection for sparse reconstruction: Application to compressed sensing and other inverse problems. *Selected Topics in Signal Processing, IEEE Journal of*, 1(4):586–597, 2007.

[36] Dominik Fleischmann, Geoffrey D Rubin, Alexander A Bankier, and Karl Hittmair. Improved uniformity of aortic enhancement with customized contrast medium injection protocols at CT angiography1. *Radiology*, 214(2):363–371, 2000.

[37] Jasper Florie, Rogier E van Gelder, Michiel P Schutter, Adrienne van Randen, Henk W Venema, Steven de Jager, Victor PM van der Hulst, Anna Prent, Shandra Bipat, Patrick MM Bossuyt, et al. Feasibility study of computed tomography colonography using limited bowel preparation at normal and low-dose levels study. *European radiology*, 17(12):3112–3122, 2007.

[38] W.T. Freeman, T.R. Jones, and E.C. Pasztor. Example-based super-resolution. *Computer Graphics and Applications, IEEE*, 22(2):56–65, 2002.

[39] Donald P Frush, Lane F Donnelly, and Nancy S Rosen. Computed tomography and radiation risks: what pediatric health care providers should know. *Pediatrics*, 112(4):951–957, 2003.

[40] Donald P Frush, Christopher C Slack, Caroline L Hollingsworth, George S Bisset, Lane F Donnelly, Jiang Hsieh, Trudy Lavin-Wensell, and John R Mayo. Computer-simulated radiation dose reduction for abdominal multidetector CT of pediatric patients. *American Journal of Roentgenology*, 179(5):1107–1113, 2002.

[41] Kouzou Hanai, Tetsuya Horiuchi, Junko Sekiguchi, Yoshihisa Muramatsu, Ryutaro Kakinuma, Noriyuki Moriyama, Ryosuke Tuchiiya, and Noboru Niki. Computer-simulation technique for low dose computed tomographic screening. *Journal of computer assisted tomography*, 30(6):955–961, 2006.

[42] MarkR. Harrigan, Jody Leonardo, KevinJ. Gibbons, LeeR. Guterman, and L.Nelson Hopkins. CT perfusion cerebral blood flow imaging in neurological critical care. *Neurocritical Care*, 2:352–366, 2005.

[43] L. He, B. Orten, S. Do, WC Karl, A. Kambadakone, DV Sahani, and H. Pien. A spatio-temporal deconvolution method to improve perfusion CT quantification. *Medical Imaging, IEEE Transactions on*, 29(5):1182–1191, 2010.

[44] E.G. Hoeffner, I. Case, R. Jain, S.K. Gujar, G.V. Shah, J.P. Deveikis, R.C. Carlos, B.G. Thompson, M.R. Harrigan, and S.K. Mukherji. Cerebral perfusion CT: Technique and clinical applications. *Radiology*, 231(3):632–644, 2004.

[45] J. Huang, S. Zhang, and D. Metaxas. Efficient MR image reconstruction for compressed MR imaging. *Medical Image Analysis*, 15(5):670–679, 2011.

[46] Junzhou Huang, Xiaolei Huang, and Dimitris Metaxas. Learning with dynamic group sparsity. In *Computer Vision, 2009 IEEE 12th International Conference on*, pages 64–71. IEEE, 2009.

[47] Junzhou Huang, Tong Zhang, and Dimitris Metaxas. Learning with structured sparsity. *The Journal of Machine Learning Research*, 12:3371–3412, 2011.

[48] Yoshimasa Imanishi, Atsushi Fukui, Hiroshi Niimi, Daisuke Itoh, Kyouko Nozaki, Shunsuke Nakaji, Kumiko Ishizuka, Hitoshi Tabata, Yu Furuya, Masahiko Uzura, et al. Radiation-induced temporary hair loss as a radiation damage only occurring in patients who had the combination of MDCT and DSA. *European radiology*, 15(1):41–46, 2005.

[49] Assia Jaillard, Catherine Cornu, Anne Durieux, Thierry Moulin, Florent Boutitie, Kennedy R. Lees, Marc Hommel, and on behalf of the MAST-E Group. Hemorrhagic transformation in acute ischemic stroke: The MAST-E study. *Stroke*, 30(7):1326–1332, 1999.

[50] Xun Jia, Yifei Lou, Bin Dong, Zhen Tian, and Steve Jiang. 4D computed tomography reconstruction from few-projection data via temporal non-local regularization. In *Medical Image Computing and Computer-Assisted Intervention–MICCAI 2010*, pages 143–150. Springer, 2010.

[51] K Juluru, JC Shih, A Raj, JP Comunale, H Delaney, ED Greenberg, C Hermann, YB Liu, A Hoelscher, N Al-Khori, et al. Effects of increased image noise on image quality and quantitative interpretation in brain CT perfusion. *American Journal of Neuroradiology*, 2013.

[52] A Kemmling, H Wersching, K Berger, S Knecht, C Groden, and I Nölte. Decomposing the hounsfield unit. *Clinical neuroradiology*, 22(1):79–91, 2012.

[53] L.E. Kershaw and H.L.M. Cheng. Temporal resolution and snr requirements for accurate dce-mri data analysis using the aath model. *Magnetic Resonance in Medicine*, 64(6):1772–1780, 2010.

[54] S.J. Kim, K. Koh, M. Lustig, S. Boyd, and D. Gorinevsky. An interior-point method for large-scale l_1-regularized least squares. *Selected Topics in Signal Processing, IEEE Journal of*, 1(4):606–617, 2007.

[55] M Koenig, E Klotz, B Luka, D J Venderink, J F Spittler, and L Heuser. Perfusion CT of the brain: diagnostic approach for early detection of ischemic stroke. *Radiology*, 209(1):85–93, 1998.

[56] M. König. Brain perfusion CT in acute stroke: current status. *European journal of radiology*, 45:S11–S22, 2003.

[57] K. Kudo, S. Terae, C. Katoh, M. Oka, T. Shiga, N. Tamaki, and K. Miyasaka. Quantitative cerebral blood flow measurement with dy-

namic perfusion CT using the vascular-pixel elimination method: comparison with h215o positron emission tomography. *American journal of neuroradiology*, 24(3):419–426, 2003.

[58] Kohsuke Kudo, Makoto Sasaki, Kei Yamada, Suketaka Momoshima, Hidetsuna Utsunomiya, Hiroki Shirato, and Kuniaki Ogasawara. Differences in CT perfusion maps generated by different commercial software: Quantitative analysis by using identical source data of acute stroke patients1. *Radiology*, 254(1):200–209, 2010.

[59] I Lawrence and Kuei Lin. A concordance correlation coefficient to evaluate reproducibility. *Biometrics*, pages 255–268, 1989.

[60] K.S.S. Lawrence and T.Y. Lee. An adiabatic approximation to the tissue homogeneity model for water exchange in the brain: I. theoretical derivation. *Journal of Cerebral Blood Flow & Metabolism*, 18(12):1365–1377, 1998.

[61] Jou-Wei Lin, Robert R Sciacca, Ru-Ling Chou, Andrew F Laine, and Steven R Bergmann. Quantification of myocardial perfusion in human subjects using 82Rb and wavelet-based noise reduction. *Journal of Nuclear Medicine*, 42(2):201–208, 2001.

[62] K Lin, KS Kazmi, M Law, J Babb, N Peccerelli, and BK Pramanik. Measuring elevated microvascular permeability and predicting hemorrhagic transformation in acute ischemic stroke using first-pass dynamic perfusion CT imaging. *American Journal of Neuroradiology*, 28(7):1292–1298, 2007.

[63] Donald Lloyd-Jones, Robert Adams, Mercedes Carnethon, Giovanni De Simone, T. Bruce Ferguson, Katherine Flegal, et al. Heart disease and stroke statistics—2009 update: A report from the american heart association statistics committee and stroke statistics subcommittee. *Circulation*, 119(3):480–486, 2009.

[64] Alfredo M Lopez-Yunez, Askiel Bruno, Linda S Williams, Engin Yilmaz, Cristina Zurrú, and José Biller. Protocol violations in community-based rtPA stroke treatment are associated with symptomatic intracerebral hemorrhage. *Stroke*, 32(1):12–16, 2001.

[65] M. Lustig, D. Donoho, and J.M. Pauly. Sparse MRI: The application of compressed sensing for rapid MR imaging. *Magnetic Resonance in Medicine*, 58(6):1182–1195, 2007.

[66] Jianhua Ma, Jing Huang, Qianjin Feng, Hua Zhang, Hongbing Lu, Zhengrong Liang, and Wufan Chen. Low-dose computed tomography image restoration using previous normal-dose scan. *Medical physics*, 38:5713, 2011.

[67] Jianhua Ma, Hua Zhang, Yang Gao, Jing Huang, Zhengrong Liang, Qianjing Feng, and Wufan Chen. Iterative image reconstruction for cerebral perfusion CT using a pre-contrast scan induced edge-preserving prior. *Physics in medicine and biology*, 57(22):7519, 2012.

[68] J. Mairal, F. Bach, J. Ponce, and G. Sapiro. Online dictionary learning for sparse coding. In *Proceedings of the 26th Annual International Conference on Machine Learning*, pages 689–696. ACM, 2009.

[69] J. Mairal, F. Bach, J. Ponce, G. Sapiro, and A. Zisserman. Non-local sparse models for image restoration. In *Computer Vision, 2009 IEEE 12th International Conference on*, pages 2272–2279. IEEE, 2009.

[70] J. Mairal, M. Elad, and G. Sapiro. Sparse representation for color image restoration. *Image Processing, IEEE Transactions on*, 17(1):53–69, 2008.

[71] S.G. Mallat and Z. Zhang. Matching pursuits with time-frequency dictionaries. *Signal Processing, IEEE Transactions on*, 41(12):3397–3415, 1993.

[72] Parinaz Massoumzadeh, Steven Don, Charles F Hildebolt, Kyongtae T Bae, and Bruce R Whiting. Validation of CT dose-reduction simulation. *Medical physics*, 36:174, 2009.

[73] B. Matalon, M. Elad, and M. Zibulevsky. Improved denoising of images using modelling of a redundant contourlet transform. In *Optics & Photonics 2005*, pages 59141Y–59141Y. International Society for Optics and Photonics, 2005.

[74] P. Meier and K.L. Zierler. On the theory of the indicator-dilution method for measurement of blood flow and volume. *Journal of applied physiology*, 6(12):731–744, 1954.

[75] A.M. Mendrik, E. Vonken, B. van Ginneken, H.W. de Jong, A. Riordan, T. van Seeters, E.J. Smit, M.A. Viergever, and M. Prokop. TIPS bilateral noise reduction in 4D CT perfusion scans produces high-quality cerebral blood flow maps. *Physics in Medicine and Biology*, 56(13):3857, 2011.

[76] K A Miles and M R Griffiths. Perfusion CT: A worthwhile enhancement? *British Journal of Radiology*, 76(904):220–231, 2003.

[77] K. Mouridsen, K. Friston, N. Hjort, L. Gyldensted, L. Østergaard, and S. Kiebel. Bayesian estimation of cerebral perfusion using a physiological model of microvasculature. *NeuroImage*, 33(2):570–579, 2006.

[78] Darius G Nabavi, Aleksa Cenic, Rosemary A Craen, Adrian W Gelb, John D Bennett, Roman Kozak, and Ting-Yim Lee. CT assessment of cerebral perfusion: Experimental validation and initial clinical experience. *Radiology*, 213(1):141–149, 1999.

[79] P. Nathan, D.B. Edward, R. Thomas, K. Dan, M.G. Christopher, B. Regan, C. Paul, and H. John. Estimating myocardial perfusion from dynamic contrast-enhanced CMR with a model-independent deconvolution method. *Journal of Cardiovascular Magnetic Resonance*, 10, 2008.

[80] Leif Østergaard, Alma Gregory Sorensen, Kenneth K. Kwong, Robert M. Weisskoff, Carsten Gyldensted, and Bruce R. Rosen. High resolution measurement of cerebral blood flow using intravascular tracer bolus passages. part ii: Experimental comparison and preliminary results. *Magnetic Resonance in Medicine*, 36(5):726–736, 1996.

[81] Leif Østergaard, Robert M. Weisskoff, David A. Chesler, Carsten Gyldensted, and Bruce R. Rosen. High resolution measurement of cerebral blood flow using intravascular tracer bolus passages. part i: Mathematical approach and statistical analysis. *Magnetic Resonance in Medicine*, 36(5):715–725, 1996.

[82] Clifford S Patlak and Ronald G Blasberg. Graphical evaluation of blood-to-brain transfer constants from multiple-time uptake data. Generalizations. *Journal of Cerebral Blood Flow & Metabolism*, 5(4):584–590, 1985.

[83] Clifford S Patlak, Ronald G Blasberg, Joseph D Fenstermacher, et al. Graphical evaluation of blood-to-brain transfer constants from multiple-time uptake data. *J Cereb Blood Flow Metab*, 3(1):1–7, 1983.

[84] J. Portilla, V. Strela, M.J. Wainwright, and E.P. Simoncelli. Image denoising using scale mixtures of gaussians in the wavelet domain. *Image Processing, IEEE Transactions on*, 12(11):1338 – 1351, nov. 2003.

[85] M. Protter and M. Elad. Image sequence denoising via sparse and redun-

dant representations. *Image Processing, IEEE Transactions on*, 18(1):27–35, 2009.

[86] S. Roth and M.J. Black. Fields of experts: A framework for learning image priors. In *Computer Vision and Pattern Recognition, 2005. CVPR 2005. IEEE Computer Society Conference on*, volume 2, pages 860–867. IEEE, 2005.

[87] Noriyuki Saito, Kohsuke Kudo, Tsukasa Sasaki, Masahito Uesugi, Kazuhiro Koshino, Michiko Miyamoto, and Shigehito Suzuki. Realization of reliable cerebral-blood-flow maps from low-dose CT perfusion images by statistical noise reduction using nonlinear diffusion filtering. *Radiological physics and technology*, 1(1):62–74, 2008.

[88] T Schneider, J Hom, J Bredno, JW Dankbaar, S-C Cheng, and M Wintermark. Delay correction for the assessment of blood-brain barrier permeability using first-pass dynamic perfusion CT. *American Journal of Neuroradiology*, 32(7):E134–E138, 2011.

[89] J Shtok, Michael Elad, and Michael Zibulevsky. Sparsity-based sinogram denoising for low-dose computed tomography. In *Acoustics, Speech and Signal Processing (ICASSP), 2011 IEEE International Conference on*, pages 569–572. IEEE, 2011.

[90] J.L. Starck, E.J. Candès, and D.L. Donoho. The curvelet transform for image denoising. *Image Processing, IEEE Transactions on*, 11(6):670–684, 2002.

[91] Enming J Su, Linda Fredriksson, Melissa Geyer, Erika Folestad, Jacqueline Cale, Johanna Andrae, Yamei Gao, Kristian Pietras, Kris Mann, Manuel Yepes, et al. Activation of PDGF-CC by tissue plasminogen activator impairs blood-brain barrier integrity during ischemic stroke. *Nature medicine*, 14(7):731–737, 2008.

[92] Barry J Sullivan and H-C Chang. A generalized landweber iteration for ill-conditioned signal restoration. In *Acoustics, Speech, and Signal Processing, 1991. ICASSP-91., 1991 International Conference on*, pages 1729–1732. IEEE, 1991.

[93] Mark Supanich, Yinghua Tao, Brian Nett, Kari Pulfer, Jiang Hsieh, Patrick Turski, Charles Mistretta, Howard Rowley, and Guang-Hong Chen. Radiation dose reduction in time-resolved CT angiography using highly constrained back projection reconstruction. *Physics in medicine and biology*, 54(14):4575, 2009.

[94] Denis Tack, Viviane De Maertelaer, Wendy Petit, Pierre Scillia, Patrick Muller, Christoph Suess, and Pierre Alain Gevenois. Multi-detector row CT pulmonary angiography: Comparison of standard-dose and simulated low-dose techniques. *Radiology*, 236(1):318–325, 2005.

[95] Zhen Tian, Xun Jia, Kehong Yuan, Tinsu Pan, and Steve B Jiang. Low-dose CT reconstruction via edge-preserving total variation regularization. *Physics in medicine and biology*, 56(18):5949, 2011.

[96] R. Tibshirani. Regression shrinkage and selection via the lasso. *Journal of the Royal Statistical Society. Series B (Methodological)*, pages 267–288, 1996.

[97] Koen Van Leemput, Frederik Maes, Dirk Vandermeulen, and Paul Suetens. Automated model-based bias field correction of MR images of the brain. *Medical Imaging, IEEE Transactions on*, 18(10):885–896, 1999.

[98] Koen Van Leemput, Frederik Maes, Dirk Vandermeulen, and Paul Suetens. Automated model-based tissue classification of MR images of the brain. *Medical Imaging, IEEE Transactions on*, 18(10):897–908, 1999.

[99] Wouter JH Veldkamp, Lucia JM Kroft, Jan Pieter A van Delft, and Jacob Geleijns. A technique for simulating the effect of dose reduction on image quality in digital chest radiography. *Journal of Digital Imaging*, 22(2):114–125, 2009.

[100] Zhou Wang, Alan C Bovik, Hamid Rahim Sheikh, and Eero P Simoncelli. Image quality assessment: From error visibility to structural similarity. *Image Processing, IEEE Transactions on*, 13(4):600–612, 2004.

[101] Martin Wiesmann, Scott Berg, G Bohner, R Klingebiel, V Schöpf, BM Stoeckelhuber, I Yousry, J Linn, and U Missler. Dose reduction in dynamic perfusion CT of the brain: effects of the scan frequency on measurements of cerebral blood flow, cerebral blood volume, and mean transit time. *European radiology*, 18(12):2967–2974, 2008.

[102] M Wintermark and MH Lev. FDA investigates the safety of brain perfusion ct. *American Journal of Neuroradiology*, 31(1):2–3, 2010.

[103] Maeder Wintermark, P Maeder, J-P Thiran, P Schnyder, and R Meuli. Quantitative assessment of regional cerebral blood flows by perfusion CT studies at low injection rates: a critical review of the underlying theoretical models. *European Radiology*, 11(7):1220–1230, 2001.

[104] Max Wintermark, Philippe Maeder, Francis R Verdun, Jean-Philippe Thiran, Jean-François Valley, Pierre Schnyder, and Reto Meuli. Using 80 kVp versus 120 kVp in perfusion CT measurement of regional cerebral blood flow. *American journal of neuroradiology*, 21(10):1881–1884, 2000.

[105] H.J. Wittsack, AM Wohlschläger, EK Ritzl, R. Kleiser, M. Cohnen, RJ Seitz, and U. Mödder. CT-perfusion imaging of the human brain: advanced deconvolution analysis using circulant singular value decomposition. *Computerized Medical Imaging and Graphics*, 32(1):67–77, 2008.

[106] K.K. Wong, C.P. Tam, M. Ng, S.T.C. Wong, and G.S. Young. Improved residue function and reduced flow dependence in MR perfusion using least-absolute-deviation regularization. *Magnetic Resonance in Medicine*, 61(2):418–428, 2009.

[107] J. Wright, A.Y. Yang, A. Ganesh, S.S. Sastry, and Y. Ma. Robust face recognition via sparse representation. *Pattern Analysis and Machine Intelligence, IEEE Transactions on*, 31(2):210–227, 2009.

[108] Ona Wu, Leif Østergaard, Robert M Weisskoff, Thomas Benner, Bruce R Rosen, and A Gregory Sorensen. Tracer arrival timing-insensitive technique for estimating flow in MR perfusion-weighted imaging using singular value decomposition with a block-circulant deconvolution matrix. *Magnetic Resonance in Medicine*, 50(1):164–174, 2003.

[109] J. Yang, J. Wright, T. Huang, and Y. Ma. Image super-resolution as sparse representation of raw image patches. In *Computer Vision and Pattern Recognition, 2008. CVPR 2008. IEEE Conference on*, pages 1–8. IEEE, 2008.

[110] Jianchao Yang, John Wright, Thomas S Huang, and Yi Ma. Image super-resolution via sparse representation. *Image Processing, IEEE Transactions on*, 19(11):2861–2873, 2010.

[111] Lifeng Yu, Xin Liu, Shuai Leng, James M Kofler, Juan C Ramirez-Giraldo, Mingliang Qu, Jodie Christner, Joel G Fletcher, and Cynthia H McCollough. Radiation dose reduction in computed tomography: techniques and future perspective. *Imaging*, 1(1):65–84, 2009.

[112] Gerald Zauner, Michael Reiter, D Salaberger, and J Kastner. Denoising of computed tomography images using multiresolution based methods. *Proceedings of ECNDT, Berlin Sept*, 2006.

[113] Qiang Zhang and Baoxin Li. Discriminative K-SVD for dictionary learning in face recognition. In *Computer Vision and Pattern Recognition (CVPR), 2010 IEEE Conference on*, pages 2691–2698. IEEE, 2010.

[114] S. Zhang, Y. Zhan, M. Dewan, J. Huang, Dimitris N. Metaxas, and X.S. Zhou. Towards robust and effective shape modeling: Sparse shape composition. *Medical image analysis*, 16(1):265–277, 2012.

[115] Shaoting Zhang, Junzhou Huang, Hongsheng Li, and Dimitris N Metaxas. Automatic image annotation and retrieval using group sparsity. *IEEE Transactions on Systems, Man, and Cybernetics, Part B: Cybernetics*, 42(3):838–849, 2012.

[116] Shaoting Zhang, Junzhou Huang, Dimitris Metaxas, Wei Wang, and Xiaolei Huang. Discriminative sparse representations for cervigram image segmentation. In *Biomedical Imaging: From Nano to Macro, 2010 IEEE International Symposium on*, pages 133–136. IEEE, 2010.

[117] Shaoting Zhang, Yiqiang Zhan, and Dimitris N. Metaxas. Deformable segmentation via sparse representation and dictionary learning. *Medical Image Analysis*, 16(7):1385 – 1396, 2012.

[118] S.C. Zhu and D. Mumford. Prior learning and gibbs reaction-diffusion. *Pattern Analysis and Machine Intelligence, IEEE Transactions on*, 19(11):1236–1250, 1997.